

Warin Ratchananusorn

## **DEVELOPMENT OF A PROCESS FOR THE DIRECT SYNTHESIS OF HYDROGEN PEROXIDE IN A NOVEL MICROSTRUCTURED REACTOR**

Thesis for the degree of Doctor of Science (Technology) to be presented with due permission for public examination and criticism in the Auditorium 1383 at Lappeenranta University of Technology, Lappeenranta, Finland on the 29<sup>th</sup> of November, 2013, at noon.

Acta Universitatis  
Lappeenrantaensis 541

Supervisor	Professor Ilkka Turunen Department of Chemical Technology Lappeenranta University of Technology Finland
Reviewers	Professor Juha Lehtonen Department of Biotechnology and Chemical Technology Aalto University Finland
	Professor Gabriel Wild Laboratoire Réactions et Génie des Procédés Université de Lorraine France
Opponent	Professor Gabriel Wild Laboratoire Réactions et Génie des Procédés Université de Lorraine France
Custos	Professor Ilkka Turunen Department of Chemical Technology Lappeenranta University of Technology Finland

ISBN 978-952-265-491-5

ISBN 978-952-265-492-2 (PDF)

ISSN-L 1456-4491

ISSN 1456-4491

Lappeenrannan Teknillinen Yliopisto  
Yliopistopaino 2013

## **Abstract**

Warin Ratchananusorn

### **Development of a process for the direct synthesis of hydrogen peroxide in a novel micro-structured reactor**

Lappeenranta 2013

53 p.

Acta Universitatis Lappeenrantaensis 541

Diss. Lappeenranta University of Technology

ISBN 978-952-265-491-5, ISBN 978-952-265-492-2 (PDF),

ISSN-L 1456-4491, ISSN 1456-4491

Microreactors have proven to be versatile tools for process intensification. Over recent decades, they have increasingly been used for product and process development in chemical industries. Enhanced heat and mass transfer in the reactors due to the extremely high surface-area-to-volume ratio and interfacial area allow chemical processes to be operated at extreme conditions. Safety is improved by the small holdup volume of the reactors and effective control of pressure and temperature.

Hydrogen peroxide is a powerful green oxidant that is used in a wide range of industries. Reduction and auto-oxidation of anthraquinones is currently the main process for hydrogen peroxide production. Direct synthesis is a green alternative and has potential for on-site production. However, there are two limitations: safety concerns because of the explosive gas mixture produced and low selectivity of the process.

The aim of this thesis was to develop a process for direct synthesis of hydrogen peroxide utilizing microreactor technology. Experimental and numerical approaches were applied for development of the microreactor.

Development of a novel microreactor was commenced by studying the hydrodynamics and mass transfer in prototype microreactor plates. The prototypes were designed and fabricated with the assistance of CFD modeling to optimize the shape and size of the microstructure. Empirical correlations for the mass transfer coefficient were derived.

The pressure drop in micro T-mixers was investigated experimentally and numerically. Correlations describing the friction factor for different flow regimes were developed and predicted values were in good agreement with experimental results.

Experimental studies were conducted to develop a highly active and selective catalyst with a proper form for the microreactor. Pd catalysts supported on activated carbon cloths were prepared by different treatments during the catalyst preparation. A variety of characterization methods were used for catalyst investigation. The surface chemistry of the support and the oxidation state of the metallic phase in the catalyst play important roles in catalyst activity and selectivity for the direct synthesis.

The direct synthesis of hydrogen peroxide was investigated in a bench-scale continuous process using the novel microreactor developed. The microreactor was fabricated based on the hydrodynamic and mass transfer studies and provided a high interfacial area and high mass transfer coefficient. The catalysts were prepared under optimum treatment conditions. The direct synthesis was conducted at various conditions.

The thesis represents a step towards a commercially viable direct synthesis. The focus is on the two main challenges: mitigating the safety problem by utilization of microprocess technology and improving the selectivity by catalyst development.

**Keywords:** microreactors; pressure drop; computational fluid dynamics; hydrodynamics; mass transfer; hydrogen peroxide; direct synthesis.

UDC 66.023:555.511.32:66.021.3:542.05:66

## **Acknowledgements**

The research work was carried out in the Laboratory of Process and Product development at Lappeeranta University of Technology.

I express my deepest gratitude to my supervisor, Professor Ilkka Turunen, for giving me the opportunity to study and the freedom to conduct the research. I also thank for his invaluable advices and supervisions throughout the whole research.

I gratefully thank for the valuable comments on my thesis by Professor Gabriel Wild and Professor Juha Lehtonen. I acknowledge Peter Jones for his hard work in language revision of my manuscripts.

The Graduate School of Chemical Engineering (GSCE), The Finnish Funding Agency for Technology and Innovation (TEKES), Neste Oil Oyj and The Center of Separation Technology (CST) are gratefully acknowledged for funding this research.

I would like to thank Davood Gudarzi M.Sc. for his enthusiastic co-operation, friendship and creating relaxing environment in the laboratory. I acknowledge to Denis Semyonov M.Sc. and Azita Soleymani D.Sc. for efficient works and collaborations. I express my appreciation to Arto Laari D.Sc. and a former colleague, Eero Kolehmainen D.Sc., for helpful discussion and support.

I particularly grateful to many friends and colleagues, especially Abay, Alex, Iris, Marcelo, Marju, Matti, Piia, Sai, Teemu, Tomomi, and Verr. I was able to complete my journey through all the dark autumns and mighty cold winters in Finland by the support and friendship from all of these very special people.

I also would like to thank many friends overseas for their friendship, encouragement and keeping on pushing me on the track.

Finally, I express my wholehearted thanks to my supportive family. This thesis is dedicated to them.

Warin Ratchananusorn

Lappeenranta



## Table of contents

<b>List of Publications</b> .....	<b>9</b>
<b>List of Symbols</b> .....	<b>11</b>
<b>1. Introduction</b> .....	<b>13</b>
1.1 Background.....	13
1.2 Microreactor technology.....	13
1.3 Hydrogen peroxide.....	14
1.4 Objectives of the work.....	16
1.5 Outline.....	17
<b>2. Development of the microreactor</b> .....	<b>18</b>
2.1 Prototype microreactor.....	18
2.2 Hydrodynamic study.....	20
2.2.1 Flow patterns.....	20
2.2.2 Hydrodynamic parameters.....	21
2.3 Mass transfer.....	24
2.4 Roles of CFD in prototype microreactor plate development.....	27
2.5 Pressure drop in micro T-mixers.....	29
<b>3. Development of the catalyst</b> .....	<b>33</b>
3.1 Catalyst support.....	33
3.2 Catalyst preparation.....	34
3.3 Catalyst tests.....	34
3.3.1 Catalyst characterization.....	34
3.3.2 Catalyst activity.....	34
<b>4. Development of a process for the direct synthesis of hydrogen peroxide</b> .....	<b>38</b>
4.1 Microreactor.....	38
4.2 Experimental setup.....	39
4.3 Experimental procedure.....	40
4.4 Catalyst.....	41
4.5 Results.....	42
4.5.1 Long-term experiments.....	42
4.5.2 Effect of the process conditions.....	44
4.6 Possible directions for further development of the process.....	47
<b>5. Conclusions</b> .....	<b>48</b>
<b>References</b> .....	<b>50</b>



## List of Publications

This thesis is based on the following publications, which are referred to in the text by Roman numbers I-V.

- I. Soleymani, A., Yousefi, H., Ratchananusorn, W., Turunen, I. (2010). Pressure drop in micro T-mixers, *Journal of Micromechanics and Microengineering*, 20, 15029-15035.
- II. Ratchananusorn, W., Semyonov, D., Gudarzi, D., Kolehmainen, E., Turunen, I. (2011). Hydrodynamics and mass transfer studies on a plate microreactor, *Chemical Engineering and Processing: Process Intensification*, 50, 1186-1192.
- III. Semyonov, D., Ratchananusorn, W., Turunen, I. (2013). Hydrodynamic model of a microstructured plate reactor, *Computers and Chemical Engineering*, 52, 145-154.
- IV. Gudarzi, D., Ratchananusorn, W., Turunen, I., Salmi, T., Heinonen, M. (2013). Preparation of Pd catalysts supported on activated carbon cloth (ACC) for direct synthesis of H<sub>2</sub>O<sub>2</sub> from H<sub>2</sub> and O<sub>2</sub>, *Topics in Catalysis*, 56, 527-539.
- V. Ratchananusorn, W., Gudarzi, D., Turunen, I., Catalytic direct synthesis of hydrogen peroxide in a novel microstructured reactor, *Submitted to Chemical Engineering and Processing: Process Intensification*.

## Author's contribution in the publications

For I, the author carried out the experiments and participated in writing the paper. For II, the author was the prime contributor and had a major role in conducting the experiments, analyzing the data, drawing the conclusions and writing the paper. For III, the author was responsible for the experimental part and participated in writing the paper. For IV, the author carried out the experiments with co-authors and participated in writing the paper. For V, the author was the prime contributor and had a major role in conducting the experiments, analyzing the data, drawing the conclusions and writing the paper.

In addition to the publications mentioned above, the author has presented related work at two international scientific conferences during the period 2009-2013.

## **Related publications**

- I. Ratchanusorn, W., Semyonov, D., Gudarzi, D., Kolehmainen, E., Turunen, I. (2009). Hydrodynamics and mass transfer studies in a microreactor plate, *2<sup>nd</sup> European Process Intensification Conference*, Venice, Italy, 14-17 June. *Oral presentation.*
- II. Ratchanusorn, W., Gudarzi, D., Turunen, I. (2013) Hydrogen peroxide direct synthesis on Pd catalysts in a microreactor, *9<sup>th</sup> European Congress of Chemical Engineering*, The Hague, The Netherlands, 21-25 April. *Oral presentation.*

## List of Symbols

$a$	specific surface area	$\text{m}^2 \text{m}^{-3}$
$A$	area	$\text{m}^2$
$C$	concentration	$\text{mol m}^{-3}$
$C^*$	saturation concentration	$\text{mol m}^{-3}$
$D$	diffusivity	$\text{m}^2 \text{s}^{-1}$
$Dh$	hydraulic diameter	$\text{m}$
$Dr$	ratio of the hydraulic diameter of mixing and inlet channel	-
$f$	friction factor	-
$h$	holdup	-
$k$	volumetric mass transfer coefficient	$\text{m s}^{-1}$
$K$	flow regime identification number	-
$L$	length	$\text{m}$
$Lx$	length of the control volume located in the mixing channel	$\text{m}$
$Ly$	length of the control volume located in the inlet channel	$\text{m}$
$P$	pressure	bar
$Re$	Reynolds number	-
$U$	local flow velocity	$\text{m s}^{-1}$
$\dot{V}$	volumetric flow rate	$\text{m}^3 \text{s}^{-1}$

## Greek symbols

$\varepsilon$	volume fraction	-
$\rho$	density	$\text{kg m}^{-3}$
$v$	superficial velocity	$\text{mm s}^{-1}$

## Subscripts

$cr$	cross sectional
$f$	fluid
$g$	gas
$in,1$	inlet channel 1
$in,2$	inlet channel 2
$s$	mixing channel of the control volume
$s,1$	inlet channel 1 of the control volume

<i>s,2</i>	inlet channel 2 of the control volume
<i>l</i>	liquid
<i>norm</i>	normalized
<i>out</i>	outlet
<i>per</i>	perimeter
<i>r</i>	reactor
<i>s</i>	structured plate reactor
<i>sq</i>	square structure plate
<i>tot</i>	total
<i>tri</i>	triangular structure plate

### **Abbreviations**

ACC	activated carbon cloth
CFD	computational fluid dynamics
DTA	differential thermal analysis
ODE	ordinary differential equations
SEM	scanning electron microscope
TGA	thermal gravimetric analysis
TPD	temperature programmed desorption
XPS	X-ray photoelectron spectroscopy

## **1. Introduction**

### **1.1 Background**

Development of chemical processes aims to improve yields and to make processes more profitable with minimized resources. With increasing environmental awareness, the development of sustainable technology that minimizes the impact on nature has become an area of considerable research interest. Recent innovations in the design and fabrication of microreactors bring promising prospects for sustainable process development. This technology provides substantial improvement on previous approaches, allowing safer processes, simpler process optimization and rapid scale-up and implementation.

### **1.2 Microreactor technology**

The emerging field of process intensification has delivered technological advances, operational efficiency, and sustainable improvements to chemical processes. Stankiewicz and Moulijn (2000) proposed a definition of process intensification as: “Any chemical engineering development that leads to a substantially smaller, cleaner, and more energy-efficient technology is process intensification”. The technology aims to decrease dramatically the plant size/capacity ratio by several orders of magnitude, as well as mitigating environmental and safety impacts of chemical processes.

Microreactors represent process intensification at its extreme and provide substantial benefits over conventional technology: The surface-area-to-volume ratio in microreactors is high. High heat transfer rates can be achieved, allowing highly exothermic reactions. Improved cooling capacity enables safe application of higher operation temperatures and therefore higher reaction rates. Hundred-fold enhancement in mass transfer is possible because of increased interfacial areas between phases (Losey *et al.*, 2001, 2002) and typical limitations of gas transport into the liquid phase found in macroscale reactors are avoided. Process safety is improved by the minimized dimensions of the equipment, resulting in suppressed radical chains of the explosion mechanism. And, finally, small hold-up in the reactors limits potential hazards from explosions (Ehrfeld *et al.*, 2002; Hessel *et al.*, 2004).

Even though microreactor technology has clearly shown its potential in a wide range of research areas and industrial applications, implementations for existing processes face practical challenges. For example, the small capacity inevitably limits application possibilities. Another challenge is the need to distribute fluids uniformly into several hundred

or thousand microchannels. Moreover, possible blockage and fouling of the channels can cause serious operational difficulties.

### 1.3 Hydrogen peroxide

Hydrogen peroxide is one of the most powerful and commonly used oxidizing agents. It is an inherently green oxidant because the only byproduct from oxidation is water. The consumption of hydrogen peroxide has increased during past decades because of its applicability to a wide range of industries (see Figure 1). Centi *et al.* (2009) reported that global consumption of hydrogen peroxide was 2.2 million tons in 2009 and expected to be over 4 million tons by the end of 2012. The demand for hydrogen peroxide is dominated by pulp bleaching and chemicals production.

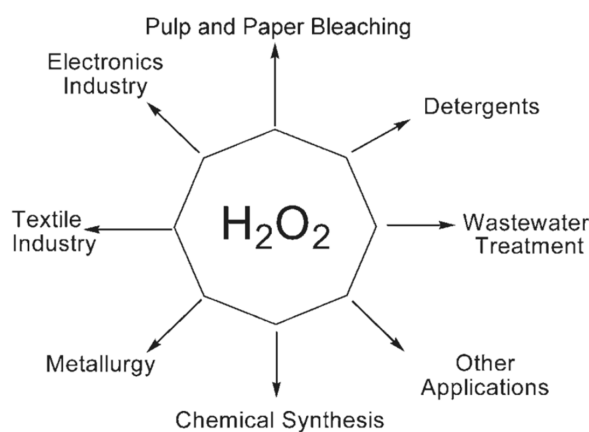


**Figure 1.** Global consumption of hydrogen peroxide (Campos-Martin *et al.* 2006).

Hydrogen peroxide is mainly produced by anthraquinone process. The process involves a cyclic operation where alkyl-anthraquinone is hydrogenated by  $H_2$  over a Pd catalyst to alkyl-anthrahydroquinone followed by auto-oxidation by  $O_2$  back to alkyl-anthraquinone. Hydrogen peroxide is generated during the oxidation step. The reaction scheme is presented in Figure 2.

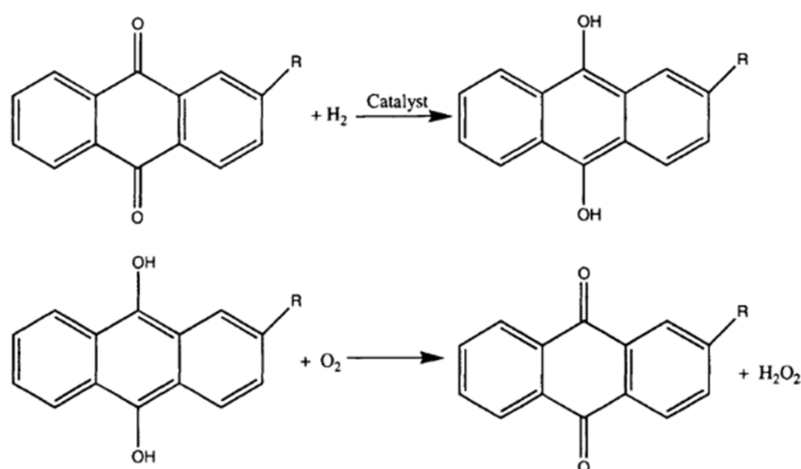


**Figure 2.** Hydrogen peroxide production by anthraquinone process (Jones and Clark, 1999).

There are several drawbacks to the anthraquinone process. The process consists of several steps and involves organic solvents. Extraction is needed to transfer hydrogen peroxide from the solvent to the aqueous phase. Distillation of the product to higher concentration (up to 50-70 wt.%) is required before transportation to end users. In view of its complexity, the process is suitable mainly for large-scale production. (Elvers *et al.*, 1989; Centi *et al.* 2009)

Chemical and environmental applications usually require H<sub>2</sub>O<sub>2</sub> in low concentrations and commercially available hydrogen peroxide is often diluted to lower concentration on-site before use. Small scale on-site processes where hydrogen peroxide can be produced at low concentration are consequently desirable. Furthermore, hydrogen peroxide can cause explosions; therefore, utilizing on-site technology avoids risks from transportation of hydrogen peroxide at high concentration.

Direct synthesis of hydrogen peroxide by direct combination of H<sub>2</sub> and O<sub>2</sub> was invented in the early 20<sup>th</sup> century (Samanta, 2008). The process is considered a green alternative to the current anthraquinone process and provides several benefits:

- The chemistry is more straightforward than in the anthraquinone process.
- The process has lower investment and operating costs due to the substantially smaller amount of equipment required.
- The process is green when compared to the anthraquinone process. This is clear if water is used as a solvent. The direct synthesis is greener even with methanol as a solvent because the total volume of organic liquid in the process would be substantially less.
- The process is favorable for on-site production.

However, technical challenges mean that the process has not yet been applicable for the industrial scale. Firstly, the mixture of  $H_2$  and  $O_2$  is explosive at a wide range of concentrations (5-96 vol%  $H_2$  at atmospheric pressure) (Baukal, 1998) and the explosive range widens further with increasing pressure. Additionally, direct synthesis involves several side reactions, as shown in Figure 3, leading to low selectivity.

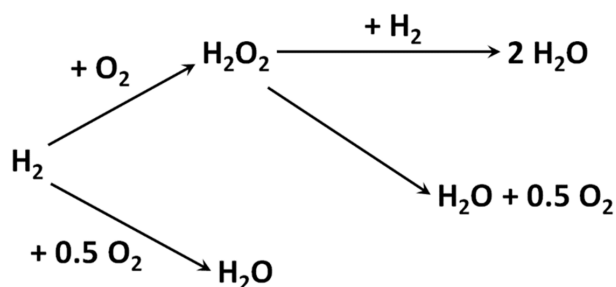


**Figure 3.** Reactions in the direct synthesis of hydrogen peroxide.

#### 1.4 Objectives of the work

The main objective of the thesis study was to develop a process for the direct synthesis of hydrogen peroxide utilizing microreactor technology. The scope of the work, presented in Figure 4, includes development of the process, microreactor and catalyst. Development of the microreactor aims to achieve favorable hydrodynamic and mass transfer behavior. In addition, pressure drop in microchannels was studied to improve understanding of microscale fluid flow phenomena. A further key objective was to develop a catalyst providing high yield and selectivity. Finally, a bench-scale process for the direct synthesis was constructed using the developed microreactor and catalyst.

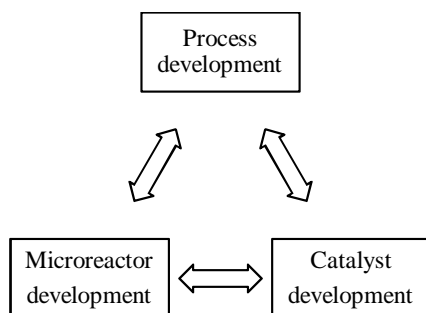


**Figure 4.** Scope of the work.

### 1.5 Outline

This thesis comprises two main parts; a summary part and five publications from international journals. The summary part presents the results from publications I-V. The main results from publication I are presented in chapter 2.5. The results from publication II are presented in chapter 2.1-2.3 and the main results from publication III in chapter 2.4. The results from publication IV are summarized in chapter 3. The results from publication V are presented in chapter 4.

## **2. Development of the microreactor**

Flow in microchannels is usually laminar (Jensen, 2001) and mainly dominated by viscosity, surface tension, and wall friction forces (Waelchli and Rohr, 2006). The hydrodynamics in microchannels are affected by the configuration of the flow channel. The main mixing principle is mainly dominated by molecular diffusion. In multiphase flow, mixing of two phases is problematic because the interfacial force causes the phases to coalesce rapidly. Gas bubbles and liquid droplets tend to merge and form large gas or liquid slugs. Understanding of the unconventional physics involved in the operation is crucial for design, optimization, manufacture, and utilization of microstructure devices.

In this study, a plate-type microreactor was selected for investigation in order to benefit from the advantages such reactors offer over more conventional multichannel structures. Firstly, gas-liquid mass transfer might be faster than in the reactor with parallel microchannels. Moreover, plugging problems were expected to be less severe and more uniform fluid distribution was anticipated. Changing and regeneration of the catalyst are less complex because the plates can be easily separated from each other.

Two prototype microreactor plates were developed for the hydrodynamic and mass transfer studies. The flow at different rates was investigated and hydrodynamic parameters were determined. Mass transfer was studied and mass transfer correlations were developed. The results from both reactor plates were compared.

### **2.1 Prototype microreactor**

Two novel microreactor plates were constructed from parallel plates and the reaction space was located between them. Each reactor plate has a different microstructure comprising a number of microstructural elements in square or triangular shape. The first microreactor plate consists of square structural elements. The microstructure size and shape were optimized simultaneously using a CFD approach and the results are discussed further in chapter 2.4. A triangular structure was selected for the second microreactor plate. An overview of the microreactor plates is shown in Figure 5(a) and their detailed structure in Figure 5(b) and 5(c).

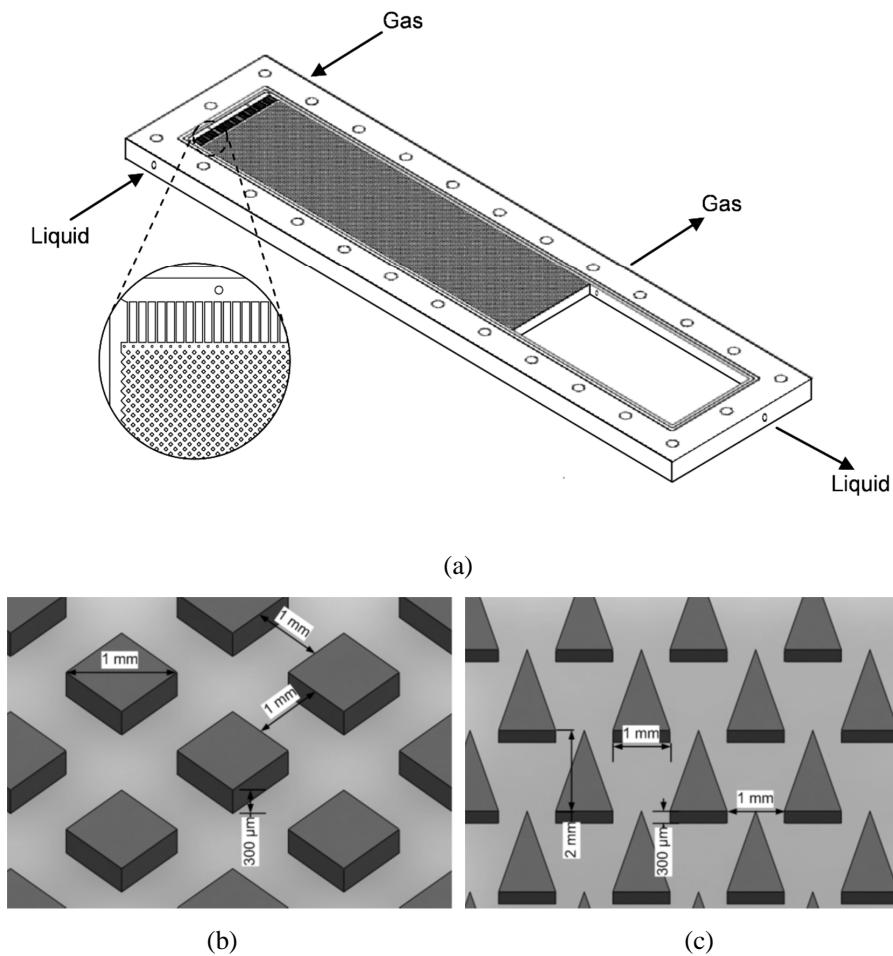


**Figure 5.** Prototype microreactor plates: (a) Microreactor plate showing inlet and outlet of gas and liquid. (b) Square structure layout and dimensions. (c) Triangular structure layout and dimensions.

The microreactor plates are made of stainless steel and consist of three sections: the inlet, reaction, and outlet section. Liquid and gas enter into the reactor at the inlet section from opposite sides and are divided into a number of substreams. The mixing and dispersion occurs in the reaction section, which consists of the structural elements. The size of the reaction section is 10×40 cm. The layout and dimensions of the structural elements are shown in Figure 5(b) and 5(c). The structural elements are arranged in staggered arrays forming a number of parallel microchannels and providing a fraction of free space of 0.83 in the square structure configuration and 0.75 in the triangular structure configuration. The distance between the plates is 300 μm. The reactor is vertically operated, allowing the fluids to flow

downwards through the reaction section to the outlet section, where the gas and liquid are separated by gravity. The liquid is then removed from the bottom and the gas is removed from the top of the outlet section.

## 2.2 Hydrodynamic study

The experimental setup for the hydrodynamics study in the prototype microstructured reactor is presented in Figure 6. The reactor was covered with acrylic plate for visual observation. A high speed camera was used to capture still images at different flow conditions in order to be able to determine hydrodynamic parameters. The liquid was fed to the reactor with a flow rate of 20 to 100 ml/min. After the liquid had filled the whole reactor, the gas was fed with a flow rate of 36 to 180 ml<sub>n</sub>/min. More detailed information about the experiments is given in publication II.

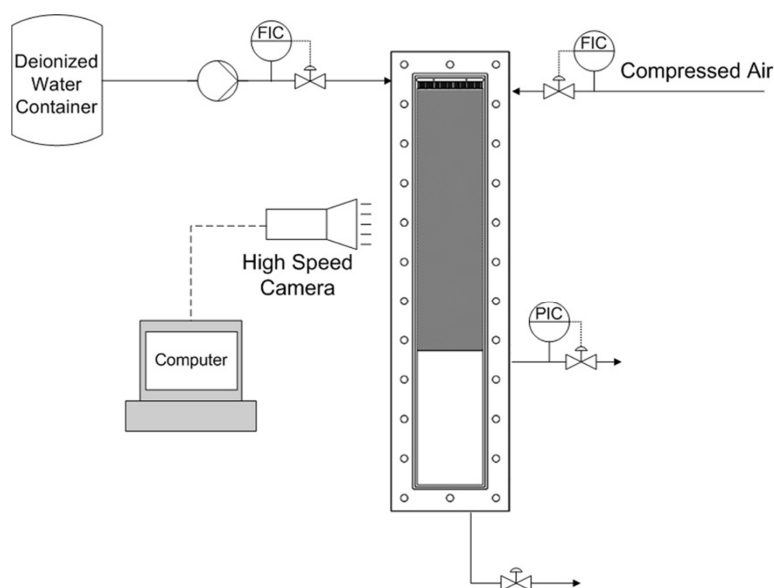


**Figure 6.** Experimental setup for hydrodynamic study.

### 2.2.1 Flow patterns

Hydrodynamics of gas and liquid flow in microchannels has been extensively studied by Coleman and Garimella (1999), Kawahara *et al.* (2002), Waelchli and von Rohr (2006) and Pohorecki *et al.* (2008). The flow often appears as slug (Taylor) flow, where elongated gas bubbles occupy the whole cross section of the channel, alternating with liquid slugs. Only a thin liquid film then separates the gas slugs from the channel wall. As shown by Pohorecki

(2007), this thin liquid film might be saturated by dissolving gas, in which case only the end of the gas slugs provide an active interfacial area for mass transfer, which might decrease the reactor performance remarkably.

The flow in the microreactor in this study differs from typical flow patterns in conventional microchannels. The flow channel in the current reactor is rectangular-shaped with a very high aspect ratio (width-to-height) and, therefore, flow patterns widely used to describe flow in conventional capillary or cylindrical microchannels are not applicable.

Channeling was observed at low flow rates, resulting in the liquid and gas flowing downwards separately and finding their own routes. As the flow rates were increased, instabilities were detected at the gas-liquid interface, leading to discontinuities of liquid or gas streams. When the flow rates were high enough, the streams of gas and liquid were completely broken into small gas bubbles and liquid slugs, respectively. This flow represents favorable hydrodynamical conditions of the reactor.

### **2.2.2 Hydrodynamic parameters**

Investigation of the flow behavior showed that the flow in the microreactor plates was relatively unstable. The flow trajectories changed continuously due to breaking-recombining behavior caused by the structural elements inside the reactors. Sample images for image analysis were captured from the reaction section where the two phase flow was fully developed. The hydrodynamic parameters, gas holdup and gas-liquid interfacial area were determined as average values from several sample images taken at different time spans in order to limit the uncertainty from the unstable flow. The image processing software, ImageJ, was used to determine the hydrodynamic parameters. The steps in image processing are presented in Figure 7. Figure 7(a) presents original images. These images were processed by inverting the colors so that the gas phase has dark color, as in Figure 7(b). The perimeter of the gas phase in Figure 7(b) was generated and is shown in Figure 7(c).

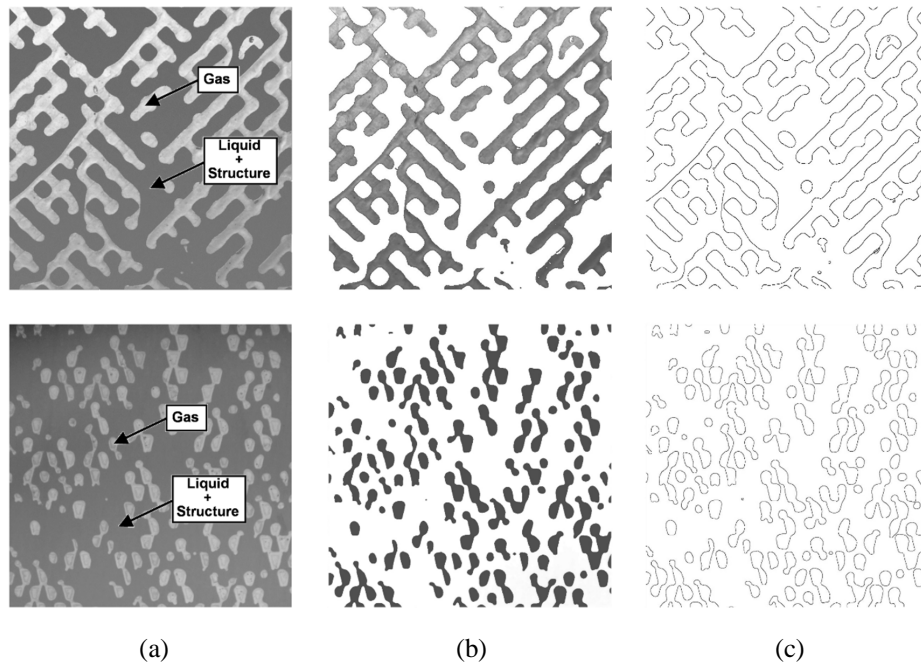


**Figure 7.** Image processing steps for gas holdup and gas-liquid interfacial area measurements; a) original image b) processed image showing the area of the gas slugs c) processed image showing the perimeters of the gas slugs.

The area of the gas slugs (see Figure 7(b)) reveals gas holdup, values of which are presented in Figure 8. Figure 9(a) presents the gas-liquid interfacial area determined from only the perimeter of the gas slugs (see Figure 7(c)), denoted by the subscript *per*. Figure 9(b) presents the interfacial area determined from both the perimeter of the gas slugs and the area against the bottom and cover plate, denoted by the subscript *tot*. The latter represents the total interfacial area. However, in some applications, only the area  $a_{per}$  might be active in mass transfer and the liquid film separating the gas from the flow channel wall might be saturated by dissolving gas (Pohorecki, 2007). The gas-liquid interfacial area was determined both as the area per volume of fluid, denoted by the subscript *f*, and per volume of the reactor, denoted by the subscript *r*.

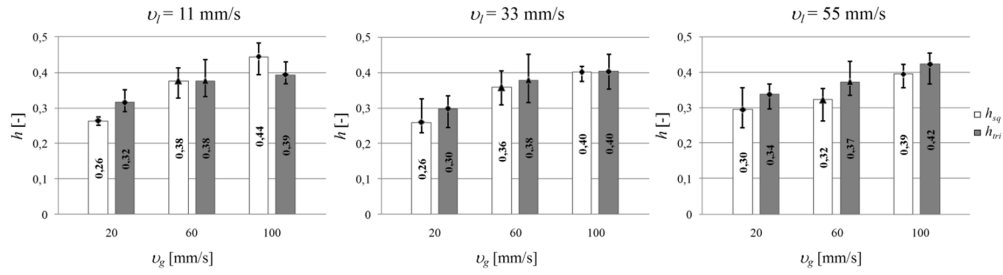


**Figure 8.** Gas holdup at various flow conditions.

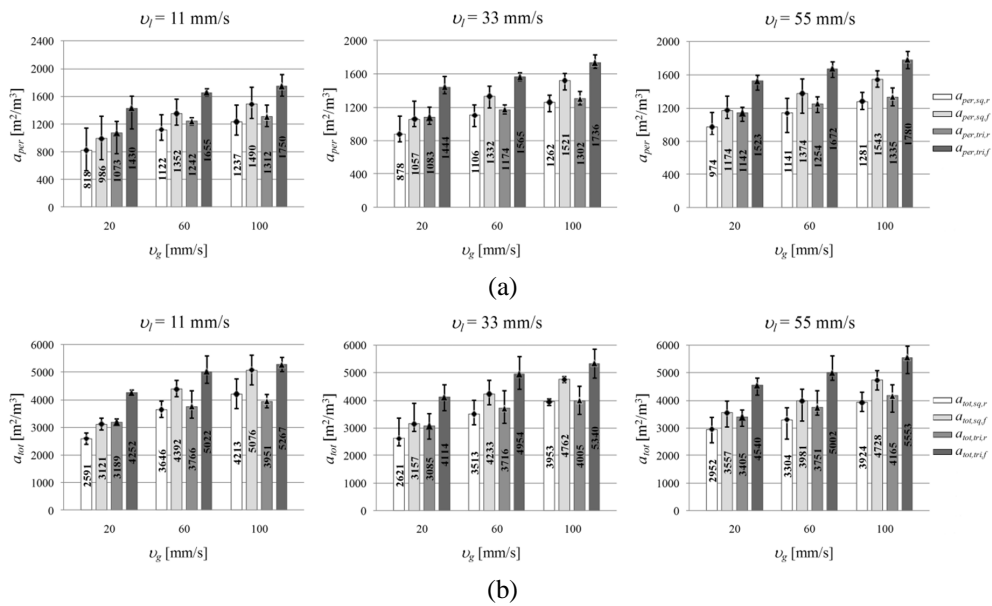


**Figure 9.** Gas-liquid interfacial area at various flow conditions: (a) determined from only the perimeter of the gas slugs, (b) determined from the perimeter of the gas slugs and the area against the bottom and cover plate.

Gas holdup determined from the experiments was in the range of 20-45 %. The values of the total gas-liquid interfacial area were high, up to 4800 and 5600  $\text{m}^2/\text{m}^3$  for the square and triangular structure microreactor, respectively, which is much higher than in typical commercial gas-liquid reactors, where 1000  $\text{m}^2/\text{m}^3$  is seldom exceeded. The interfacial area in the triangular structure reactor was higher because of differences in the void fraction and in the number and shape of the structural elements.

### 2.3 Mass transfer

The experimental setup for mass transfer study in the microreactor is shown in Figure 10. A water–nitrogen–oxygen system was used. Deionized water was saturated with oxygen, and nitrogen was used to strip oxygen out from the liquid phase. An in-line electrochemical dissolved oxygen sensor was employed to measure the concentration of oxygen at the inlet and outlet of the reactor. The ranges of the gas and liquid flow rates were the same as in the hydrodynamic measurements.

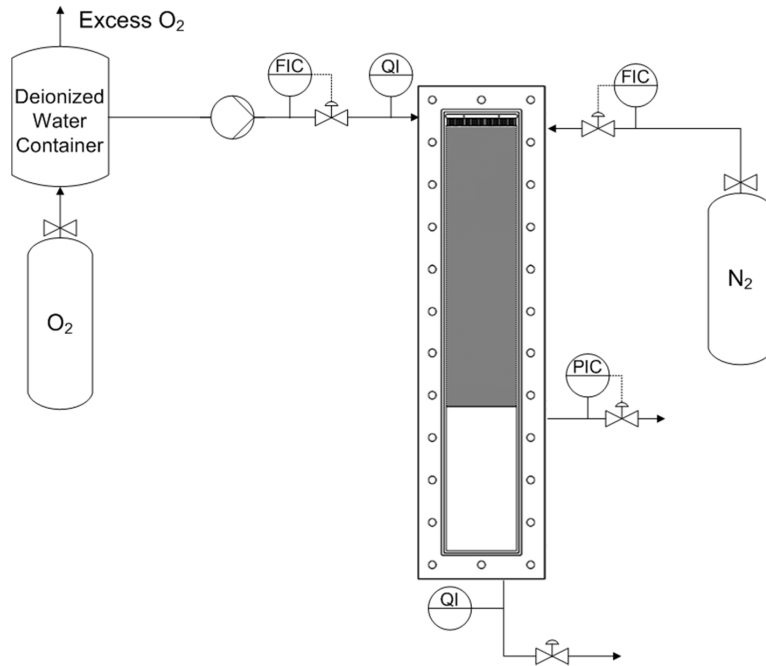


**Figure 10.** Experimental setup for mass transfer study.

In the mass transfer study, oxygen was transferred from liquid phase to gas phase and nitrogen vice versa. Change in molar flow of oxygen and nitrogen in the gas phase can be described by the following equations.

$$\frac{d\dot{n}_{O_2}}{dL} = -k_l a (C_{O_2}^* - C_{O_2}) (1 - \varepsilon_s) A_{cr} \quad (1)$$

$$\frac{d\dot{n}_{N_2}}{dL} = -\frac{D_{N_2}}{D_{O_2}} k_l a (C_{N_2}^* - C_{N_2}) (1 - \varepsilon_s) A_{cr} \quad (2)$$

Concentrations of oxygen and nitrogen in the liquid phase change according to the following equations

$$\frac{dC_{O_2}}{dL} = k_l a (C_{O_2}^* - C_{O_2}) \frac{A_{cr} (1 - \varepsilon_s) (1 - \varepsilon_g)}{\dot{V}_l} \quad (3)$$

$$\frac{dC_{N_2}}{dL} = \frac{D_{N_2}}{D_{O_2}} k_l a (C_{N_2}^* - C_{N_2}) \frac{A_{cr} (1 - \varepsilon_s) (1 - \varepsilon_g)}{\dot{V}_l} \quad (4)$$

A mass transfer model can be presented as an empirical correlation as a function of gas and liquid superficial velocities.

$$k_l a = \alpha_1 \left( \frac{v_g}{v_{g,norm}} \right)^{\alpha_2} \left( \frac{v_l}{v_{l,norm}} \right)^{\alpha_3} \quad (5)$$

where  $v_{g,norm}$  and  $v_{l,norm}$  are equal to 0.02 m/s.

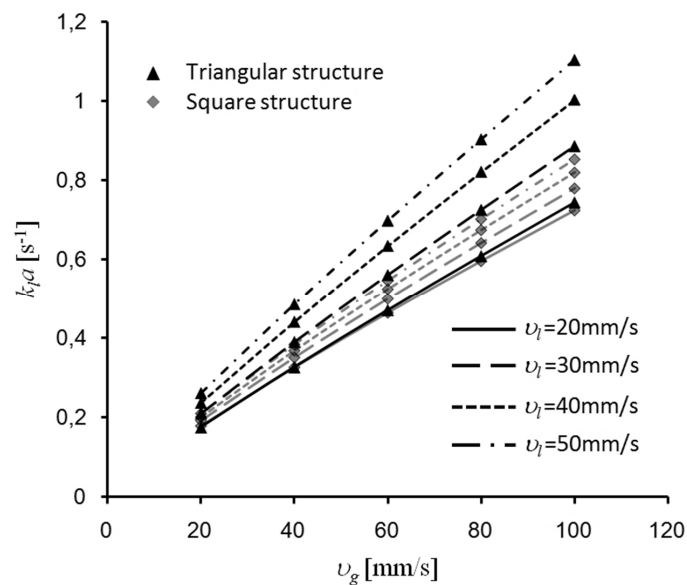
A set of experiments was performed on both the square and triangular structure microreactors. In each experiment  $O_2$  concentration in the liquid was measured at the inlet ( $L = 0$  mm) and outlet of the microreactor ( $L = 400$  mm) for each gas and liquid flow rate. Inlet measurements defined initial conditions for the system of ordinary differential equations (ODE) and outlet measurements were used to fit the model parameters. An Euler method was then used to solve the ODE system.

$k_l a$  values were estimated by minimizing the sum of the squared differences between the estimated and the measured values at the outlet of the reactor. Corresponding estimated optimal parameter values are shown in Table 1.

**Table 1.** Parameter values and correlation for mass transfer coefficient.

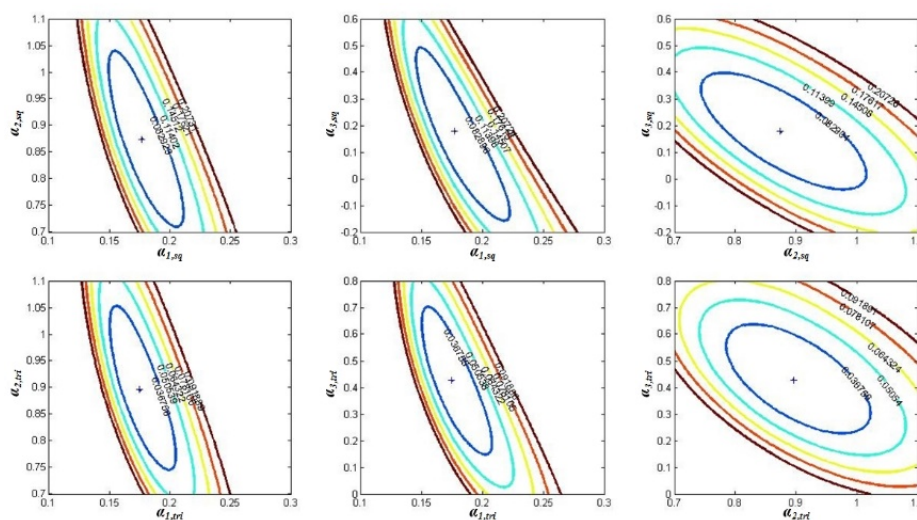
Element type	$\alpha_1$	$\alpha_2$	$\alpha_3$	Correlation
Square (◆)	0.177	0.874	0.179	$k_l a = 0.177 \left( \frac{v_g}{0.02} \right)^{0.874} \left( \frac{v_l}{0.02} \right)^{0.179}$
Triangular (▲)	0.175	0.899	0.432	$k_l a = 0.175 \left( \frac{v_g}{0.02} \right)^{0.899} \left( \frac{v_l}{0.02} \right)^{0.432}$

Figure 11 shows that mass transfer in the triangular structure microreactor was better than in the square structure one. The difference is explained, at least partly, by the difference in the void fraction (0.17 in the square structured plate and 0.25 in the triangular one), number and shape of the structural elements. The maximum  $k_{l}a$  values in the triangular structure microreactor were as high as  $1.10 \text{ s}^{-1}$ , which was approximately 25% higher than in the square structure reactor, where the highest value was  $0.85 \text{ s}^{-1}$ . The mass transfer coefficients from this study are in the range from  $0.17$  to  $1.10 \text{ s}^{-1}$ , which is one or two orders of magnitude higher than conventional scale gas-liquid contactors and in the same range as in other microscale gas-liquid contactors.



**Figure 11.** Estimated  $k_{l}a$  dependency on  $v_g$  and  $v_l$ .

Sensitivity analysis of the estimated parameters ( $\alpha_1$ ,  $\alpha_2$ , and  $\alpha_3$ ) was carried out to determine their identifiability and the goodness of the fit. The aim of the analysis was to determine the shape of the objective function representing the sum of squares  $SS(\alpha_1, \alpha_2, \alpha_3)$  used to find the parameters. Its minimum indicates the optimal point and the best parameter values. The shape of the function tells how well every parameter is identified and if there is a correlation between them. In this case, the objective function is a surface in a four-dimensional space, so it cannot be explicitly plotted. Instead, two-dimensional cross-sections of the function at the optimal point can be studied. The cross-section is taken along coordinate planes ( $\alpha_1, \alpha_2$ ), ( $\alpha_1, \alpha_3$ ) and ( $\alpha_2, \alpha_3$ ). Corresponding contour-plots are presented in Figure 12.



**Figure 12.** Sensitivity plots of estimated parameters for volumetric mass transfer coefficient.

Top row is for the square structure microreactor, bottom row – for the triangle microreactor. These plots indicate that the parameters are well-identified, although a slight correlation exists, especially between the  $\alpha_1$ - $\alpha_2$  and  $\alpha_1$ - $\alpha_3$  in both cases.

#### 2.4 Roles of CFD in prototype microreactor plate development

CFD has enormous potential for product and process development and optimization in chemical processes. It gives a comprehensive overview of the flow and therefore gives good insight into the phenomena occurring in the chemical process equipment. Many studies have reported successful application of CFD for full-scale modeling of different types of multiphase microreactors and micromixers (Al-Rawashdeha *et al.*, 2008; Chii-Dong *et al.*, 2011; Deshmukh *et al.*, 2004; Harries *et al.*, 2003; Qian and Lawal, 2006). However, most of these earlier studies are not applicable in this case. The flow in the microreactor is highly chaotic and unstable; therefore, in order to get statistically reliable results, it is necessary to simulate the flow in a large space span and average over time to eliminate the effect of randomness.

In this study, a CFD approach was used for microstructure optimization in full-scale modeling of the flow in the microreactor. The model described the hydrodynamics in the microreactor by accurately resolving the inertia, viscosity and surface tension forces. Detailed information on the simulations is given in publication IV.

A comparison of the flow patterns obtained from the model and experiments for both microreactors is presented in Figures 13 and 14. A white/bright color in the figures represents the gas phase and a black/dark color represents the liquid phase and structural elements. It can be seen that the two phase flow phenomena in the microreactor were adequately described by the developed model. The model was able to show small scale phenomena, such as separated gas bubbles of different size, liquid enclosures inside gas bubbles and liquid droplets on the structural elements.

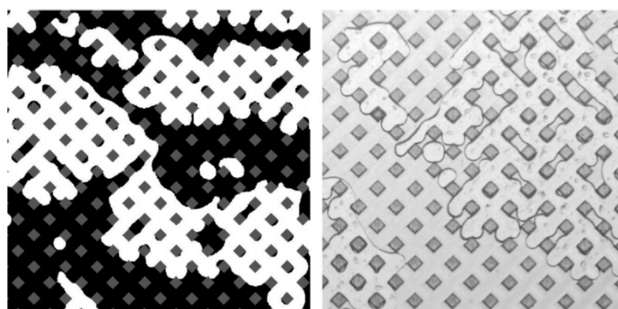


**Figure 13.** Comparison of flow patterns obtained from the model (left) and experiment (right) for the microreactor with rectangular microstructure.

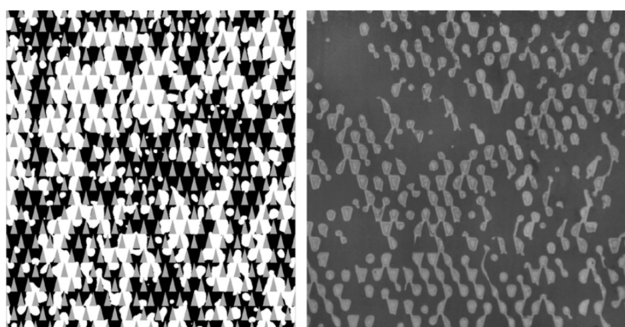


**Figure 14.** Comparison of flow patterns obtained from the model (left) and experiment (right) for the microreactor with triangular microstructure.

Additional quantitative comparison between the hydrodynamic parameters obtained from the simulations and experiments was done to validate the model. The images obtained from the experiment and CFD simulation were processed by an image processing routine written in Matlab to determine the gas-liquid interfacial area and gas holdup. Computed values are in relatively good agreement with the experiment. A comparison of the results is shown in Figure 15.

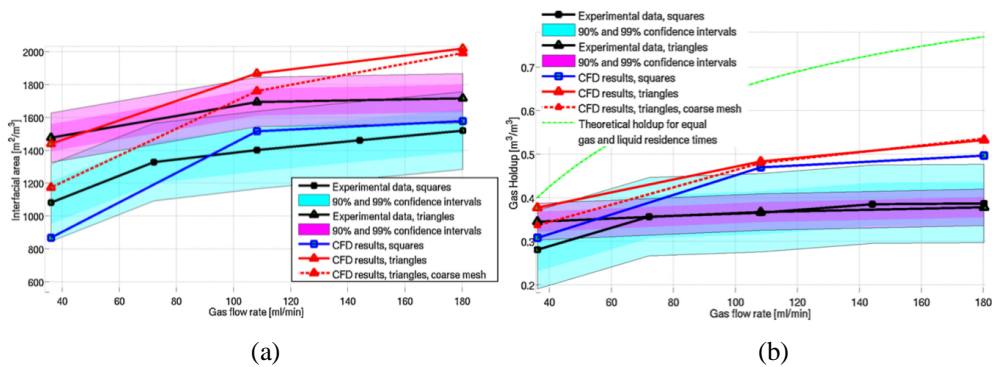


**Figure 15.** Comparison of the experimental and simulated results: gas-liquid interfacial area (a) and gas holdup (b).

The results from CFD study were implemented to the design of the microreactor. The prototype microreactor with triangular microstructure was selected based on these results.

## 2.5 Pressure drop in micro T-mixers

In this thesis work, pressure drop in micro T-mixers was studied to gain more insights on the hydrodynamics in microscale.

Pressure drop from the flow in a straight channel is determined by the friction factor, which is a function of the Reynolds number. Many attempts have been made to describe the relationship between the friction factor and the Reynolds number in microscale flow (Pfahler *et al.*, 1990; Yu *et al.*, 1995; Mala and Li, 1999; Qu *et al.*, 2000; Liu and Garimella, 2004). The studies have found that the friction factor in microscale flow differs from theoretical macroscale predictions. Therefore, conventional theory of pressure drop may not always be valid in microscale.

The micro T-mixer is widely used because it is a continuous mixer with a very simple geometry. The mixing efficiency of the T-micro mixer has been studied intensively over the last years (Engler *et al.*, 2004; Wong *et al.*, 2004; Bothe *et al.*, 2006). However, little emphasis has been placed on pressure drop measurement inside the mixers.

Micro T-mixers with different geometrical parameters were studied. The aims were to study the pressure drop of the liquid phase inside T-mixers and correlate it to friction factor, Reynolds number and the geometrical parameters of the T-mixers.

The study of pressure drop in micro T-mixers was done experimentally and a numerical approach was used to develop correlations. A set of numerical simulations were performed for different geometrical parameters and Reynolds number.

The scheme of the control volume for the calculation of the pressure drop is shown in Figure 16.  $L_y$  and  $L_x$  are defined as the length of the channels where the longitudinal component of the velocity is 99% of the fully developed velocity for inlet channels and mixing channels, respectively. Detailed information of the simulations is given in publication I.

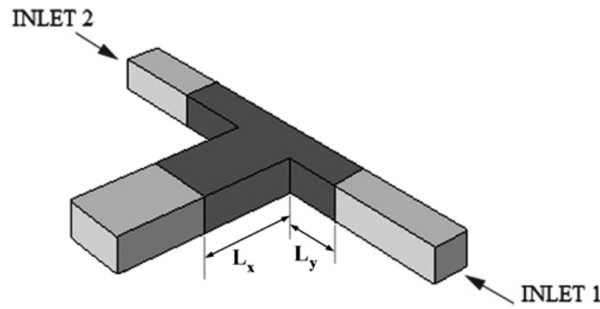


**Figure 16.** Control volume for numerical calculation of the pressure drop and friction factor.

Pressure loss inside the control volume is defined as the pressure drop resulting from deflection of the streamlines and is calculated as follows:

$$\Delta P = \left[ \frac{1}{2} (P_{m,1} + P_{m,2}) - P_{out} \right] - \left[ \frac{1}{2} (\Delta P_{s,1} + \Delta P_{s,2}) - P_s \right] \quad (6)$$

The friction factor,  $f$ , can be related to the pressure drop by

$$f = \frac{\left( \frac{\Delta P}{L} \right) Dh}{\rho U^2} \quad (7)$$

Analysis of the simulation data resulted in the following expression for the friction factor  $f$  in terms of the Reynolds number in the mixing channel ( $Re$ ) and the ratio between the hydraulic diameter of the mixing channel and inlet channels ( $D_r$ ). The correlation for the friction factor from numerical study can be described as follows:

$$f(\text{Re}, Dr) = \begin{cases} (0.0115Dr - 0.0152)\text{Re} + (44.86Dr - 47.66)\text{Re}^{-1} \\ + (-2.98Dr + 3.92) & \text{if } K < 100 \\ (-73.15Dr^2 - 2200Dr + 5362)\text{Re}^{-2.03} \\ + (0.0129Dr + 0.0761) & \text{if } K \geq 100 \end{cases} \quad (8)$$

Where  $K$  is the identification number describing the flow regime inside a micro T-mixer with different geometrical parameters developed by Soleymani *et al.* (2008).

Experimental investigations to measure the pressure loss in micro T-mixers were conducted to validate the numerical results. A series of experiments was performed to measure the pressure loss with increasing mass flow for two different micro T-mixers with the same hydraulic diameters. Their detailed dimensions are presented in Figure 17. The micro T-mixers were manufactured by micromachining using PTFE as the main construction material.

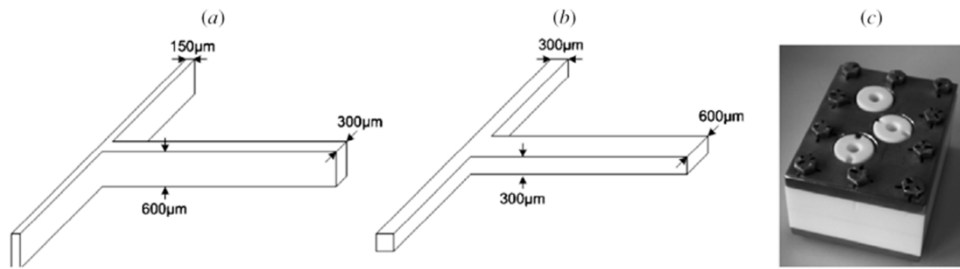


**Figure 17.** Geometric data of the micro T-mixers used in the experimental study; (a) T-mixer (1) of dimensions  $300 \times 150 \times 600$ ; (b) T-mixer (2) of dimensions  $600 \times 300 \times 300$ ; (c) housing of T-mixers.

A schematic drawing of the experimental set-up is presented in Figure 18. The liquid used in the experiments was deionized water at room temperature. The liquid was fed equally to both inlets through PTFE tubing. The total flow rate was in the range between  $0.72 \text{ ml min}^{-1}$  and  $6.71 \text{ ml min}^{-1}$ . The pressure drop over the micro T-mixer was measured by a differential pressure transmitter with the range of  $0 \dots 0.1 \text{ bar}$  and  $\pm 0.5\%$  full-scale accuracy.

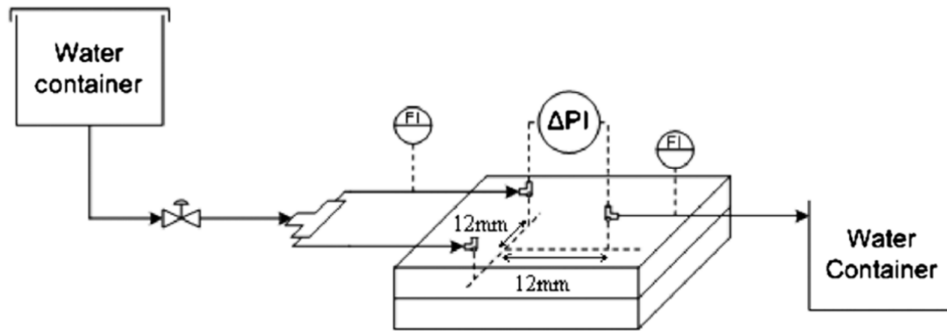


**Figure 18.** Schematic drawing of the experimental set-up.

Experimental results for the pressure loss,  $\Delta P$  are compared with those obtained from the proposed model (equations (1-3)) in Table 1. The model results for the pressure loss are consistent with observations from experiments at a wide range of Reynolds numbers. From Table 1, it can be concluded that the proposed model can accurately estimate the pressure drop inside the micro T-mixers over a wide range of dimensions of the mixer and Reynolds number.

**Table 2.** Pressure drop over the T-mixers obtained from the experiments and the proposed models.

Mixer chip ( $A \times B \times C$ )	Mass flow in the mixing channel, $\dot{m}(\text{g h}^{-1})$	$Re$ in the mixing channel	$\Delta P$ , from experiment (Pa)	$\Delta P$ , equations (3-9) (Pa)	Error%
$300 \times 150 \times 600$	39	24	16	15	+6.7%
$300 \times 150 \times 600$	52	32	20	19	+5.3%
$300 \times 150 \times 600$	117	72	37	39	-5.1%
$300 \times 150 \times 600$	136	84	61	64	-4.7%
$600 \times 300 \times 300$	194	120	162	152	+6.6%
$600 \times 300 \times 300$	233	144	201	211	-4.7%
$600 \times 300 \times 300$	130	80	69	74	-6.7%
$600 \times 300 \times 300$	259	160	311	287	+8.3%
$600 \times 300 \times 300$	324	200	542	517	+4.8%
$600 \times 300 \times 300$	350	216	610	628	-2.9%

### **3. Development of the catalyst**

Supported Pd catalysts are the most commonly used catalysts for direct synthesis (Solsona, 2006). The most common supports have been carbon, silica (high surface area materials), alumina and silica-alumina (relatively low surface area materials). Of these supports, activated carbon materials have resulted in best activity and selectivity. Pd on activated carbon has other additional advantages, e.g. chemical stability, availability, and easy recovery of Pd metal by burning off carbon components (Harada, 2006).

In this thesis, the effect of the oxidation state of the loaded metal, heat treatment of the catalysts in different atmospheres (H<sub>2</sub>, air) at different temperatures, surface chemistry of the support, and the catalytic activity were investigated. Different characterization methods were used to determine the surface chemistry of the support and the oxidation state of the metallic phase. The catalytic activities were investigated in an autoclave reactor.

In order to investigate the effect of the surface chemistry of the support, the support was pretreated before catalyst loading to introduce oxygen containing functional groups onto the surface. To investigate the effect of the oxidation state of the metallic phase and heat treatment on the catalytic performances, the catalysts were treated with different processes. The reduced catalysts were prepared under heat treatment with hydrogen at 185 °C and the calcined catalysts were prepared under heat treatment with air at temperatures of 135, 185, and 235 °C.

#### **3.1 Catalyst support**

Activated carbon cloth (ACC) was selected as a catalyst support. It is flexible and easily applicable, and it can be cut to proper size, bent and rolled to fit into any reactor geometry. A large specific surface area is available (over 2000 m<sup>2</sup>/g). The diameter of the fibers is small and uniform, ensuring that a good contact between the flowing fluid and the catalyst surface can be obtained and excellent mass transfer characteristics achieved (Yang, 2003).

ACC is available from many manufacturers and available with different properties. In this study, ACC was purchased from Kynol GmbH, Germany, and the model number was ACC507-15. The specific surface area (BET) is as high as 1500 m<sup>2</sup>/g and the fiber size 9.2 μm. The microstructure of the fiber is uniform with straight pores rather than branched ones as in granulated activated carbon.

### **3.2 Catalyst preparation**

A series of Pd/ACC catalysts was prepared by impregnation of Pd on ACC. The pretreatment of the support was done with 20 % nitric acid overnight. Acidic solution of PdCl<sub>2</sub> was used to prepare the catalysts. The detailed procedure is described in publication IV.

### **3.3 Catalyst tests**

#### **3.3.1 Catalyst characterization**

Surface chemistry of the support and oxidation state of the metallic phase was investigated by means of XPS, TPD, SEM, DTA and TGA tests. From the results, it can be concluded that the wet oxidation treatments with nitric acid introduced oxygen containing functional groups onto the surface of the ACC fibers. The oxidation state of the metallic phase was achieved by heat treatment. The metal phase on fresh virgin catalyst (without heat treatment) was mainly in metallic form (Pd<sup>0</sup>). After heat treatment by calcination, palladium oxide (PdO) could be found, and the amount of PdO increased with increasing temperature. In contrast, heat treatment by reduction did not lead to formation of PdO but seriously damaged the oxygen containing functional groups on the surface of the support.

#### **3.3.2 Catalyst activity**

The effect of the above-mentioned characteristics on catalytic activity for the direct synthesis was studied. The catalyst study was carried out in a stainless steel autoclave reactor (Parr Instruments Ltd) and the experimental setup is presented in Figure 19. The reactor was charged with about 55 mg of catalyst and successively with carbon dioxide up to 15.2 bar. The pressure was thereafter elevated to 20.2 bar with oxygen and further to 35.2 bar with carbon dioxide. Methanol was employed as a reaction medium. 175 g of methanol was pumped in and the reactor was cooled down to around -1 °C. When the desired temperature was reached, the partial pressure of hydrogen was raised by 3.2 bar. The reaction started immediately after feeding of hydrogen and the reaction time was 3 h. More detailed information on experiments is given in publication IV.

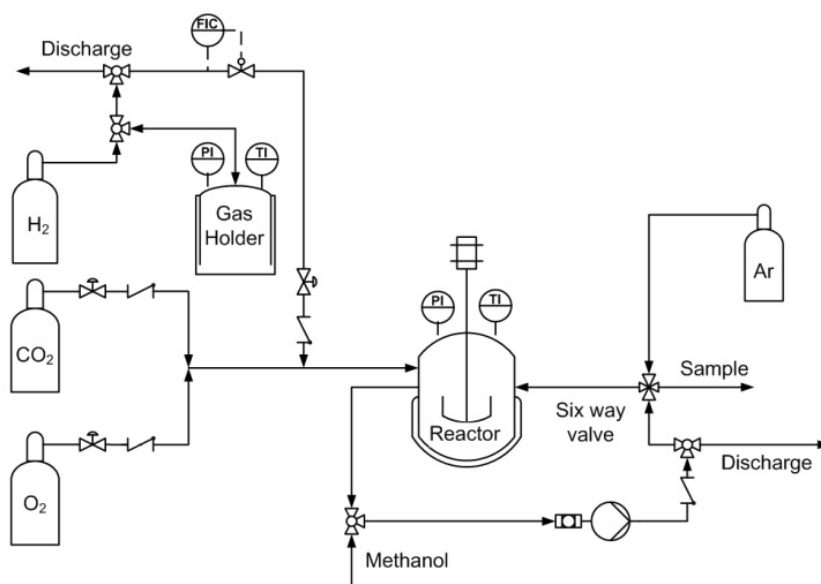


**Figure 19.** Experimental setup for catalyst study.

Oxidized and non-oxidized catalysts with different conditions of heat treatment were prepared and used in the experiments. The yield and selectivity were determined from each sample taken during the experiments, and yield and selectivity were defined as:

$$Yield(\%) = \frac{\text{Moles of Produced } H_2O_2}{\text{Moles } H_2 \text{ fed}} \times 100\% \quad (9)$$

$$Selectivity(\%) = \frac{\text{Moles of Produced } H_2O_2}{\text{Moles of consumed } H_2} \times 100\% \quad (10)$$

The results of direct synthesis over 3 wt.% Pd catalysts on oxidized and non-oxidized ACC are shown in Figure 20 and 21, respectively. Oxygen containing functional groups on the oxidized ACC improved the performance of the catalysts, making them considerably more selective for the direct synthesis than the non-oxidized samples. The oxidation state of the metallic phase found in the calcined catalysts exhibited higher activity and selectivity than the reduced catalysts. Heat treatment of the catalysts showed significant effect on the catalytic activity. Higher calcination temperature of the heat treatment of the catalysts supported on non-oxidized ACC improved the selectivity. Activity and selectivity were improved with the catalysts supported on oxidized ACC when increasing the calcination

temperature up to 185 °C, but further increase of the temperature led to a less selective catalyst.

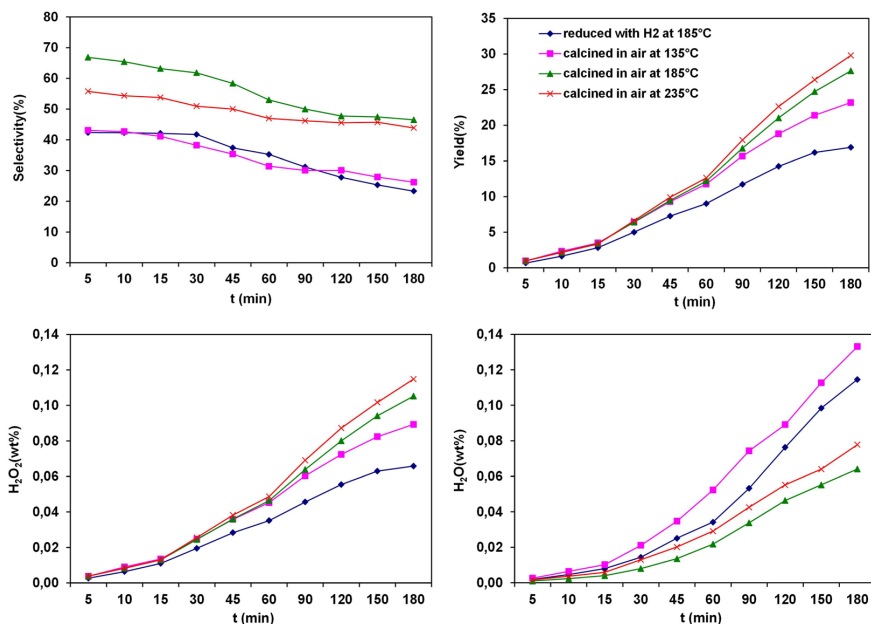


Figure 20. Performance of 3% Pd catalysts on oxidized ACC.

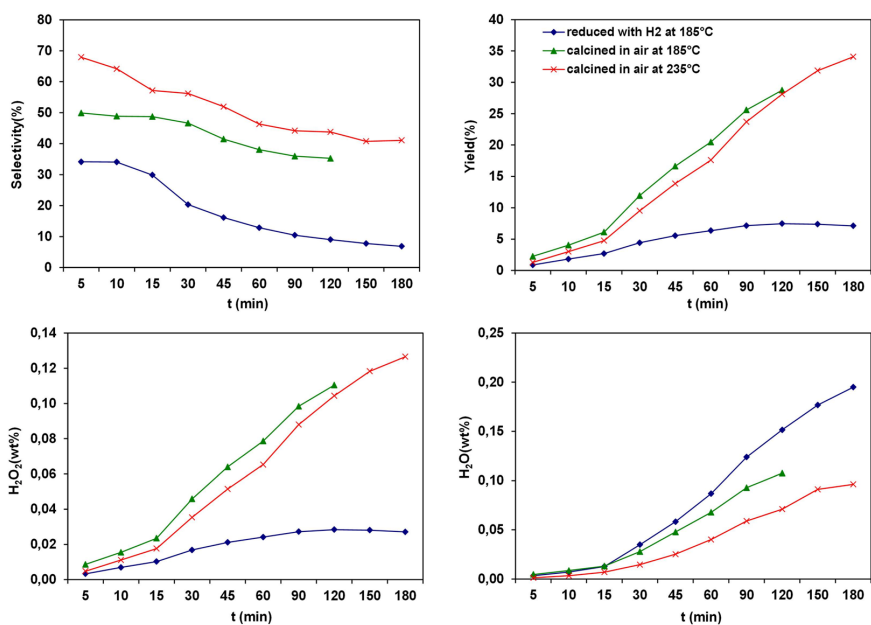


Figure 21. Performance of 3% Pd catalysts on non-oxidized ACC.

The results from the catalyst tests can be summarized as follows:

- Existence of the oxidized state of metal by heat treatment makes the catalyst more selective than the corresponding zerovalent state.
- Oxidized state of metal affects the selectivity of the direct synthesis by increasing the rate of H<sub>2</sub>O<sub>2</sub> production and simultaneously reducing the amount of water produced.
- Pretreatment of the support with nitric acid introduces oxygen-containing surface functional groups onto the surface, resulting in increased selectivity by reducing the rate of water production.

Pd catalysts supported on oxidized ACC that were calcined at 185 °C exhibited optimum performance for the direct synthesis in terms of activity and selectivity. These catalysts were therefore selected for tests in the microreactor.

#### **4. Development of a process for the direct synthesis of hydrogen peroxide**

Even though direct synthesis of hydrogen peroxide has been known since the beginning of the last century, there was not much research activity on direct synthesis until the 1980s, when environmental concerns started to become more important. The demand for hydrogen peroxide, a green oxidant, increased sharply and direct production once again became a focus of interest. DuPont started up a pilot plant but experienced frequent explosions in the pilot-scale reactor, which forced studies to be discontinued (Samanta, 2008).

During the last decade, advances in reactor technology and catalysts have led to renewed industrial interest and academic research in direct synthesis. Highly active and selective catalyst for direct synthesis have been tested by many research groups in a variety of reactors. Direct synthesis in a conventional batch reactor has been investigated by a number of authors (Burch and Ellis, 2003; Gudarzi *et al.*, 2010; Monero *et al.*, 2010; Biasi *et al.*, 2012b; Gemo *et al.*, 2012a; Gudarzi *et al.*, 2013). Some studies have been conducted in continuous systems using trickle bed reactors (Biasi *et al.*, 2010, 2011, 2012a). Another promising approach had been the use of a membrane-based catalyst to avoid direct contact between H<sub>2</sub> and O<sub>2</sub> (Choudhary *et al.*, 2001).

A microreactor is inherently safe by virtue of its small reaction space, which suppresses the occurrence of explosions. Several studies during the last decade have focused on utilizing this benefit of microreactors for direct synthesis. The simplest microreactor is a single channel microreactor and such reactors have been studied by Voloshin *et al.* (2007), Wang *et al.* (2007), Maehara *et al.* (2008) and Lawal *et al.* (2010). Some studies have been conducted in the explosive regime (Voloshin *et al.*, 2007; Wang *et al.*, 2007; Inoue *et al.*; 2010, 2013) and sometimes small explosions have been detected (Inoue *et al.*, 2010).

##### **4.1 Microreactor**

In this thesis work, a microreactor for a bench-scale process was designed and constructed based on findings from hydrodynamics and mass transfer studies in prototype microreactor plates. A triangular microstructure was selected and several modifications were made to the prototypes to improve the fluid distribution in the reactor.

The configuration of the microreactor is shown in Figure 22. The microreactor is made of stainless steel and consists of several sections. The reactor plate is installed in a vertical position and the inlets for the gas and liquid feeds are located at the top section. A bifurcation

configuration was used for the liquid feed to improve the distribution and prevent channeling problems. The gas feed takes place through the cover plate, which is installed against the microreactor plate. The microstructure section is located below the inlet section. The width of this section is 32 mm, height 300 mm and depth 300  $\mu\text{m}$ . The microstructure consists of a number of triangular elements (see Fig.2). The size of each element is 1 mm  $\times$  2 mm  $\times$  300  $\mu\text{m}$  (base  $\times$  height  $\times$  depth). The elements are arranged in staggered arrays providing a fraction of free space of 0.75. The holdup for the gas/liquid mixture was 3.84  $\text{cm}^3$ . The microstructure was designed to improve the mixing of the two phases and to generate a high interfacial area. Below the microstructure section is the catalyst bed. A Pd catalyst supported on active carbon cloth was fixed in this section.

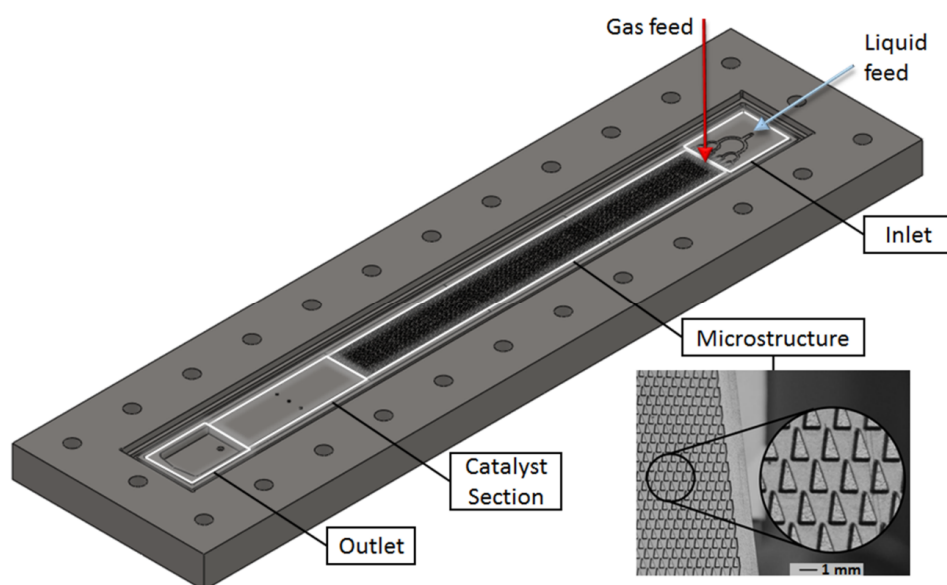


**Figure 22.** Microreactor plate.

#### 4.2 Experimental setup

A continuous bench scale process was used for the direct synthesis, shown in Figure 23. The stainless steel equipment was initially passivated with 20% citric acid at 333.15 K for 12 h to minimize the decomposition of hydrogen peroxide. Methanol was used as a solvent, allowing higher solubility of gases. The solvent was saturated with oxygen in a saturation vessel at 20 bar. Excess of oxygen gas was used in order to also strip away dissolved carbon dioxide and hydrogen left in the recycled solvent. The vessel was cooled to maintain solvent temperature at 273.15 K. From the saturation vessel, solvent with dissolved oxygen was fed into the

microreactor together with a mixture of CO<sub>2</sub> and H<sub>2</sub> (95%/5%). The fluids flowed concurrently downwards in the reactor. At the bottom, the gas and liquid phase were separated by gravity. Pressure was controlled by the gas outflow. Part of the outflowing liquid was taken as a product and the rest was recycled back to the saturation vessel. To maintain constant volume of liquid in the system, an equal amount of solvent was added to the saturation vessel as taken away as product stream after the reactor. The instrumentation is shown in Figure 23.

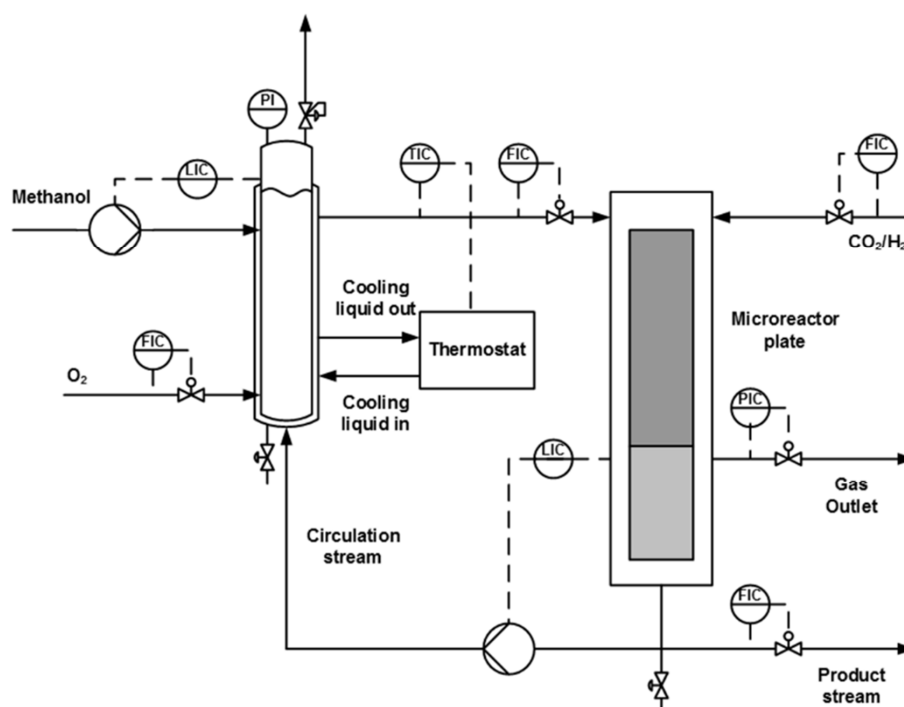


**Figure 23.** Experimental setup.

### 4.3 Experimental procedure

Typical conditions in the reactor were 273.15 K and 20 bar. At the beginning of the procedure, the saturation vessel was filled with methanol (0.35 l). Cooling of the liquid was started by feeding ethylene glycol through the jacket of the saturation vessel. Oxygen flow through the saturation vessel was then initiated. A gas sparger was utilized to achieve sufficient gas-liquid interface. Next, circulation of saturated solvent through the process was started and the pressure of the reactor was raised by feeding inert gas into the reactor. Once the required conditions had been attained, the inert gas feed was changed to the mixture of CO<sub>2</sub> and H<sub>2</sub> and the reaction started.

The variables in the experiments were flow rate of liquid feed into the reactor, flow rate of gas feed into the reactor, pressure, concentration of Pd in the catalysts and amount of catalyst. In addition, two alternative inert gases, CO<sub>2</sub> and N<sub>2</sub>, were utilized to dilute the hydrogen feed. The temperature was constant, 273.15 K.

In each experiment, samples were taken from the product stream and the concentration of hydrogen peroxide and water was determined in each sample. Iodometric titration was used for hydrogen peroxide and Karl-Fischer titration for water. The selectivity was calculated according to Equation (10).

#### **4.4 Catalyst**

Using ACC as a catalyst support provided certain benefits for the plate-type microreactor. Because ACC is a fabric-type support, it can be placed directly between the reaction plate and the cover plate. Thus, replacement and regeneration of the catalyst is easily done by opening the reactor and removing the ACC. Packing problems are less significant than with conventional granulated or powder catalysts.

Pd catalysts supported on oxidized ACC were selected for the tests in the microreactor. The palladium loading was in the range 1-5 wt.%. The catalysts were calcined at 185 °C.

SEM images of catalysts with different Pd loading are shown in Figure 24. The white spots represent metal particles, which are well distributed throughout the ACC fibers. From the images it can be seen that Pd loading up to 1 wt.% mainly occurred inside the micropores of the ACC, because no particles can be detected on the outer surface of the ACC. Increasing the amount of Pd led to development of large Pd particles on the outer surface (Gudarzi *et al.* 2013).

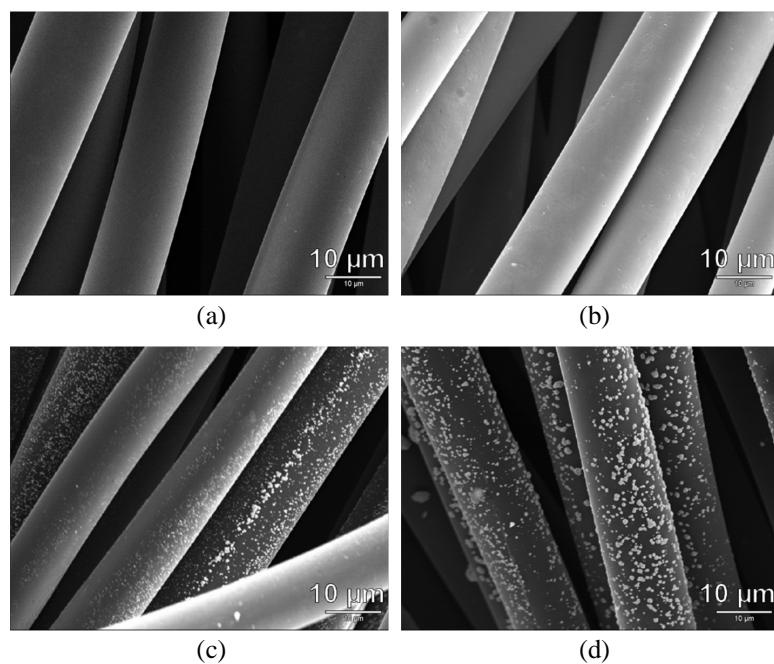


**Figure 24.** SEM images for the catalysts used in this study; 0 wt.% (a), 1 wt.% (b) 3 wt.% (c), and 5 wt.% (d).

## 4.5 Results

### 4.5.1 Long-term experiments

In these experiments, the effects of two inert gases,  $N_2$  and  $CO_2$ , were studied. Nitrogen has low solubility and has no effect on the reaction solvent. Carbon dioxide, on the other hand, dissolves in the solvent and acidifies in the presence of water. The solubility of the reactant gases is enhanced because of good affinity with carbon dioxide (Gemo, 2012b). Acidic conditions also promotes the stability of the hydrogen peroxide produced (Edwards, 2008).

The experiments were conducted at different pressure levels. The results at high pressure were better because more reactants dissolved in the liquid phase. Analyzed concentration of  $H_2O_2$  in the product streams is shown in Figure 25.

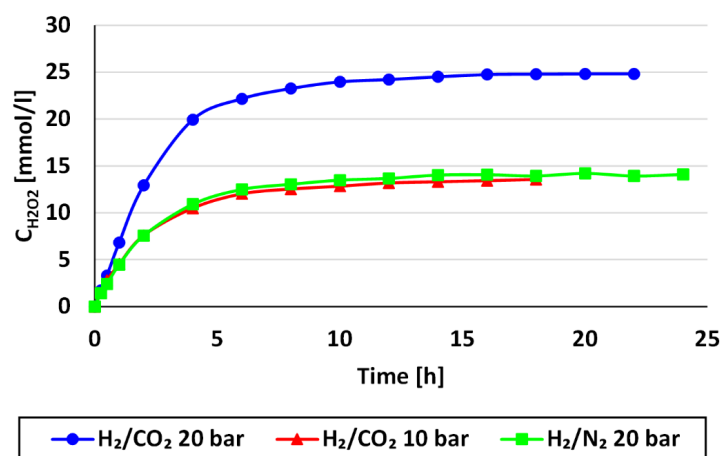


**Figure 25.** Concentration of H<sub>2</sub>O<sub>2</sub> in long-term experiments.

The cumulative amount of H<sub>2</sub>O<sub>2</sub> produced (mmol) as a function of time is shown in Figure 26. The upper curve represents the real cumulative H<sub>2</sub>O<sub>2</sub> production (mmol) and the lower one describes the cumulative H<sub>2</sub>O<sub>2</sub> (mmol) in the process circulation.

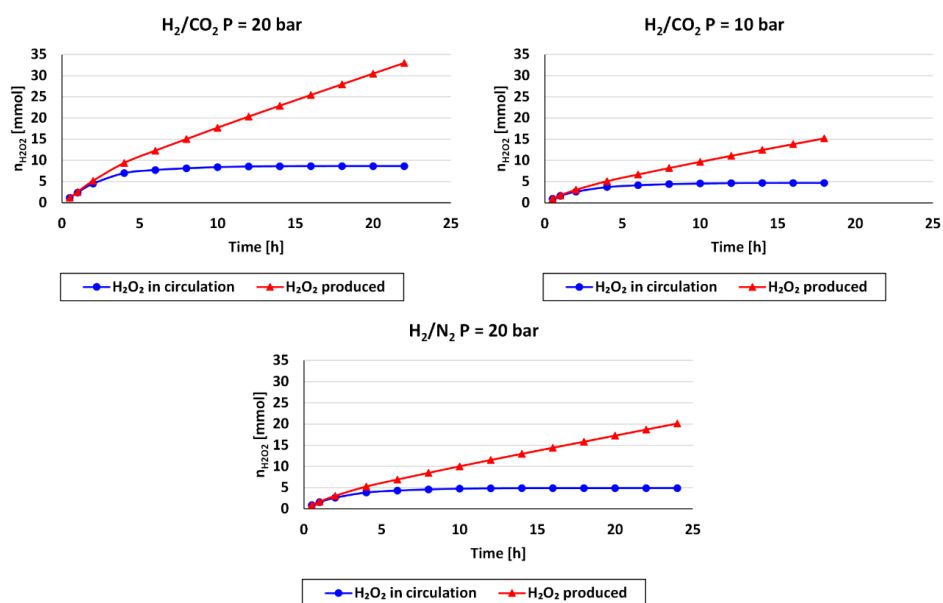


**Figure 26.** Cumulative amount of H<sub>2</sub>O<sub>2</sub> produced.

The total production rate of H<sub>2</sub>O<sub>2</sub> in the reactor (mmol/h) is shown in Figure 27. This is also shown per mass of Pd (mmol/h/g<sub>Pd</sub>).

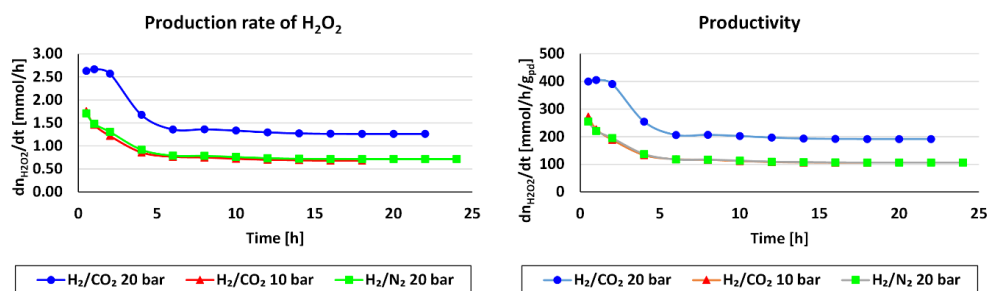


**Figure 27.** Production rate of H<sub>2</sub>O<sub>2</sub> in the reactor.

Selectivity in the long-term experiments is shown in Figure 28. The value was highest at the beginning of the experiment. As the reaction proceeded, the produced hydrogen peroxide was further hydrogenated and decomposed to water, which lead to a decrease in selectivity. Selectivity was best in the system with CO<sub>2</sub> at higher pressure. As noted above, CO<sub>2</sub> improves the solubility of the reactants and stabilizes the hydrogen peroxide produced.

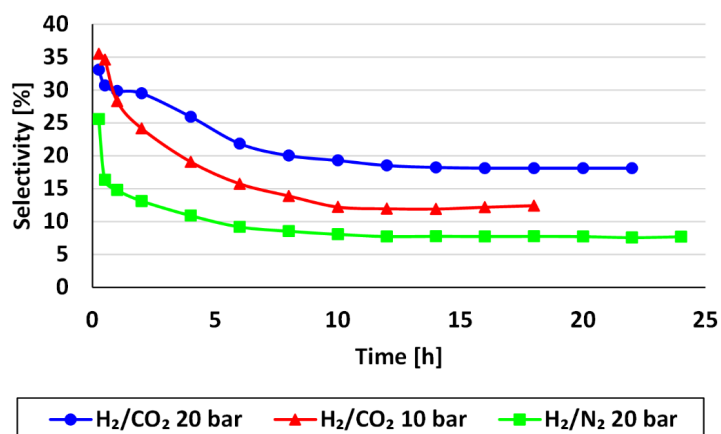


**Figure 28.** Selectivity.

#### 4.5.2 Effect of the process conditions

The effects of feed rate, gas/liquid ratio, amount of Pd loading and amount of catalyst were studied. The experiments were run with a residence time of 6 hours. Concentration of H<sub>2</sub>O<sub>2</sub> and selectivity were determined. Detailed information about the experimental conditions are described in publication V. The results can be summarized as follows:

### *Effect of feed rate*

Experiments were done with different liquid feed rates while the gas/liquid ratio was kept constant. The results are presented in Figure 29. It can be seen from the results that both concentration of  $\text{H}_2\text{O}_2$  and selectivity seem to increase as a function of liquid feed rate. At higher liquid feed rates, the hydrodynamical conditions in the catalyst bed could be enhanced, causing better contact and liquid/solid mass transfer. The gas/liquid mass transfer could be improved by higher gas/liquid flow rates as well.

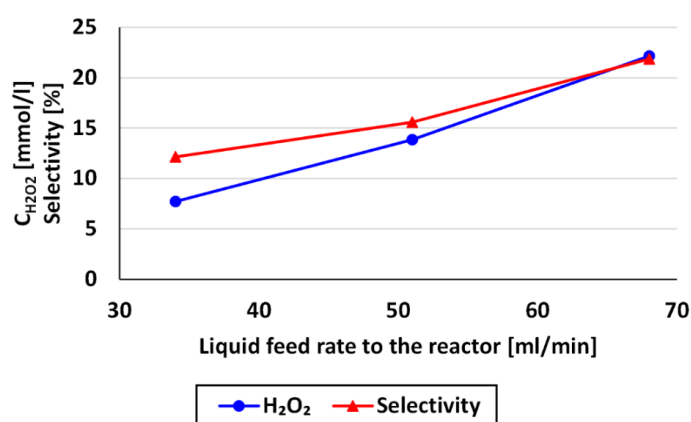


**Figure 29.** Effect of liquid feed rate.

### *Effect of gas/liquid feed ratio*

The effect of the gas/liquid feed ratio was studied by changing gas flow rate (at 273.15 K and 20 bar) while keeping the liquid flow rate constant. The results of the experiments are shown in Figure 30. The increase in  $\text{H}_2\text{O}_2$  concentration with increasing hydrogen feed is understandable. The decrease in selectivity can be explained by enhanced decomposition of  $\text{H}_2\text{O}_2$  via hydrogenation (see Figure 3).

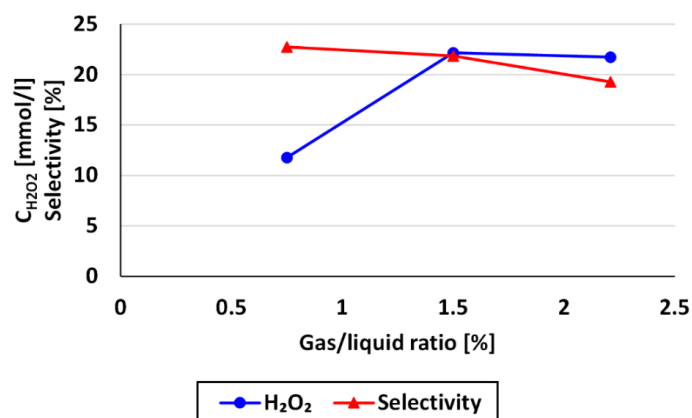


**Figure 30.** Effect of gas/liquid feed ratio.

*Effect of Pd loading*

The catalysts were prepared with 1 wt.%, 3 wt.%, and 5 wt.% Pd loading. In the case of the 1 wt.% Pd catalyst, almost all the Pd particles were located inside micropores, which are more difficult to access for the reactants. After increasing the amount of Pd to 3 wt.%, particles started to develop on the outer surface of the carbon fibers, which is easily accessible for the reactants. Further increase of Pd loading to 5 wt.% did not increase the number of active sites; it merely led to bigger particles on the outer surface of the carbon fibers. For this reason, the concentration of hydrogen peroxide did not increase with Pd loading greater than 3 wt.% (Gudarzi *et al.*, 2013). The results of the effect of Pd loading are shown in Figure 31.

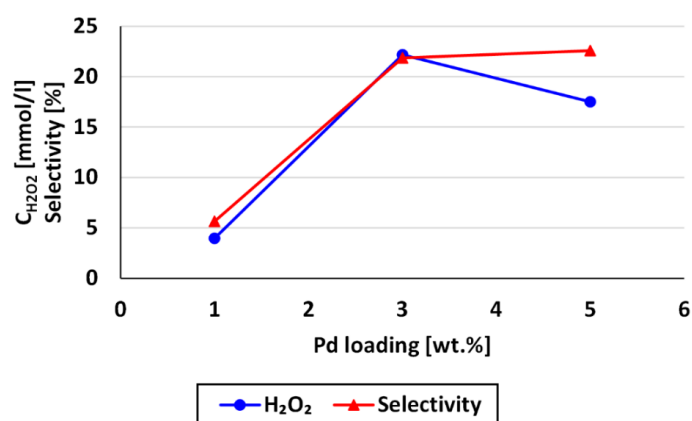


**Figure 31.** Effect of Pd loading.

### *Effect of the amount of catalyst*

The hydrogen peroxide concentration and selectivity decreased when increasing the amount of catalyst. The produced hydrogen peroxide might be hydrogenated or decomposed to water by the extra catalyst. The results are shown in Table 3.

**Table 3** Effect of the amount of catalyst.

Amount of catalyst [g]	H <sub>2</sub> O <sub>2</sub> Concentration [mmol/l]	Selectivity [%]
0.21	22.16	21.85
0.42	14.18	16.00

### **4.6 Possible directions for further development of the process**

A bench-scale process has been developed and it showed promising performance for the direct synthesis of hydrogen peroxide. The reactor introduced in this thesis was designed for research purposes. A commercial reactor of the same process would need to be slightly different.

A full scale reactor would have to contain several parallel reactor plates. Moreover, the height of the plates would be longer, probably consisting of alternating sections for mixing and catalytic sections and there would be gas feeds to each catalytic section. In general, both the location and the composition of the gas feeds would differ from the arrangement in the research unit presented. Further studies are needed to find out if the microreactor approach could allow the safe use of a gas mixture in explosive concentration ranges (Voloshin *et al.*, 2007; Wang *et al.*, 2007; Inoue *et al.*; 2010, 2013). This would enable more favorable gas concentration and lead to substantially higher yields.

Further development of the catalyst would provide improvement to the yield and selectivity. In recent studies (Edwards *et al.*, 2005; Biasi *et al.*, 2011; Freakley *et al.*, 2013), it has been found that the addition of Au to Pd catalysts can significantly increase the activity and selectivity of the catalyst.

A commercial process would include a separation unit after the microreactor, where hydrogen peroxide is separated from methanol. This can be done by distillation or by more novel methods, for instance, membrane-based separation.

## 5. Conclusions

Direct synthesis is a sustainable alternative process for hydrogen peroxide production. The direct synthesis process does, however, face challenges such as safety and selectivity problems. Advances in reactor technology and catalysts provide a promising opportunity for process development. The novel microreactor and a new type of catalyst discussed in this thesis show potential for the direct synthesis of hydrogen peroxide.

The novel type of microstructured reactor plate developed provided certain benefits, i.e. less severe plugging problem and easy catalyst changing and regeneration. CFD has proven to be a beneficial tool for microstructure design and optimization. The developed CFD model could correctly resolve the flow in the microreactor, giving results that were in good agreement with experimental measurements.

The design of the microstructure and optimization of flow rates are important for favorable hydrodynamic and mass transfer behaviors in the microreactor. The hydrodynamics and mass transfer performances of the developed microreactor were considerably better than in conventional multiphase reactors. The total interfacial area and mass transfer coefficient were relatively high. Empirical correlations for the mass transfer coefficient were derived.

A new type of Pd catalyst supported on ACC was developed. Such catalysts provide certain benefits for use in plate-type microreactors, for example, catalyst fixing and regeneration are easy because of their flexibility. It was found during the catalyst study that the oxidized state of the support and the metallic phase of the catalyst has significant roles in catalytic activity and selectivity. During the catalyst preparation, pretreatment of the support by acid introduces oxygen surface functional groups, which makes the Pd catalyst more selective. The metallic phase of the catalyst, obtained by heat treatment, improves both yield and selectivity. Optimum conditions for catalyst preparation were derived from the study.

The direct synthesis of hydrogen peroxide was carried out in a bench-scale process using the developed microreactor and catalysts. The effect of the process conditions on productivity and selectivity were studied and promising results were achieved. The study demonstrated that the bench-scale process can be effectively and safely used for laboratory tests on the direct synthesis of hydrogen peroxide. The question of whether the microreactor might have potential for operation with gas mixtures in the explosive regime requires further investigation. Reactor and feed system modifications and a separation unit would be needed

to achieve higher concentrations of hydrogen peroxide. It should be noted that the process was designed to produce information for research and development purposes. A commercial full-scale unit would have different design criteria and slightly different operation conditions.

## References

- Al-Rawashdeha M., Hessela V., Loba P., Mevissena K., Schonfelda F. (2008). Pseudo 3-D simulation of a falling film microreactor based on realistic channel and film profiles. *Chemical Engineering Science*, 63, 5149–5159.
- Baukal Jr. C.E. (1998). *Oxygen-Enhanced Combustion*, CRC, New York.
- Biasi P., Canu P., Menegazzo F., Pinna F. and Salmi T.O., (2012a). Direct synthesis of hydrogen peroxide in a trickle bed reactor: comparison of Pd-based catalysts, *Industrial Engineering Chemistry Research*, 51, 8883-8890.
- Biasi P., Gemo N., Carucci J.R.H., Eränen K. and Canu P. (2012b). Kinetics and mechanism of H<sub>2</sub>O<sub>2</sub> direct synthesis over Pd/C catalyst in a batch reactor, *Industrial Engineering Chemistry Research*, 51, 8903-8912.
- Biasi P., Menegazzo F., Pinna F., Eränen K., Salmi T.O. (2011). Continuous H<sub>2</sub>O<sub>2</sub> direct synthesis over PdAu catalysts, *Chemical Engineering Journal*, 176-177, 172-177.
- Biasi P., Menegazzo F., Pinna F., Eränen K., Canu P. and Salmi T.O. (2010). Hydrogen peroxide direct synthesis: selectivity enhancement in a trickle bed reactor, *Industrial Engineering Chemistry Research*, 49 10627-10632.
- Bothe, D., Stemich, C., Warnecke, H. (2006). Fluid mixing in a T-shaped micro-mixer, *Chemical Engineering Science*, 61, 2950–2958.
- Burch R., Ellis P.R., (2003). An investigation of alternative catalytic approaches for the direct synthesis of hydrogen peroxide from hydrogen and oxygen, *Applied Catalysis B: Environmental*, 42, 203-211.
- Campos-Martin, J.M., Blanco-Brieva, G., Fierro, J.L.G. (2006). Hydrogen peroxide synthesis: An outlook beyond the anthraquinone process, *Angewandte Chemie International Edition*, 45, 6962-6984.
- Centi, G., Perathoner, S., Abate, S., Mizuno, N. (Eds.) (2009). *Modern Heterogeneous Oxidation Catalysis: Design, Reactions and Characterization*, Wiley-VCH, Weinheim.
- Chii-Dong H., Hsuan C., Hsi-Jen C., Cheng-Liang C., Hsieh-Hsung L., Yin-Yu C. (2011). CFD simulation of the two-phase flow for a falling film microreactor. *International Journal of Heat and Mass Transfer*, 54, 3740–3748.
- Choudhary V.R., Gaikwad A.G., Sansare S.D. (2001). Nonhazardous Direct Oxidation of Hydrogen to Hydrogen Peroxide Using a Novel Membrane Catalyst, *Angewandte Chemie International Edition*, 40 (9), 1776-1779.

- Coleman, J.W., Garimella, S. (1999). Characterization of two-phase flow patterns in small diameter round and rectangular tubes, *International Journal of Heat and Mass Transfer*, 42, 2869-2881.
- Deshmukh, S.R., Mhadeshwar, A.B., Vlachos, D.G. (2004). Microreactor modeling for hydrogen production from ammonia decomposition on ruthenium. *Industrial and Engineering Chemical Research*, 43, 2986–2999.
- Edwards, J.K., Hutchings, G.J. (2008). Palladium and Gold–Palladium Catalysts for the Direct Synthesis of Hydrogen Peroxide, *Angewandte Chemie International Edition*, 47, 9192-9198.
- Edwards, J.K., Solsona, B.E., Landon, P., Carley, A.F., Herzing, A., Kiely, C.J. and Hutchings, G.J. (2005). Direct synthesis of hydrogen peroxide from H<sub>2</sub> and O<sub>2</sub> using TiO<sub>2</sub>-supported Au-Pd catalysts, *Journal of Catalysis*, 236, 69-79.
- Engler, M., Kockmann, N., Kiefer, T. and Woias, P. (2004). Numerical and experimental investigations on liquid mixing in static micromixers, *Chemical Engineering Journal*, 101, 315–322.
- Ehrfeld, W., Hessel, V., Löwe, H. (2002). *Microreactors: New Technology for Modern Chemistry*, WILEY-VCH, Weinheim.
- Elvers, B., Hawkins, S., Ravenscroft, M., Schulz, G. (Eds.) (1989). *Ullmann's Encyclopedia of Industrial Chemistry, Vol. A13: Hydrogen peroxide*, VCH, Weinheim.
- Freakley, S.J., Piccinini, M., Edwards, J. K., Ntainjua, E.N., Moulijn, J. A., Hutchings, G.J. (2013). Effect of reaction conditions on the direct synthesis of hydrogen peroxide with a AuPd/TiO<sub>2</sub> catalyst in a flow reactor, *ACS Catalysis*, 3 487-501.
- Gemo, N., Biasi, P., Canu, P. and Salmi, T.O. (2012a). Mass transfer and kinetics of H<sub>2</sub>O<sub>2</sub> direct synthesis in a batch slurry reactor, *Chemical Engineering Journal*, 207-208, 539-551.
- Gemo, N., Biasi, P., Salmi, T.O., Canu, P. (2012b). H<sub>2</sub> solubility in methanol in the presence of CO<sub>2</sub> and O<sub>2</sub>, *Journal of Chemical Thermodynamics*, 54, 1-9.
- Gudarzi, D., Ratchanansorn, W. and Turunen, I. (2013). Preparation and study of Pd catalysts supported on activated carbon cloth (ACC) for direct synthesis of H<sub>2</sub>O<sub>2</sub> from H<sub>2</sub> and O<sub>2</sub>, *Topics in Catalysis*, 56, 527-539.
- Gudarzi D., Simokova O.A., Carucci J.R.H., Biasi P., Eränen K., Kolehmainen E., Turunen I., Murzin D.Y., Salmi T. (2010). Direct synthesis of H<sub>2</sub>O<sub>2</sub> from H<sub>2</sub> and O<sub>2</sub> over carbon supported Au, Pd and Au-Pd/C bimetallic catalysts, *Chemical Engineering Transactions*, 21, 925-930.
- Harada, T., Ikeda, S., Miyazaki, M., Sakata, T., Mori, H., Matsumura, M. (2007). A simple method for preparing highly active palladium catalysts loaded on various carbon supports for

- liquid-phase oxidation and hydrogenation reactions, *Journal of Molecular Catalysis A: Chemical*, 268 (1-2), 59-64.
- Harries, N., Burns, J.R., Barrow, D.A., Ramshaw, C. (2003). A numerical model for segmented flow in a microreactor. *International Journal of Heat and Mass Transfer*, 3313–3322.
- Hessel, V., Hardt, S., Löwe, H. (2004). *Chemical Micro Process Engineering: Fundamentals, Modelling and Reactions*, Wiley-VCH GmbH & Co, Weinheim.
- Inoue, T., Kikutani, Y., Hamakawa, S., Mawatari, K., Mizukami, F., Kitamori, T. (2010). Reactor design optimization for synthesis of hydrogen peroxide, *Chemical Engineering Journal*, 160, 909-914.
- Inoue, T., Ohtaki, K., Murakami, S., Matsumoto, S. (2013). Direct synthesis of hydrogen peroxide based on microreactor technology, *Fuel Processing Technology*, 108, 8-11.
- Jensen, K. F. (2001) Microreaction engineering – is small better?, *Chemical Engineering Science*, 56, pp.293-303.
- Jones, C.W., Clark, J.H. (1999). *Applications of Hydrogen Peroxide and Derivatives*, The Royal Society of Chemistry, Cambridge.
- Kawahara, A., Chung, P.M.Y., Kawaji, M. (2002). Investigation of two-phase flow pattern, void fraction and pressure drop in a microchannel. *International Journal of Multiphase Flow*, 28, 1411-1435.
- Liu, D, Garimella, S (2004). Investigation of liquid flow in microchannels, *Journal of Thermophysics and Heat Transfer*, 18, 65–72.
- Losey, M.W., Rebecca, J., Firebaugh, S.L., Schmidt, M.A., Jensen, K.F. (2002). Design and fabrication of microfluidic devices for multiphase mixing and reaction, *Journal of Microelectromechanical Systems*, 11, 709-717.
- Losey, M.W., Schmidt, M.A., Jensen, K.F. (2001). Microfabricated multiphase packed-bed reactor: Characterization of mass transfer and reactions, *Industrial Engineering Chemistry Research*, 40, 2555-2562.
- Maehara, S., Taneda, M., Kusakabe, K. (2008). Catalytic synthesis of hydrogen peroxide in microreactors, *Chemical Engineering Research and Design*, 86, 410-415.
- Mala, G.M., Li, D. (1999). Flow characteristics of water in microtubes, *International Journal of Heat and Fluid Flow*, 20, 142–148.
- Moreno, T., García-Serna, J. and Cocero, M.J. (2010). Direct synthesis of hydrogen peroxide in methanol and water using scCO<sub>2</sub> and N<sub>2</sub> as diluents, *Green Chemistry*, 12, 282-289.

- Pfahler, J.N., Harley, J., Bau, H., Zemel, J. (1989). Liquid transport in micron and submicron channels, *Sensors and Actuators A: Physical*, 22 (1-3), 431–434.
- Pohorecki, R. (2007). Effectiveness of interfacial area for mass transfer in two-phase flow in microreactors, *Chemical Engineering Science*, 62, 6495-6498.
- Pohorecki, R., Sobieszuk, P., Kula, K., Moniuk, W., Zieliński, M., Cygański, P., Gawiński, P. (2008). Hydrodynamic regimes of gas-liquid flow in a microreactor channel, *Chemical Engineering Journal*, 135S, 185-190.
- Qian, D., Lawal, A. (2006). Numerical study on gas and liquid slugs for Taylor flow in a T-junction microchannel. *Chemical Engineering Science*, 61, 7609–7625.
- Qu, W., Mala, G.M., Li, D. (2000). Heat transfer for water flow in trapezoidal silicon microchannels, *International Journal of Heat and Mass Transfer*, 43, 3925–3936.
- Samanta, C. (2008). Direct synthesis of hydrogen peroxide from hydrogen and oxygen: An overview of recent developments in the process, *Applied Catalysis A: General*, 350, 133-149.
- Solsona, B.E., Edwards, J.K., Landon, P., Carley, A.F., Herzing, A., Kiely, C.J., and Hutchings, G.J. (2006). Direct Synthesis of Hydrogen Peroxide from H<sub>2</sub> and O<sub>2</sub> Using Al<sub>2</sub>O<sub>3</sub> Supported Au–Pd Catalysts, *Chemistry of Materials*, 18(11), 2689-2695.
- Stankiewicz, A.I., Moulijn, J.A. (2000). Process intensification: transforming chemical engineering. *Chemical Engineering Progress*, 96, 22–33.
- Voloshin, Y., Halder, R., Lawal, A. (2007). Kinetics of hydrogen peroxide synthesis by direct combination of H<sub>2</sub> and O<sub>2</sub> in a microreactor, *Catalysis Today*, 125, 40-47.
- Waelchli, S., Rohr, P.R. von (2006). Two-phase flow characteristics in gas-liquid microreactors, *International Journal of Multiphase Flow*, 32, pp.791-806.
- Wang, X., Nie, Y., Lee, J.L. and Jaenicke, S. (2007) Evaluation of multiphase microreactors for the direct formation of hydrogen peroxide, *Applied Catalysis A: General*, 317, 258-265.
- Wong, S.H., Ward, M.C.L., Wharton, C. (2004). Micro T-mixers as a rapid mixing micromixer, *Sensors and Actuators B: Chemical*, 100, 359-379.
- Yang, R. T. (2003). *Adsorbents: Fundamentals and Applications*, John Wiley & Sons Inc., New Jersey.
- Yu, D., Warrington, R., Barron, R. and Ameal, T. (1995). An experimental and theoretical investigation of fluid flow and heat transfer in microtubes, *Proceedings ASME/JSME Thermal Engineering Joint Conference* (Maui, Hawaii), pp 523–530.



## **Publication I**

Soleymani, A., Yousefi, H., Ratchananusorn, W., Turunen, I. (2010)  
Pressure drop in micro T-mixers  
*Journal of Micromechanics and Microengineering*, 20, 15029-15035

Reprinted by permission of IOP Publishing  
© IOP Publishing



# Pressure drop in micro T-mixers

A Soleymani<sup>1</sup>, H Yousefi, W Ratchananusorn and I Turunen

Department of Chemical Technology, Lappeenranta University of Technology, 53851 Lappeenranta, Finland

E-mail: azita@lut.fi

Received 3 September 2009

Published 8 December 2009

Online at stacks.iop.org/JMM/20/015029

## Abstract

Results are presented from a numerical study examining the pressure drop of the liquid phase inside micro T-mixers at moderate Reynolds numbers. The effects on the pressure gradient of changes to design and operating parameters such as the aspect ratio of the mixing channel and the volume flow rate are studied. To understand the influence of geometrical parameters on flow resistance and the mixing zone, a wide range of dimensions of micro T-mixers is studied. A broad range of Reynolds numbers is investigated so that the flow is either in the vortex or in the engulfment regimes. Explicit equations are proposed to predict the friction factor for both vortex and engulfment flow regimes inside T-mixers. In addition, a model is proposed to determine the mixing zone in micro T-mixers. A set of experiments were carried out to support the simulation results. The model results were found to be consistent with the experimental findings.

(Some figures in this article are in colour only in the electronic version)

## Nomenclature

$A$	width of the mixing channel
$B$	width of the inlet channels
$C$	depth of all the channels
$D_h$	hydraulic diameter of the mixing channel
$D_{h\_in}$	hydraulic diameter of the inlet channels
$D_{h\_A/2}$	hydraulic diameter of a rectangular surface of dimensions $\frac{A}{2} \times C$
$f$	friction factor
$K$	identification number
$K_c$	critical identification number
$L_x$	length of the control volume located in the mixing channel
$L_y$	length of the control volume located in the inlet channels
$P$	pressure
$P_{in}$	measured pressure at the inlets of the control volume
$P_{out}$	measured pressure at the outlet of the control volume
$R^2$	absolute fraction of variance
$Re$	Reynolds number in the mixing channel based on the hydraulic diameter of the mixing channel

$Re_{in}$	Reynolds number in the inlet channels based on the hydraulic diameter of the inlet channels, $D_{h\_in}$
$t$	time
$U$	local flow velocity
$\mathbf{V}$	velocity vector

## Greek letters

$\mu$	viscosity
$\rho$	density
$\tau$	shear stress
$\zeta$	fourth parameter of the identification number $K$ in equation (4)

## 1. Introduction

The rapid progress in the manufacture and utilization of microstructure systems during the last decade has not been matched by corresponding advances in the understanding of the unconventional physics involved in the production and operation of microstructure devices. Providing such understanding is crucial for the design, optimization, manufacture and utilization of improved microdevices.

Despite the fundamental simplicity of the laminar flow in straight ducts, experimental studies of the microscale flow

<sup>1</sup> Author to whom any correspondence should be addressed.

have often failed to reveal the expected relationship between the friction factor and the Reynolds number. Microscale measurements of the friction factor by Mala and Li (1999) and Qu *et al* (2000) revealed higher values for the friction factor than theoretical macroscale predictions, whereas the works of Pfahler *et al* (1990) and Yu *et al* (1995) are among studies finding a decrease in the friction factor on the microscale. Liu and Garimella (2004) carried out experiments and measured friction factor in rectangular microchannels. They did not observe any scale-related phenomena in their experiments and concluded that the conventional theory can be used to predict the flow behavior in microchannels in the range of dimensions considered.

Wu and Cheng (2003) conducted experiments and measured the friction factor of the laminar flow of water in smooth silicon microchannels of trapezoidal cross-section. Bahrami *et al* (2007) proposed an analytical model to predict the pressure drop of fully developed, laminar flow of liquids in microchannels of arbitrary cross-section within 8% accuracy.

The purpose of this work was to study the pressure drop of the liquid phase inside micro T-mixers by means of computational fluid dynamics which has been proven to be an effective tool to design and develop microprocesses with minimum expenditure of time and money. The T-micro mixer is widely used because it is a continuous mixer with a very simple geometry. The mixing efficiency of the T-micro mixer has been studied intensively over the last years. However, less focus was on the pressure drop measurement inside the T-micro mixers. Here the aim was to determine a correlation between the friction factor, Reynolds number and the geometrical parameters of T-mixers. To end this, the effects on the pressure drop of variation in operating and design parameters such as volume flow rate, the aspect ratio of the mixing channel or the hydraulic diameters of the channels were studied. Recent work on liquid mixing with micro T-mixers carried out by Engler *et al* (2004) and Bothe *et al* (2006) highlighted three laminar flow regimes in the mixing channel namely, stratified flow, vortex flow and engulfment flow. At very low Reynolds numbers where the flow is in the stratified regime, the streamlines are parallel and the flow is plane-symmetric with respect to one symmetry plane of the mixer. The mixing is entirely due to molecular diffusion between the layers of different concentrations. Owing to the small diffusion coefficient of liquids, the resulting species distribution consists of two segregated regions. With increasing flow velocity when the fluid flows through the bends, centrifugal forces push the fluid from the center of the channel to the outer side. The fluid at the outer wall is pressed either upward or downward inducing a double symmetrical vortex pairs at the entrance of the mixing channel (Kockmann *et al* 2006, Hussong *et al* 2009). An increase in the mixing efficiency sets in. The main mixing principle, however, is still diffusion. The axis-symmetry of the vortex pairs at the entrance of the mixing channel is broken in the engulfment flow regime and fluid swaps to the opposite side. This asymmetrical flow increases the interfacial area of the mass transfer and dramatically improvement in the mixing is achieved. The onset of the engulfment regime in the T-micro

mixers depends not only on the Reynolds numbers, but also on another dimensionless group accounting for the geometrical parameters. Soleymani *et al* (2008) proposed a dimensionless group for the differentiation of the different flow regimes in liquid phase in T-micro mixers. They determined the critical value for the identification number at which the transition from the vortex flow to the engulfment flow regime occurs. For the simulations in this study, the flow will be flowing either in the vortex or in the engulfment regimes.

## 2. Simulation method

A computational fluid dynamics (CFD) simulation was carried out with the commercial code FLUENT 6.3.26 (ANSYS Inc.). The model used considers laminar mixing of the species in a micro T-mixer resulting from contact between two identical fluids having the same viscosity ( $\mu = 0.001$  Pa s) and the same density ( $\rho = 998.2$  kg m<sup>-3</sup>).

The density and viscosity of the flow were assumed to be constant along the channels, despite the very large pressure gradients that characterize the microscale flow. This assumption can be considered valid due to the fact that the effects of the internal heating as a result of the viscous dissipation are much less significant in liquid flows, owing to the much higher heat capacity of liquids relative to gases. The changes in mass and momentum are described by

$$\frac{\partial V_j}{\partial x_j} = 0, \quad (1)$$

$$\frac{\partial}{\partial t}(\rho V_i) + \frac{\partial}{\partial x_j} \rho V_j V_i = -\frac{\partial P}{\partial x_i} + \frac{\partial}{\partial x_j} \left( \mu \frac{\partial V_i}{\partial x_j} \right) \quad (2)$$

$i = 1, 2, 3$

where  $V$  and  $P$  are the velocity and pressure, respectively.

The field of velocity in three-dimensional T-mixers as schematically illustrated in figure 1 was sought through discretization of the conservation equations (1) and (2) using the finite volume formulation (Patankar 1980). A uniform velocity profile was assumed at the inlets and the pressure at the exit was assumed to be fixed to the local atmospheric pressure. A no-slip boundary condition at the sidewalls was applied (Gad-el-Hak 2002). The SIMPLE-Consistent algorithm (Vandoomaal and Raithby 1984) was implemented for pressure-velocity coupling. To achieve realistic simulations, the lengths of the side branches were chosen to be sufficiently long ranging from 3000–4000  $\mu\text{m}$  not to influence significantly the simulation of the fluid behavior inside the mixer channel. Initially, the simulations were performed with body-fitted structured grids of length 10  $\mu\text{m}$  in all directions. The grids were then locally refined in the area where the gradient of velocity was high. 10% of the maximum gradient of velocity was used as the basis for mesh refinement. The effects of the mesh size were tested by comparing a plot of the velocity versus location along the center line of the mixing channel. Refinement of the grids was continued until a solution independent of the mesh was achieved. A single simulation, as described above, takes about 4 h of CPU time on a single Pentium Xeon (2.4 GHz with 2GB of RAM).

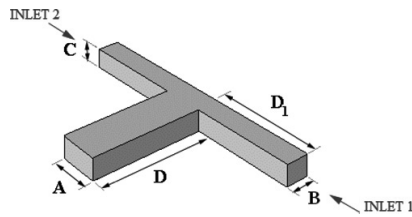


Figure 1. Schematic representation of a T-mixer with dimensions  $A \times B \times C$ .

Table 1. Ranges of the geometrical parameters of the micro T-mixers used in the numerical simulations

Width of the mixing channel, A	60–1600 $\mu\text{m}$
Width of the inlet channels, B	50–500 $\mu\text{m}$
Depth of the all channels, C	50–450 $\mu\text{m}$
Hydraulic diameter of the mixing channel, $D_h$	60–533 $\mu\text{m}$
Hydraulic diameter of the inlet channels, $D_{h,in}$	40–356 $\mu\text{m}$
Aspect ratio of the inlet channels, B/C	1–2
Aspect ratio of the mixing channel, A/C	0.66–5.4

To obtain a correlation between the friction factor, the Reynolds number and the geometrical parameters of the micro T-mixer, a set of numerical-type simulations were performed for 40 different mixers at different volume flow rates. The ranges of the geometrical parameters considered in the set of simulations are listed in table 1. The dimensions of the mixers were selected in such a way as to cover a wide range of aspect ratios of the inlet and mixing channels, namely, B/C and A/C. A, B and C are the width of the mixing channel, the width of the inlet channels and the depth of the channels, respectively.

### 3. Control volume

Figure 2 illustrates the streamlines at the entrance of the mixing channel for a  $600 \times 300 \times 300$  mixer (notation: width of the mixing channel in  $\mu\text{m} \times$  width of the inlet channels in  $\mu\text{m} \times$  depth of all channels in  $\mu\text{m}$ , see figure 1) at  $Re = 240$ . As can be seen, the straight streamlines breaks up when the fluid passes through the sharp edges of the micro T-mixer. This is due to the centrifugal forces which push the fluid from the center of the channel to the outer side. The fluid at the outer wall is pressed either upward or downward inducing a double vortex pair at the entrance of the mixing channel (Kockmann et al 2006, Hussong et al 2009). As the flow is in the laminar regime, the viscous forces dampen the vortices and the streamlines are readjusted after a certain distance depending on the mass flow rate and the dimensions of the micro T-mixer.

Owing to the very small molecular diffusion coefficients of liquids, the mixing in micro T-mixers at moderate Reynolds numbers is mainly due to the convective mass transfer induced by the vortices at the sharp edges of the mixers. In the remainder of this paper, the mixing zone is defined as the volume in the mixing channel in which the fluid streams are deflected.

Figure 3 shows the variation in the cross-sectional pressure along the mixing channel length at moderate

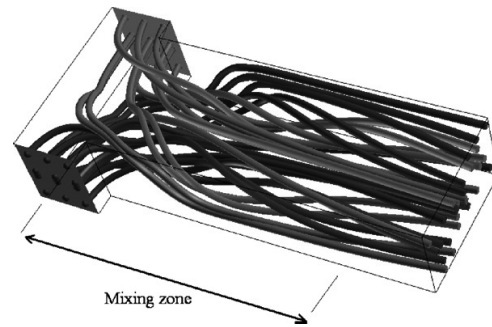


Figure 2. Streamlines at the entrance of the mixing channel for a  $600 \times 300 \times 300$  mixer at  $Re = 240$ . Color is used to distinguish between the streams entering each of the inlet channels. Outside the mixing zone the streamlines are scarcely bent.

Reynolds numbers for a  $600 \times 300 \times 300$  mixer. The values of the pressure are sharply decreased at the entrance of the mixing channel due to the deflection of the inflowing streams.

A linear pressure dependence is observed after the mixing zone, as expected for a fully developed duct flow. Figure 3 shows that by increasing the Reynolds number the mixing zone becomes larger and the pressure drop increases significantly.

In the light of the above discussion, special care has to be taken in choosing the control volume. As the key concern in this study is the pressure drop resulting from the deflection of the inflowing streams, the control volume was set to be the part of the mixer in which the streamlines of the fluid deflected from the fully developed flow as a result of the junction. The dimensions of the control volume vary by both mass flow rate and the geometry of the T-mixer.

The schematic of the control volume for the calculation of the pressure drop in a micro T-mixer is shown in figure 4.  $L_y$  is defined as the length of the inlet channels in which the flow is deflected by the T-mixer.  $L_x$  is defined as the length of the mixing channel in which the streamlines are strongly bent and the laminar flow has not readjusted.  $L_x$  is calculated as the distance away from the junction in the mixing channel where the longitudinal component of the velocity is 99% of the fully developed velocity magnitude. Similarly,  $L_y$  is calculated as the distance away from the junction in the inlet channels where the longitudinal component of the velocity is 99% of the fully developed velocity magnitude. In all the simulations, the inlet channels were chosen to be sufficiently long so that the fully developed flow can be observed in the upstream of  $L_y$ .

### 4. Simulation results

#### 4.1. Mixing zone

Analyzing the set of data obtained from numerical calculations by means of the differential evolution algorithm (Price et al 2005, Storn 1999, Storn and Price 1995) resulted in the following expression for  $L_x$ , defined as the length of the

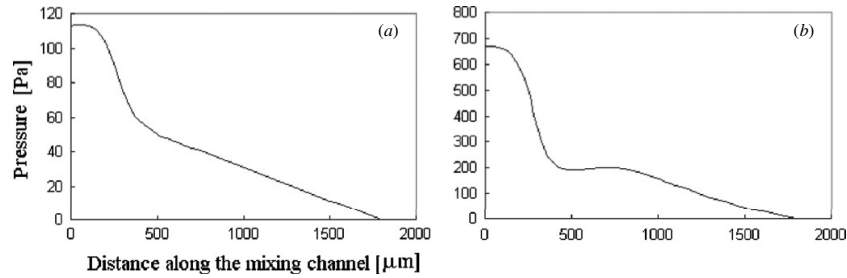


**Figure 3.** Cross-sectional pressure along the mixing channel for a  $600 \times 300 \times 300$  mixer at (a)  $Re = 80$ , and (b)  $Re = 240$ . The pressure plotted from the beginning of length  $L_x$  as shown in figure 4.

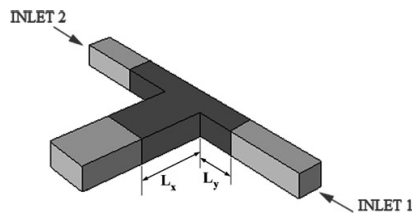


**Figure 4.** Mixing zone (the dark area) in a T-mixer. The mixing zone is set to be the control volume for the calculation of the pressure drop and friction factor.

mixing zone (control volume) located in the mixing channel:

$$\frac{L_x}{D_h} = \begin{cases} (0.0576 + 0.00156Re)(1 - 0.1635Dr + 4.2433Dr^2) & \text{if } K < 100 \\ (-2.389 + 0.0348Re)(1 - 1.458Dr + 1.0856Dr^2) & \text{if } K \geq 100 \end{cases} \quad (3)$$

where  $Re$  is the Reynolds number in the mixing channel based on the hydraulic diameter of the mixing channel,  $D_h$ ,  $Dr$  is the ratio between the hydraulic diameter of the mixing channel and the hydraulic diameter of the inlet channels,  $D_h/D_{h,in}$  and  $K$  is the identification number describing the flow regime inside a micro T-mixer, defined as

$$K = Re^{0.82} \left(\frac{B}{C}\right)^{-0.79} \left(\frac{D_{h,in}}{D_h}\right)^{-1.5} \left(\frac{A}{C}\right)^{0.15} \quad (4)$$

It has been shown that at the critical value of  $K_C = 100$  a transition from vortex flow to the engulfment flow regime can be observed (Soleymani *et al* 2008). Above the critical value of  $K_C = 100$ , the flow is in the engulfment regime.

Equation (3) implies that at moderate Reynolds number range where the flow is either in the vortex or the engulfment regimes, the dimensionless entrance length in the mixing channel,  $L_x/D_h$ , depends not only on the volume flow rate and the dimensions of the mixing channel but also on the geometrical parameters upstream of the flow in the inlet channels. This dependence appears in the second parenthesis in the right-side of equation (3).

For a micro T-mixer,  $L_x/D_h$  increases linearly with the Reynolds number in the mixing channel. From equation (3), it can also be concluded that for two T-mixers with the same  $Dr$ , the dimensionless length  $L_x/D_h$  is the same provided the Reynolds number is the same for both mixers.

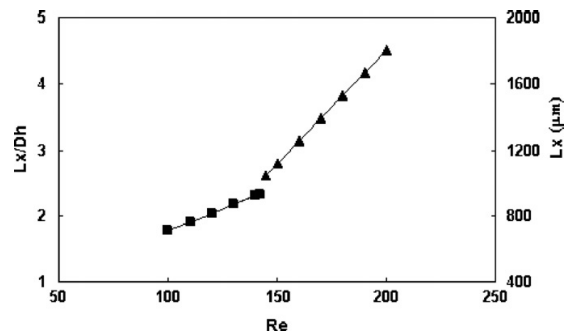


**Figure 5.**  $L_x/D_h$  as a function of the Reynolds number in the mixing channel for a  $600 \times 300 \times 300$  mixer, where  $D_h = 400 \mu\text{m}$ ,  $D_{h,in} = 300 \mu\text{m}$  and  $Dr = 1.33$ . The squares and triangles denote the vortex ( $K < 100$ ) and the engulfment ( $K > 100$ ) flow regimes, respectively.

Figure 5 shows the variation of  $L_x$  as a function of the Reynolds number in the mixing channel for a  $600 \times 300 \times 300$  mixer. At  $Re_C = 143$  where there is a transition from the vortex flow to the engulfment flow regime ( $K = 100$  in equation (4)), the slope of line  $L_x/D_h$  increases abruptly.

Analyzing the set of data obtained from the numerical calculations resulted in the following expression for  $L_y$ , defined as the length of the mixing zone (control volume) located in the inlet channels

$$\frac{L_y}{D_{h,in}} = \begin{cases} (0.6342 + 0.0038Re_{in})(-0.3531Dr_{in}^{-1} + 1 + 0.131Dr_{in}) & \text{if } K < 100 \\ (9.1852 + 0.01334Re_{in})(-0.5744Dr_{in}^{-1} + 1 - 0.3521Dr_{in}) & \text{if } K \geq 100 \end{cases} \quad (5)$$

where  $Re_{in}$  is the Reynolds number in the inlet channels based on the hydraulic diameter of the inlet channels,  $D_{h,in}$ . Here  $Dr_{in}$  is defined as

$$Dr_{in} = D_{h,in}/D_{h-A/2} \quad (6)$$

where  $D_{h-A/2}$  is the hydraulic diameter of a rectangular surface of dimensions  $\frac{A}{2} \times C$  (half of the width of the mixing channel  $\times$  the depth of the channels).

Equation (5) implies that the dimensionless length  $L_y/D_{h,in}$  increases linearly with  $Re_{in}$ . The length  $L_y$  as a function of the Reynolds number in the mixing channel for a  $600 \times 300 \times 300$  mixer is shown in figure 6. The slope of

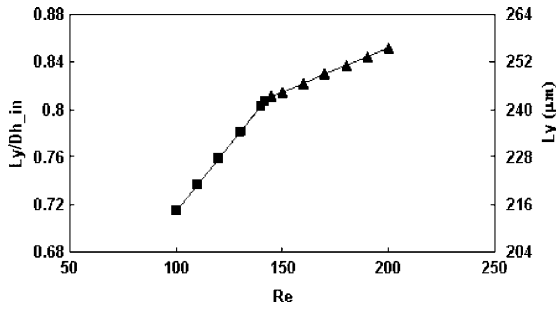


**Figure 6.**  $L_y$  as a function of the Reynolds number in the mixing channel for a  $600 \times 300 \times 300$  mixer, where  $Dr_{in} = 1$  and  $Re_{in} = 0.75 Re$ . The squares and triangles denote the vortex ( $K < 100$ ) and the engulfment ( $K > 100$ ) flow regimes, respectively.

the line decreases in the onset of the engulfment flow regime. Moreover, it can be seen that the length  $L_y$  is less sensitive to the variation of the Reynolds numbers (figure 6) than  $L_x$  (figure 5).

The proposed correlations for the calculation of the control volume dimensions ( $L_x$  and  $L_y$ ) can be replaced by the rule of thumb suggested by Engler *et al* (2004). In their investigation,  $L_x$  was set to be three times the mixing channel width (A) and  $L_y$  was roughly equal to the inlet channel width (B). According to Engler *et al* (2004),  $L_x = 1800 \mu\text{m}$  and  $L_y = 300 \mu\text{m}$  for a  $600 \times 300 \times 300$  mixer, while the calculated  $L_x$  and  $L_y$  from the proposed models (equations (3) and (5)) for the same mixer are functions of the volume flow rate and vary from 700–1800  $\mu\text{m}$  for  $L_x$ , and 240–255  $\mu\text{m}$  for  $L_y$  in the range of the Reynolds numbers shown in figures 5 and 6.

#### 4.2. Friction factor

After determination of the control volume for the specified mixer at a certain volume flow rate, characteristic length  $L$  and pressure loss  $\Delta P$  were measured. Characteristic length  $L$  is defined as the ratio of the control volume to the cross-sectional area of the mixing channel.

The pressure loss  $\Delta P$  inside the control volume is defined as the pressure drop resulting from deflection of the streamlines and is calculated as follows:

$$\Delta P = \left[ \frac{1}{2}(P_{in,1} + P_{in,2}) - P_{out} \right] - \left[ \frac{1}{2}(\Delta P_{s,1} + \Delta P_{s,2}) + \Delta P_s \right] \quad (7)$$

where  $P_{in,1}$  and  $P_{in,2}$  are the measured pressure at the inlets of the control volume, and  $P_{out}$  is the measured pressure at the outlet of the control volume.  $\Delta P_{s,1}$  and  $\Delta P_{s,2}$  are the pressure loss inside the inlet channels of the control volume if they were parts of a very long straight channel with the same cross-section as the inlet channels.  $\Delta P_s$  is the pressure drop inside the mixing channel of the control volume assuming long length and the total flow rate of the two inlet channels.

The first bracket in the right-hand side of equation (7) presents the total pressure loss inside the control volume.

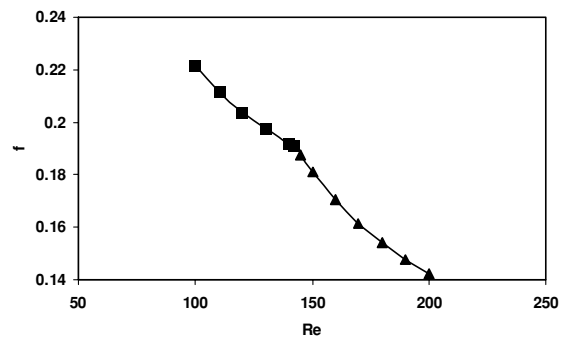


**Figure 7.** The variation of the friction factor versus the Reynolds number for a  $600 \times 300 \times 300$  mixer. The squares and triangles denote the vortex ( $K < 100$ ) and the engulfment ( $K > 100$ ) flow regimes, respectively.

The friction factor,  $f$ , can be related to the pressure drop  $\Delta P$  by

$$f = \frac{\left(\frac{\Delta P}{L}\right) D_h}{\rho U^2}, \quad (8)$$

where  $U$  is the mean velocity in the mixing channel.

Analysis of the simulation data resulted in the following expression for the friction factor  $f$  in terms of the Reynolds number in the mixing channel ( $Re$ ) and the ratio between the hydraulic diameter of the mixing channel and inlet channels ( $Dr$ ).

$$f(Re, Dr) = \begin{cases} (0.0115 Dr - 0.0152) Re + (44.86 Dr - 47.66) Re^{-1} & \text{if } K < 100 \\ + (-2.89 Dr + 3.92) & \\ (-73.15 Dr^2 - 2200 Dr + 5362) Re^{-2.03} & \\ + (0.0129 Dr + 0.0761) & \text{if } K \geq 100. \end{cases} \quad (9)$$

For the ranges of the Reynolds number and mixer dimensions considered in this study, the friction factor ranged from 0.16 to 1.25. The variation of the friction factor versus the Reynolds number in the mixing channel for a  $600 \times 300 \times 300$  mixer is shown in figure 7. It can be seen that the friction factor decreases with increasing Reynolds number. The slope of the line decreases at the onset of the engulfment flow regime.

## 5. Experimental investigations

To validate the simulation results, a series of experiments was conducted to measure the pressure loss with increasing mass flow for different micro T-mixers. Two micro T-mixers with the same hydraulic diameters were studied. Their detailed dimensions are presented in figure 8. The micro T-mixers were manufactured by micromachining using PTFE (polytetrafluoroethylene) as the main construction material. The mixers were fabricated by *high-speed milling* (HSM).

A schematic drawing of the experimental set-up is presented in figure 9. The liquid was delivered out of the container without pulsation. A precision valve was used to

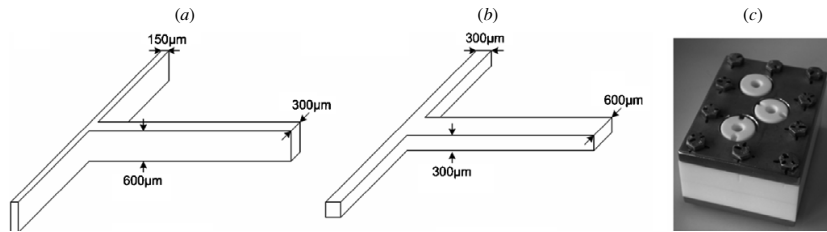


**Figure 8.** Geometric data of the micro T-mixers used in the experimental study; (a) T-mixer (1) of dimensions 300 × 150 × 600; (b) T-mixer (2) of dimensions 600 × 300 × 300; (c) housing of T-mixers.

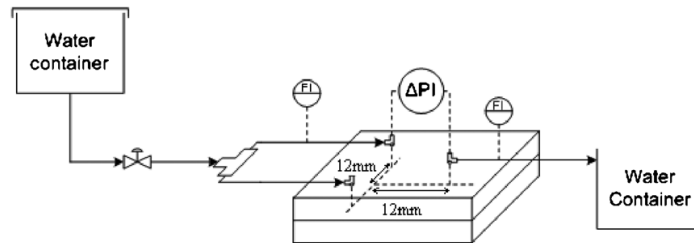


**Figure 9.** Schematic drawing of the experimental set-up.

**Table 2.** The pressure drop over the T-mixers obtained from the experiments and the proposed models (equations (4), (8) and (9)).

Mixer chip (A × B × C)	Mass flow in the mixing channel, $\dot{m}$ (g h <sup>-1</sup> )	Re in the mixing channel	$\Delta P$ , from experiment (Pa)	$\Delta P$ , equations (3–9) (Pa)	Error%
300 × 150 × 600	39	24	16	15	+6.7%
300 × 150 × 600	52	32	20	19	+5.3%
300 × 150 × 600	117	72	37	39	-5.1%
300 × 150 × 600	136	84	61	64	-4.7%
600 × 300 × 300	194	120	162	152	+6.6%
600 × 300 × 300	233	144	201	211	-4.7%
600 × 300 × 300	130	80	69	74	-6.7%
600 × 300 × 300	259	160	311	287	+8.3%
600 × 300 × 300	324	200	542	517	+4.8%
600 × 300 × 300	350	216	610	628	-2.9%

control the mass flow rate of the liquid entry into the micro T-mixer. The flow was divided into two streams by a T-connector and the streams were fed into the mixer inlets. Flow meters with a range of 0–20 ml min<sup>-1</sup> were used to measure the flow at one inlet and outlet streams to ensure that the flow was equally divided before entering the inlets of micro T-mixer. PTFE tubing of 1.0 mm inner diameter was used as the connector throughout the system. The pressure drop over the micro T-mixer was measured by a differential pressure transmitter with the range of 0 . . . 0.1 bar and ±0.5% full-scale accuracy. Additional small T-connectors orthogonal to the inlet channels and outlet channel were etched into the housing. Pressure drop was measured from these connectors at one inlet channel and mixing channel while another inlet connector was blocked so that these connectors have no influence on the fluid behavior in the T-mixer.

The liquid used in the experiments was de-ionized water tempered at 20 °C. The total flow rate was in the range between 0.72 ml min<sup>-1</sup> and 6.71 ml min<sup>-1</sup>. This range corresponds to Reynolds numbers in the mixing chambers between 24

and 249. The differential pressure transmitter measured the pressure difference at the distance of 12 mm away from the junction at the inlet and mixing channels of the mixer.  $\Delta P$ , defined as the pressure drop resulting from deflection of the streamlines inside the control volume, is calculated by subtracting  $\Delta P_{s,1+}$  from the pressure difference measured by the pressure transmitter.  $\Delta P_{s,1}$  and  $\Delta P_s$ , defined in section 4.2, are calculated by the proposed model of Bahrami *et al* (2007). Bahrami *et al* proposed an analytical model to predict the pressure drop of fully developed, laminar flow of liquids in microchannels of arbitrary cross-section within 8% accuracy.

Experimental results for the pressure loss  $\Delta P$  are compared with those obtained from the proposed models (equations (3–9)) in table 2. The model results for the pressure loss are consistent with the observations from the experiments in a wide range of Reynolds numbers. From table 2, it can be concluded that the proposed model can accurately estimate the pressure drop inside the micro T-mixers over a wide range of dimensions of the mixer and Reynolds number.

## 6. Conclusions

The pressure drops of liquids in micro T-mixers were investigated numerically. The study was motivated by the fact that this particular geometry (T-mixer) is very common in microfluidic applications. Application of the differential evolution algorithm to the set of data obtained from the simulation resulted in a model for the friction factor in T-mixers in the moderate and high Reynolds number range. In addition, models were proposed to estimate the mixing zone as a function of the volume flow rate and the mixer dimensions. Two fitting functions were used for the vortex and engulfment flows to describe that the flow patterns change from one regime to another.

It was seen that for both vortex and engulfment flows, the dimensionless lengths  $L_x/D_h$  and  $L_y/D_{h,in}$  relate linearly to the Reynolds number in the mixing channel and inlet channels, respectively. For both flow regimes,  $L_x/D_h$  and  $L_y/D_{h,in}$  and, consequently, the mixing zone increase with increasing Reynolds number. For vortex flow,  $L_x/D_h$  and  $L_y/D_{h,in}$  increase with increasing  $Dr$  and  $Dr_{in}$ , respectively. The proposed correlations for the mixing zone can be replaced by the rule of thumb suggested by Engler et al (2004). In their investigation,  $L_x$  was set to be three times the mixing channel width ( $A$ ) and  $L_y$  was roughly equal to the inlet channel width ( $B$ ).

The friction factor ( $f$ ), defined based on the pressure loss resulting from bending of the streamlines in the T-mixer, was observed to be a function of the Reynolds number in the mixing channel and the ratio between the hydraulic diameter of the mixing channel and the hydraulic diameter of the inlet channels, namely  $Dr = D_h/D_{h,in}$ . A quadratic polynomial correlation was found between the Reynolds number in the mixing channel and the friction factor  $f$ . The coefficients of the polynomial are functions of the hydraulic diameters ratio,  $Dr$ . The friction factor increases with increasing Reynolds number. The model results for the pressure drop due to the deflection of the fluid streamlines were in excellent agreement with those from the experiments. Consequently, it can be concluded that the proposed equation can estimate the friction factor and pressure drop within a high degree of accuracy.

## References

- Bahrami M, Yovanovich M M and Culham R 2007 A novel solution for pressure drop in singly connected microchannels of arbitrary cross-section *Int. J. Heat Mass Transfer* **50** 2492–502
- Bothe D, Stemich C and Warnecke H 2006 Fluid mixing in a T-shaped micro-mixer *Chem. Eng. Sci.* **61** 2950–8
- Engler M, Kockmann N, Kiefer T and Woias P 2004 Numerical and experimental investigations on liquid mixing in static micromixers *Chem. Eng. J.* **101** 315–22
- Gad-el-Hak M 2002 *The MEMS Handbook* (Boca Raton, Florida: CRC Press)
- Hussong J, Lindken R, Pourquie M and Westerweel J 2009 Numerical study on the flow physics of a T-shaped micro mixer *IUTAM Symp. on Advances in Micro- and Nanofluidics, IUTAM Bookseries 15*, (Berlin: Springer Science) pp 191–205
- Kockmann N, Kiefer T, Engler M and Woias P 2006 Convective mixing and chemical reactions in microchannels with high flow rates *Sensors Actuators B* **117** 495–508
- Liu D and Garimella S 2004 Investigation of liquid flow in microchannels *J. Thermophys. Heat Transfer* **18** 65–72
- Mala G M and Li D 1999 Flow characteristics of water in microtubes *Int. J. Heat Fluid Flow* **20** 142–8
- Patankar S V 1980 *Numerical Heat Transfer and Fluid Flow* (New York: McGraw-Hill)
- Pfahler J N, Harley J, Bau H and Zemel J 1990 Liquid transport in micron and submicron channels *Sensors Actuators* **21-A23** 431–4
- Price K V, Storn R M and Lampinen J A 2005 *Differential Evolution: A Practical Approach to Global Optimization* (Berlin: Springer Verlag)
- Qu W, Mala G M and Li D 2000 Heat transfer for water flow in trapezoidal silicon microchannels *Int. J. Heat Mass Transfer* **43** 3925–36
- Soleymani A, Kolehmainen E and Turunen I 2008 Numerical and experimental investigations of liquid mixing in T-Type micromixers *Chem. Eng. J.* **135S** 219–28
- Soleymani A, Yousefi H and Turunen I 2008 Dimensionless number for identification of flow patterns inside a T-micromixer *Chem. Eng. Sci.* **63** 5291–7
- Storn R 1999 System design by constraint adaptation and differential evolution *IEEE Trans. Evol. Comput.* **3** 22–34
- Storn R and Price K V 1995 Differential evolution—a simple and efficient adaptive scheme for global optimization over continuous spaces *Technical Report TR-95-012*, ICSI
- Vandoormaal J P and Raithby G D 1984 Enhancements of the SIMPLE method for predicting incompressible fluid flows *Numer. Heat Transfer* **7** 147–63
- Wu H Y and Cheng P 2003 Friction factors in smooth trapezoidal silicon microchannels with different aspect ratios *Int. J. Heat Mass Transfer* **46** 2519–25
- Yu D, Warrington R, Barron R and Ameel T 1995 An experimental and theoretical investigation of fluid flow and heat transfer in microtubes *Proc. ASME/JSME Thermal Engineering Joint Conf. (Maui, Hi)* pp 523–30



## **Publication II**

Ratchananusorn, W., Semyonov, D., Gudarzi, D., Kolehmainen, E., Turunen, I. (2011)  
Hydrodynamics and mass transfer studies on a plate microreactor  
*Chemical Engineering and Processing: Process Intensification*, 50, 1186-1192.

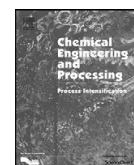
Reprinted by permission of Elsevier Publishing  
© Elsevier Publishing





Contents lists available at SciVerse ScienceDirect

## Chemical Engineering and Processing: Process Intensification

journal homepage: [www.elsevier.com/locate/cep](http://www.elsevier.com/locate/cep)

### Hydrodynamics and mass transfer studies on a plate microreactor

Warin Ratchananusorn\*, Denis Semyonov, Davood Gudarzi, Eero Kolehmainen, Ilkka Turunen

Department of Chemical Technology, Lappeenranta University of Technology, P.O. Box 20, FI-53851 Lappeenranta, Finland

#### ARTICLE INFO

##### Article history:

Received 21 April 2011  
Received in revised form 13 July 2011  
Accepted 19 August 2011  
Available online 26 August 2011

##### Keywords:

Microreactor  
Multiphase flow  
Gas holdup  
Interfacial area  
Mass transfer

#### ABSTRACT

Prototype of structured microreactor plates with 300  $\mu\text{m}$  deep flow channels was developed. Two plates with different structural elements, square and triangular, were used in the study. Flow behavior was investigated and the results showed excellent mixing behavior of gas and liquid phases. Hydrodynamic parameters and volumetric gas–liquid mass transfer coefficients were determined at various flow conditions. Gas holdup and the gas–liquid interfacial area were determined by an optical method using image processing software. Volumetric mass transfer coefficients were measured using nitrogen to strip oxygen from deionized water. The experimental results indicate a high mass transfer rate. Gas holdup and the total gas–liquid interfacial area were in the range of 20–45% and 2600–5600  $\text{m}^2 \text{m}^{-3}$ , respectively. Volumetric mass transfer coefficients were as high as  $1.1 \text{ s}^{-1}$ . An empirical correlation for the mass transfer coefficient was derived.

© 2011 Elsevier B.V. All rights reserved.

#### 1. Introduction

Microreactors have recently been of great interest for multiphase reaction applications, mainly because of their high heat and mass transfer capacities and perceived safety advantages [1,2]. Due to the small size of the flow channels, extremely high surface to volume ratios can be obtained, allowing excellent heat transfer properties. As a consequence, hotspots in exothermic reactions can be avoided because of the maintenance of uniform temperatures throughout the reactor [3]. In multiphase catalytic reactions, gas–liquid mass transfer sometimes represents significant resistance [4,5]. Microreactors can provide a high gas–liquid interfacial area and therefore enhance mass transfer by up to 100 times compared to conventional scale reactors [6,7]. Multiphase microreactors include both non-catalytic gas–liquid reactors and gas–liquid–solid reactors, where a catalyst may be fixed on the channel walls.

Typically, such reactors consist of a large number of parallel channels. The diameter of the channels can sometimes be even less than 100  $\mu\text{m}$ , thus the flow in microchannels is usually laminar and mainly dominated by viscosity, surface tension, and wall friction forces. Hydrodynamics of gas liquid flow in direct microchannels has been extensively studied [8–11]. The favorable flow pattern is slug (Taylor) flow, where elongated gas bubbles, occupying the whole cross section of the channel, alternate with liquid slugs. Only a thin liquid film then separates the gas slugs from the channel walls. As presented by Pohorecki [12], in some

conditions, this thin liquid film might be saturated by dissolved gas. In these cases, only the ends of the gas slugs provide an active interfacial area for mass transfer, which might decrease the mass transfer performance remarkably. However, if the walls are covered with catalyst, the gas may be consumed and no saturation would occur.

A number of studies have been conducted to investigate mass transfer characteristics associated with different flow patterns in different types of microscale gas–liquid contactors. Yue et al. [3,13] investigated the mass transfer characteristics of gas–liquid flow in rectangular microchannels with hydraulic diameter of 200, 400, and 667  $\mu\text{m}$ . The results exhibited that the specific gas–liquid interfacial area and mass transfer coefficient in microscale gas–liquid contactors were found to be at least one or two orders of magnitude higher than those in conventional scale gas–liquid contactors. Shao et al. [14] demonstrated the work on CFD modeling to investigate the mass transfer characteristics with slug flow pattern in micro-capillaries with diameter less than 1 mm. The results were compared and reported to be in the same range with the values from Yue et al. [3]. Losey et al. [6,7] designed and fabricated a novel type of multichannel packed-bed microreactors for hydrogenation reaction. The reactor consists of ten parallel channels with microstructure situated inside the channels. Extremely high mass transfer coefficient and gas–liquid interfacial area, by two orders of magnitude larger than in conventional scale gas–liquid contactors, were achieved in their study.

The current study was performed with novel microreactor plates designed for multiphase reactions. Gas holdup, the gas–liquid interfacial area, and the mass transfer coefficient were determined at various flow conditions.

\* Corresponding author.

E-mail address: [warin.ratchananusorn@lut.fi](mailto:warin.ratchananusorn@lut.fi) (W. Ratchananusorn).

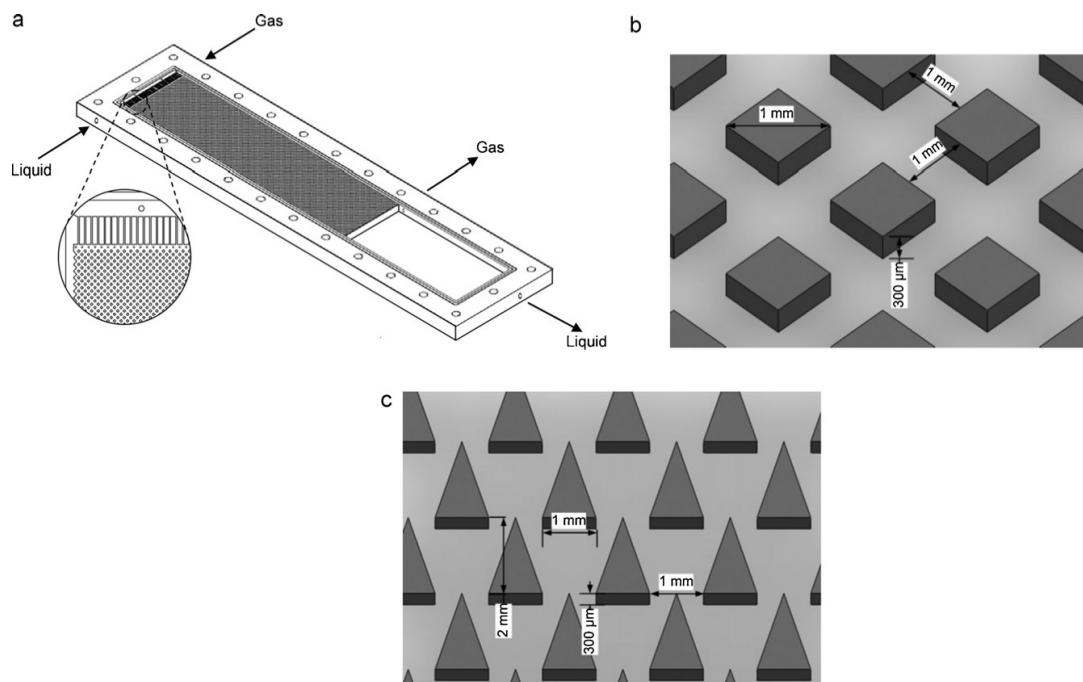


Fig. 1. Microreactor plate: (a) Microreactor plate showing inlet and outlet of gas and liquid. (b) Square structure layout and dimensions. (c) Triangular structure layout and dimensions.

## 2. Microreactor plate

A novel microreactor was constructed from parallel plates and the reaction space was located between them. This structure was selected in order to gain several advantages over more conventional multichannel structures. Firstly, plugging problems were expected to be less severe and more uniform fluid distribution was anticipated. Secondly, changing and regeneration of the catalyst were assumed to be less complex, because the plates can be easily separated from each other. An overview of the microreactor plate is shown in Fig. 1(a) and its detailed structure in Fig. 1(b) and (c).

The microreactor plate is made of stainless steel and consists of three sections: the inlet, reaction, and outlet section. Liquid and gas enter into the reactor at the inlet section from opposite sides and are divided into a number of substreams. The mixing and dispersion occurs in the reaction section, which consists of the structural elements. The size of the reaction section is  $10\text{ cm} \times 40\text{ cm}$ . Two types of structural elements, square and triangle, are used. The layout and dimensions of these structures is shown in Fig. 1(b) and (c). The structural elements are arranged in staggered arrays forming a number of parallel microchannels and providing a fraction of free space of 0.83 in the square structure configuration and 0.75 in the triangular structure configuration. The distance between the plates is  $300\text{ }\mu\text{m}$ . The reactor is vertically operated, allowing the fluids to flow downwards through the reaction section to the outlet section where the gas and liquid are separated by gravity. The liquid is then removed from the bottom and the gas is removed from the top of the outlet section.

## 3. Hydrodynamic measurement

The experimental setup is shown in Fig. 2. A water–air system was used. The reactor plate was covered by transparent acrylic plate

to enhance visual observation. A high speed camera was used to capture still images at different flow conditions in order to be able to determine hydrodynamic parameters.

Because the top and bottom plates are made of different materials, they have different wetting properties. The contact angle measurement was done with KSV CAM100 contact angle meter. The contact angle of water on steel was 72 and on the acrylic was 77. The difference in wetting properties might have small effect on the hydrodynamic behavior in the reactor.

The experiments were performed by feeding water at a certain flow rate ranging from 20 to  $100\text{ ml/min}$  into the reactor so that all the flow channels were fully occupied. Air was then fed into the reactor with a flow rate ranging between 36 and  $180\text{ ml}_n/\text{min}$ . The

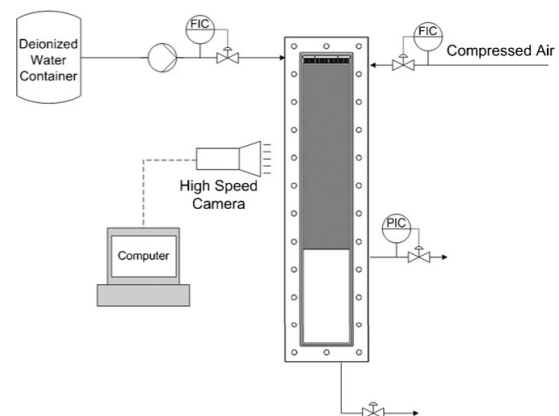
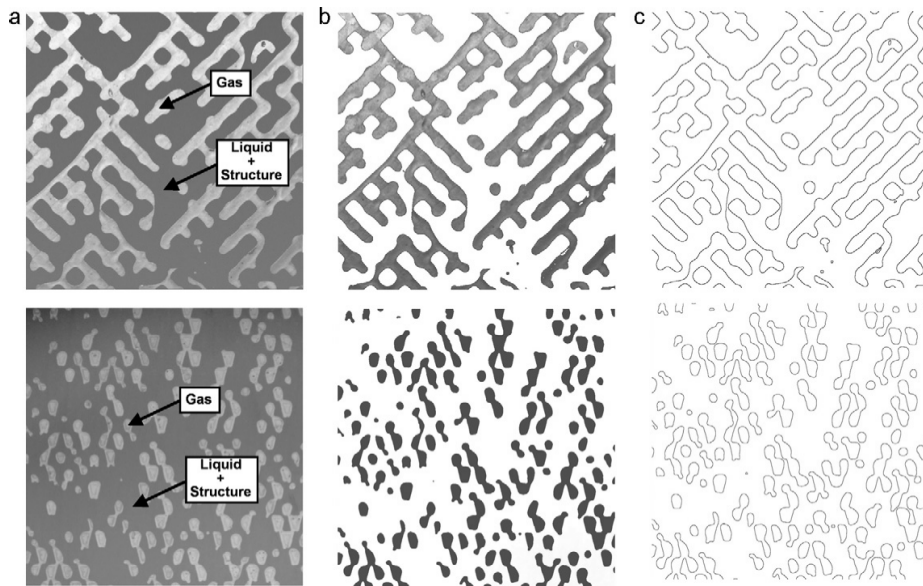


Fig. 2. Experimental setup for hydrodynamics measurement.



**Fig. 3.** Image processing steps for gas holdup and gas–liquid interfacial area measurements: (a) original image, (b) processed image showing the area of the gas slugs, (c) processed image showing the perimeters of the gas slugs.

feed flow rates correspond to a superficial velocity of 11–55 mm s<sup>-1</sup> and 20–100 mm s<sup>-1</sup> for water and air, respectively. Ambient temperature and pressure prevailed.

A favorable flow pattern was achieved. The flow in the microreactor demonstrated excellent mixing behavior by breaking and recombining the gas and liquid slugs throughout the reactor. Thus, an extremely high gas–liquid interfacial area was achieved.

From the investigation of flow behavior, the flow in microreactor plates was considerably unstable. The flow trajectories changed continuously due to the breaking–recombining behavior caused by the structural elements inside the reactors. The determination of hydrodynamic parameters by image analysis was done carefully in order to limit the uncertainty from the unstable flow and to prove the reproducibility of the results. Several sample images from each flow combination were taken at different time spans. The images were captured from the reaction section where the two phase flow was fully developed and the hydrodynamic parameters were determined as average values. The image processing software, ImageJ, was used to determine the hydrodynamic parameters. The images from square and triangular structure microreactor were cropped to 800 × 800 pixel and 1440 × 1440 pixel, respectively. The scales of the images were 43 pixel/mm for the square structure reactor and 30 pixel/mm for the triangular structure reactor. The

software calculated the area occupied by the gas by subtracting the area occupied by the liquid and the structural elements from the total plate area. The steps in image analysis for gas holdup and gas–liquid interfacial area measurements in the square structure microreactor (upper) and triangular structure microreactor (lower) are presented in Fig. 3. Brighter parts in Fig. 3(a) represent the gas phase, while darker parts represent the liquid phase and structural elements. Fig. 3(a) was processed by inverting the colors so that the gas phase has dark color in Fig. 3(b). The perimeter of the gas phase in Fig. 3(b) was generated and is shown in Fig. 3(c). The area of the gas slugs determine gas holdup which is presented in Fig. 4. Fig. 5 presents the gas–liquid interfacial area determined from (a) only the perimeter of gas slugs, denoted by the subscript *per*, and (b) both from the perimeter of gas slugs and the area against the bottom and cover plate, denoted by the subscript *tot*. The latter represents the real interfacial area. However, in some applications only the area *a<sub>per</sub>* might be active in mass transfer. The gas–liquid interfacial area was determined both as the area per volume of fluid, denoted by the subscript *f*, and per volume of the reactor, denoted by the subscript *r*.

Gas holdup determined from the experiments was in the range of 20–45%. The values of the total gas–liquid interfacial area were high up to 4800 and 5600 m<sup>2</sup> m<sup>-3</sup> for the square and triangular

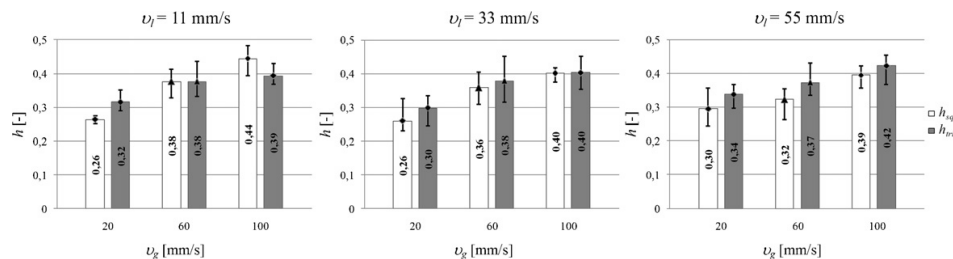


**Fig. 4.** Experimental results: gas holdup at various flow conditions.

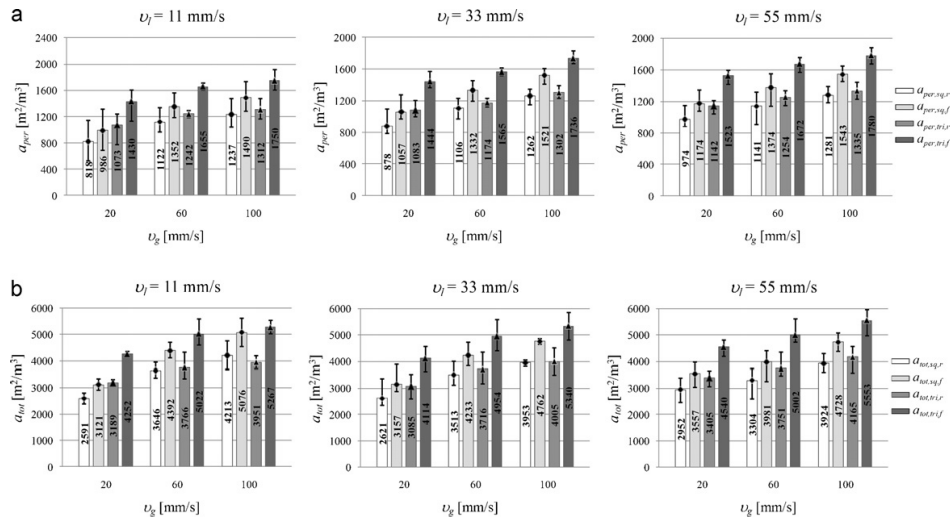


Fig. 5. Experimental results: gas–liquid interfacial area at various flow conditions: (a) determined from only the perimeter of gas slugs, (b) determined from the perimeter of gas slugs and area against the bottom and cover plate.

structure microreactor, respectively, which is much higher than in typical commercial gas–liquid reactors, where  $1000 \text{ m}^2 \text{ m}^{-3}$  is seldom exceeded. The uncertainty of the results obtained from the images at each flow combination was found to be in the range of  $\pm 20\%$  where the maximum value at  $\pm 30\%$  was found at the lowest gas and liquid flow rate in the square plate. The uncertainty tended to be decreased at higher gas and liquid flow rate. This can be explained by the poor hydrodynamic behavior which was exhibited as fingered flow (channeling flow). This type of flow was observed at low gas and liquid flow rate where the gas and liquid phases flowed through the certain part of the reactor plate and breaking–recombining behavior sometimes occurred during the investigation.

The gas and liquid slugs in the triangular plate were splitted into smaller gas bubbles and liquid slugs than the ones in the square plate; a result caused from the difference in the void fraction and in the shape of the structural elements. As a result, the gas–liquid interfacial area was slightly higher in the plate with triangular elements. The gas superficial velocity strongly influenced both gas holdup and the gas–liquid interfacial area, while the effect of the liquid superficial velocity was insignificant.

#### 4. Mass transfer measurements

The experimental setup is shown in Fig. 6. A water–nitrogen–oxygen system was used. Deionized water was saturated with oxygen, and nitrogen was used to strip oxygen out from the liquid phase. An in-line oxygen concentration analyzer was employed to measure the concentration of oxygen at the inlet and outlet of the reactor. The ranges of the gas and liquid flow rates were the same as in hydrodynamic measurements.

Oxygen was transferred from the liquid phase to the gas phase and nitrogen vice versa. Changes in the oxygen and nitrogen molar flow in the gas phase along the microreactor can be described as:

$$\frac{d\dot{n}_{O_2}}{dL} = -k_1 a (C_{O_2}^* - C_{O_2}) (1 - \varepsilon_s) A_{cr} \quad (1)$$

$$\frac{d\dot{n}_{N_2}}{dL} = -\frac{D_{N_2}}{D_{O_2}} k_1 a (C_{N_2}^* - C_{N_2}) (1 - \varepsilon_s) A_{cr} \quad (2)$$

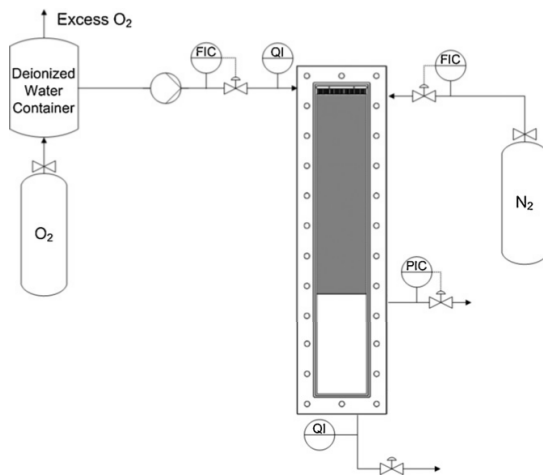


Fig. 6. Experimental setup for mass transfer study.

Concentrations of oxygen and nitrogen in the liquid phase change according to the following equations

$$\frac{dC_{O_2}}{dL} = k_1 a (C_{O_2}^* - C_{O_2}) \frac{A_{cr}(1 - \varepsilon_s)(1 - \varepsilon_g)}{\dot{V}_l} \quad (3)$$

$$\frac{dC_{N_2}}{dL} = \frac{D_{N_2}}{D_{O_2}} k_1 a (C_{N_2}^* - C_{N_2}) \frac{A_{cr}(1 - \varepsilon_s)(1 - \varepsilon_g)}{\dot{V}_l} \quad (4)$$

The saturation concentrations of the nitrogen and oxygen can be calculated by Henry's law as:

$$C_{N_2}^* = \frac{p_{N_2}}{H_{N_2}} \quad (5)$$

$$C_{O_2}^* = \frac{p_{O_2}}{H_{O_2}} \quad (6)$$

$$p_{N_2} = \frac{\dot{n}_{N_2}}{\dot{n}_{O_2} + \dot{n}_{N_2}} \cdot P \quad (7)$$

**Table 1**  
Parameter values and correlation for mass transfer coefficient.

Element type	$\alpha_1$	$\alpha_2$	$\alpha_3$	Correlation
Square (◆)	0.177	0.874	0.179	$k_1a = 0.177 \left(\frac{u_g}{0.02}\right)^{0.874} \left(\frac{u_l}{0.02}\right)^{0.179}$
Triangular (▲)	0.175	0.899	0.432	$k_1a = 0.175 \left(\frac{u_g}{0.02}\right)^{0.899} \left(\frac{u_l}{0.02}\right)^{0.432}$

$$p_{O_2} = \frac{\dot{n}_{O_2}}{\dot{n}_{O_2} + \dot{n}_{N_2}} \cdot P \quad (8)$$

where  $H_{N_2} = 1468.90 \text{ dm}^3 \text{ bar mol}^{-1}$  and  $H_{O_2} = 732.62 \text{ dm}^3 \text{ bar mol}^{-1}$  [15].

A closed system of four ordinary differential equations (ODE) describes the two-phase mass transfer in the microreactor.

The following correlation was used to describe the dependency of the mass transfer coefficient from the superficial velocities:

$$k_1a = \beta_1 u_g^{\beta_2} u_l^{\beta_3} \quad (9)$$

For better numerical performance the following normalized form of the equation was used:

$$k_1a = \alpha_1 \left(\frac{u_g}{u_{g,norm}}\right)^{\alpha_2} \left(\frac{u_l}{u_{l,norm}}\right)^{\alpha_3} \quad (10)$$

where  $u_{g,norm}$  and  $u_{l,norm}$  are equal to  $0.02 \text{ m s}^{-1}$ .

A set of experiments was performed on both the square and triangular structure microreactors. In each experiment  $O_2$  concentration in the liquid was measured at the inlet ( $L = 0 \text{ mm}$ ) and outlet of the microreactor ( $L = 400 \text{ mm}$ ) for each gas and liquid flow rate. Inlet measurements defined initial conditions for the ODE system and outlet measurements were used to fit the model parameters. An Euler method was then used to solve the ODE system. It was found that this method is very fast and robust enough in this case. Conducted error analysis revealed that it gives an accuracy of the estimated parameters of 0.2–0.5% when the number of subintervals is only 200.

$k_1a$  values were estimated by minimizing the sum of the squared differences between the estimated and the measured values at the outlet of the reactor. Corresponding estimated optimal parameter values are shown in Table 1.

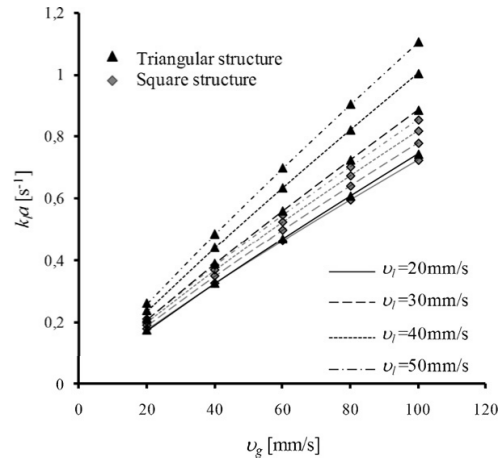


Fig. 7. Estimated  $k_1a$  dependency on  $u_g$  and  $u_l$ .

Fig. 7 shows that mass transfer in the triangular structure microreactor was better than in the square structure one. The maximum  $k_1a$  values in the triangular structure microreactor were as high as  $1.10 \text{ s}^{-1}$ , which was approximately 25% higher than in the square structure reactor, where the highest value was  $0.85 \text{ s}^{-1}$ . The comparison of mass transfer coefficient obtained from this study and from literature [3,6,7,13,14,16–19] in microscale and conventional scale gas–liquid contactors is presented in Table 2. The mass transfer coefficients from this study are in the range from 0.17 to  $1.10 \text{ s}^{-1}$ , which are one or two orders of magnitude higher than

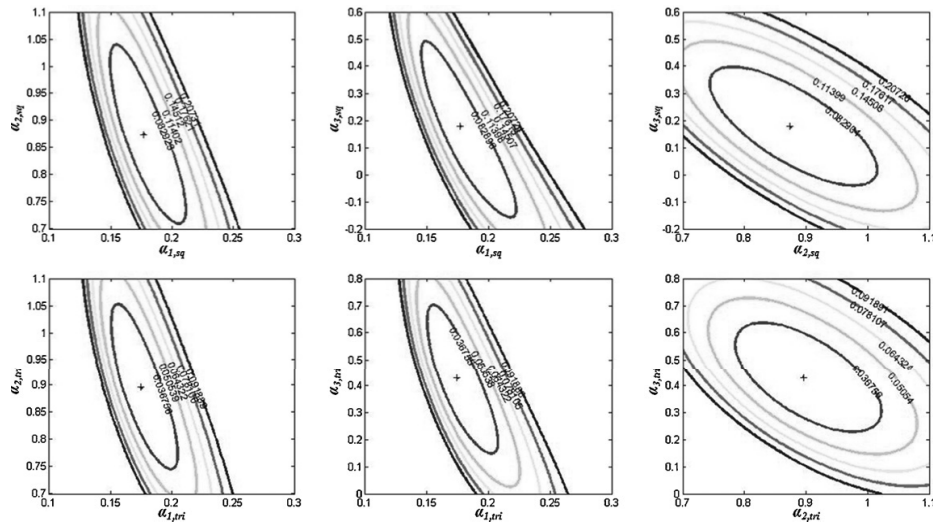


Fig. 8. Sensitivity plots of estimated parameters for volumetric mass transfer coefficient.

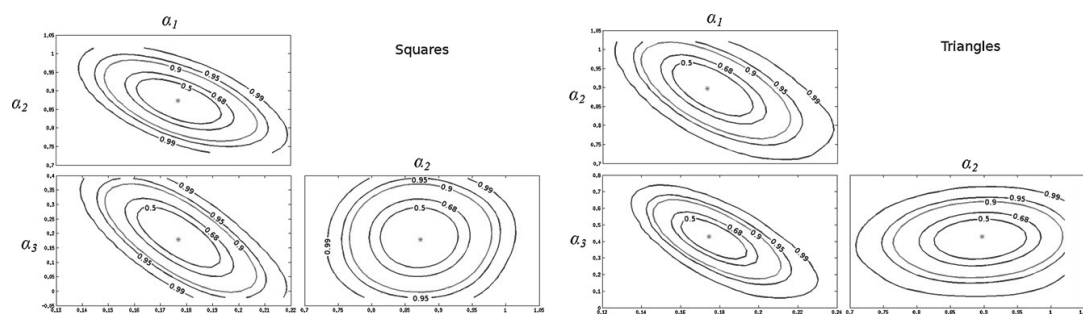


Fig. 9. Confidence level of marginal distribution of parameters.

Table 2

Comparison of gas–liquid interfacial area and mass transfer coefficients in different gas–liquid contactors.

Type of contactor	$a$ [ $\text{m}^2 \text{m}^{-3}$ ]	$k_L a$ [ $\text{s}^{-1}$ ]
Bubble column [16]	180–670	0.07–0.25
Trickle bed reactor [17]	150–1500	0.01–0.08
Three-phase fluidized bed [18]	30–160	0.08–0.64
Static mixer [19]	100–1000	0.1–2.4
Microchannel [3,13]	3400–9000	0.3–21
Micro-capillaries [14]	1000–7500	0.3–1.5
Micro packed-bed reactor [6,7]	1500–16,000	5–15
Microreactor in this study	2600–5600	0.17–1.1

conventional scale gas–liquid contactors and in the same range as in other microscale gas–liquid contactors.

Sensitivity analysis of the estimated parameters ( $\alpha_1$ ,  $\alpha_2$ , and  $\alpha_3$ ) was carried out to determine their identifiability and the goodness of the fit. The aim of the analysis was to determine the shape of the objective function representing the sum of squares  $SS(\alpha_1, \alpha_2, \alpha_3)$  used to find the parameters. Its minimum indicates the optimal point and the best parameter values. The shape of the function tells how well every parameter is identified and if there is a correlation between them. In this case the objective function is a surface in a four-dimensional space, so it cannot be explicitly plotted. Instead, two-dimensional cross-sections of this function at the optimal point can be studied to get an insight of it. The cross-section is done along coordinate planes ( $\alpha_1, \alpha_2$ ), ( $\alpha_1, \alpha_3$ ) and ( $\alpha_2, \alpha_3$ ). Corresponding contour-plots are presented in Fig. 8. Top row is for the square structure, bottom row – for triangle. These plots indicate that the parameters are well-identified, although a slight correlation exists between them, especially between the  $\alpha_1$ – $\alpha_2$  and  $\alpha_1$ – $\alpha_3$  in both cases.

Confidence levels of marginal distributions of the estimated parameters are presented in Fig. 9. Three plots on the left are for the squared structure reactor and three on the right are for the triangle. These distributions were estimated using Monte-Carlo Markov Chain (MCMC) simulation. They are in a good accordance with the objective function contour-plots and also indicate the same correlation between the  $\alpha_1$ – $\alpha_2$  and  $\alpha_1$ – $\alpha_3$  for both cases.

## 5. Conclusion

Hydrodynamic and mass transfer behavior of a novel plate type microreactor was studied. The reactor has certain advantages when compare to conventional microreactor consisted of parallel direct microchannels. Firstly, less plugging problem can be expected. Secondly, changing and regenerating catalyst is easier because the reactor can be easily opened.

Relatively uniform gas–liquid distribution without serious channeling was obtained. Hydrodynamics and mass transfer

performance of the microreactor were considerably better than in conventional multiphase chemical reactors. The total interfacial area was in the range of 2600–5600  $\text{m}^2 \text{m}^{-3}$  and the volumetric mass transfer coefficient was in the range of 0.17–1.10  $\text{s}^{-1}$ . The volumetric mass transfer coefficient correlated well with the superficial velocities of the gas and liquid. The parameters of the correlation were well determined.

It was found that the triangular structural elements gave slightly better hydrodynamic behavior than the square ones. As a consequence, also the mass transfer was faster with the triangular elements.

## Appendix A. Nomenclature

$a$	specific surface area ( $\text{m}^2 \text{m}^{-3}$ )
$A$	area ( $\text{m}^2$ )
$C$	concentration ( $\text{mol m}^{-3}$ )
$C^s$	saturation concentration ( $\text{mol m}^{-3}$ )
$D$	diffusivity ( $\text{m}^2 \text{s}^{-1}$ )
$h$	holdup (–)
$H$	Henry's constant ( $\text{dm}^3 \text{bar mol}^{-1}$ )
$k$	volumetric mass transfer coefficient ( $\text{m s}^{-1}$ )
$L$	length of the microreactor plate (m)
$p$	partial pressure (bar)
$P$	total pressure (bar)
$\dot{V}$	volumetric flow rate ( $\text{m}^3 \text{s}^{-1}$ )

### Greek symbols

$\varepsilon$	volume fraction (–)
$\nu$	superficial velocity ( $\text{mm s}^{-1}$ )

### Subscripts

$cr$	cross sectional
$f$	fluid
$g$	gas
$l$	liquid
$norm$	normalized
$per$	perimeter
$r$	reactor
$s$	structured plate reactor
$sq$	square structure plate
$tot$	total
$tri$	triangular structure plate

## References

- [1] W. Ehrfeld, V. Hessel, H. Löwe, Microreactors: New Technology for Modern Chemistry, Wiley-VCH, Weinheim, 2002.
- [2] K. Jähnisch, V. Hessel, H. Löwe, M. Baerns, Chemistry in microstructured reactors, Angew. Chem. Int. Ed. 43 (2004) 406–446.

- [3] J. Yue, G. Chen, Q. Yuan, L. Luo, Y. Gontier, Hydrodynamics and mass transfer characteristics in gas–liquid flow through a rectangular microchannel, *Chem. Eng. Sci.* 62 (2007) 2096–2108.
- [4] L. Kiwi-Minsker, A. Renken, Microstructured reactors for catalytic reactions, *Catal. Today* 110 (2005) 2–14.
- [5] St. Walter, St. Malmberg, B. Schmidt, M.A. Liauw, Mass transfer limitations in microchannel reactors, *Catal. Today* 110 (2005) 15–25.
- [6] M.W. Losey, M.A. Schmidt, K.F. Jensen, Microfabricated multiphase packed-bed reactor: characterization of mass transfer and reactions, *Ind. Eng. Chem. Res.* 40 (2001) 2555–2562.
- [7] M.W. Losey, J. Rebecca, S.L. Firebaugh, M.A. Schmidt, K.F. Jensen, Design and fabrication of microfluidic devices for multiphase mixing and reaction, *J. Microelectromech. Syst.* 11 (2002) 709–717.
- [8] J.W. Coleman, S. Garimella, Characterization of two-phase flow patterns in small diameter round and rectangular tubes, *Int. J. Heat Mass Transf.* 42 (1999) 2869–2881.
- [9] A. Kawahara, P.M.Y. Chung, M. Kawaji, Investigation of two-phase flow pattern, void fraction and pressure drop in a microchannel, *Int. J. Multiphase Flow* 28 (2002) 1411–1435.
- [10] S. Waelchli, P.R. von Rohr, Two-phase flow characteristics in gas–liquid microreactors, *Int. J. Multiphase Flow* 32 (2006) 791–806.
- [11] R. Pohorecki, P. Sobieszuk, K. Kula, W. Moniuk, M. Zieliński, P. Cygański, P. Gawiński, Hydrodynamic regimes of gas–liquid flow in a microreactor channel, *Chem. Eng. J.* 135S (2008) 185–190.
- [12] R. Pohorecki, Effectiveness of interfacial area for mass transfer in two-phase flow in microreactors, *Chem. Eng. Sci.* 62 (2007) 6495–6498.
- [13] J. Yue, L. Luo, Y. Gonthier, G. Chen, Q. Yuan, An experimental study of air–water Taylor flow and mass transfer inside square microchannels, *Chem. Eng. Sci.* 64 (2009) 3697–3708.
- [14] N. Shao, A. Gavriilidis, P. Angeli, Mass transfer during Taylor flow in microchannels with and without chemical reaction, *Chem. Eng. J.* 160 (2010) 873–881.
- [15] R.H. Perry, *Perry's Chemical Engineers' Handbook*, 7th edition, McGraw-Hill Inc., USA, 1999.
- [16] K.M. Singh, S.K. Majumder, Co- and counter-current mass transfer in bubble column, *Int. J. Heat Mass Transf.* 54 (2011) 2283–2293.
- [17] M.H. Aldahhan, F. Larachi, M.P. Dudukovic, A. Laurent, High-pressure trickle-bed reactors: a review, *Ind. Eng. Chem. Res.* 36 (8) (1997) 3292–3314.
- [18] W. Yang, J. Wang, T. Wang, Y. Jin, Experimental study on gas–liquid interfacial area and mass transfer coefficient in three-phase circulating fluidized beds, *Chem. Eng. J.* 84 (2001) 485–490.
- [19] A. Heyouni, M. Roustan, Z. Do-Quang, Hydrodynamics and mass transfer in gas–liquid flow through static mixers, *Chem. Eng. Sci.* 57 (2002) 3325–3333.



### **Publication III**

Semyonov, D., Ratchananusorn, W., Turunen, I. (2013).  
Hydrodynamic model of a microstructured plate reactor,  
*Computers and Chemical Engineering*, 52, 145-154.

Reprinted by permission of Elsevier Publishing  
© Elsevier Publishing





## Hydrodynamic model of a microstructured plate reactor

D. Semyonov\*, W. Ratchananusorn, I. Turunen

Lappeenranta University of Technology, Department of Chemical Technology, Finland

### ARTICLE INFO

#### Article history:

Received 18 May 2012

Received in revised form 2 November 2012

Accepted 10 December 2012

Available online 2 January 2013

#### Keywords:

Microreactor

CFD

Multiphase flow

Interfacial area

### ABSTRACT

A numerical model of a two-phase flow in a plate microreactor was developed. The model is based on a computational fluid dynamics (CFD) approach and was constructed with the help of an open-source toolbox OpenFOAM, which utilizes a finite volume method to solve the equations of a fluid motion. A cold flow, i.e. a flow without a reaction and a mass transfer was considered in this study. The model was validated by comparing with experimentally measured hydrodynamic parameters: gas holdup and the interfacial area of gas bubbles inside the existing prototype. Validated model was used to test several proposed plate structures for the next prototype. The structure with the highest gas–liquid interfacial area was chosen for the construction.

© 2013 Elsevier Ltd. All rights reserved.

### 1. Introduction

Two-phase gas–liquid flow inside a newly developed microstructured plate microreactor (Ratchananusorn, Semyonov, Gudarzi, Kolehmainen, & Turunen, 2011) was the subject for modelling in the present study. The microreactor consists of two plates. One plate has a numerous intersecting channels with 300  $\mu\text{m}$  depth (Fig. 1), or alternatively it can be considered as a chamber with many structural elements with 300  $\mu\text{m}$  height. These elements work as obstacles to mix the flow and to achieve high values of a gas–liquid interfacial area. The second plate is flat and firmly covers the chamber preventing any leakage over the top of the elements. Gas and liquid are fed into the chamber in the inlet section through a set of holes and channels in attempt to achieve a uniform flow distribution from the beginning of the reaction space. More detailed information about the microreactor has been given by Ratchananusorn et al. (2011).

This concept of numerous intersecting channels requires detailed investigation and optimization. Usage of a CFD approach here is justified by several reasons: CFD results give a comprehensive outlook on the flow inside the reactor and therefore gives a good insight into the phenomena occurring in the microreactor, e.g. heat and mass transfer. CFD simulations are also easier and cheaper than the experiments, so the optimal conditions for real runs can be chosen by simulation. The full-scale CFD model is convenient for shape optimization, because the construction of every new microreactor prototype takes much more time and

is much more expensive than creating a new geometry on a computer.

In literature there are number of reports on successful application of CFD for a full-scale modelling of different types of multiphase microreactors and micromixers (Al-Rawashdeha, Hessela, Loba, Mevissena, & Schonfelda, 2008; Chii-Dong et al., 2011; Deshmukh, Mhadeshwar, & Vlachos, 2004; Harries, Burns, Barrow, & Ramshaw, 2003; Qian & Lawal, 2006), but none of them can be extended to be applicable in this case. Obstacles cause the flow to split and merge continuously, yielding in a favourable chaotic flow pattern with high interfacial area. Because of chaotic and unsteady flow behaviour, approaches like described in Harries et al. (2003) or Kashid, Agar, and Turek (2007) cannot be used in this case, because here the slug properties vary in time and space. Therefore, to get statistically reliable results of such unsteady flow it is required to simulate the flow in a considerably big space span and then also to average over the time to eliminate the effect of randomness. This method should give stationary characteristic values of the hydrodynamic parameters, which are free of fluctuations due to the chaotic behaviour of the flow. Correct modelling of the chaotic unsteady flow pattern requires a very fine computational mesh to accurately resolve all small details resulting in that pattern. This causes particular difficulties, as the full-scale 3D simulation in this case becomes extremely heavy and can not be afforded.

A goal in the development of the model was to correctly resolve the interfacial area between the phases to use it for testing the prototypes. Interfacial area depends on shape and distribution of gas bubbles in the microreactor. The shape, size and hold-up of gas bubbles strongly depend on the ratios between inertia, viscosity and surface tension forces on a microlevel. Therefore, it is of primary importance to correctly resolve these forces in order to get the correct interfacial area values.

\* Corresponding author.

E-mail address: [denis.semyonov@lut.fi](mailto:denis.semyonov@lut.fi) (D. Semyonov).

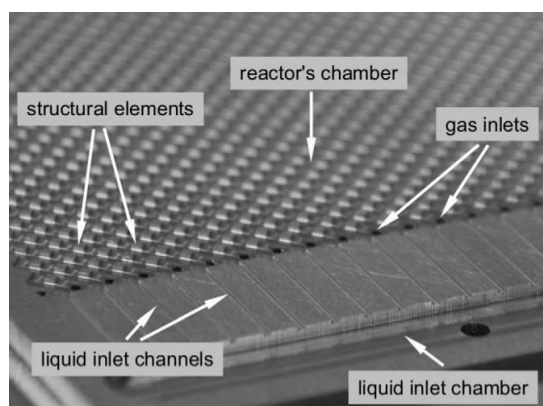


Fig. 1. Photo of an inlet section.

## 2. Experimental setup

Two prototypes were studied. First one is the original, which was used for the model validation. Second one was built based on the modelling results. In the first prototype, the plate has square structural elements, which form an orthogonal grid of intersecting channels, Fig. 2. <sup>1</sup> The dimensions of elements are 0.71 mm × 0.71 mm, the width of channels is 1 mm and the channels' depth is 300 μm. The fraction of these elements is 17.16%. Fig. 3 (left) shows a detailed image of the microstructure.

The plate consists of three parts: inlet, reaction zone, and outlet. Liquid and gas enter the reactor as a number of sub-streams in the inlet part. There are 41 inlet channels which are 150 μm deep and 500 μm wide and 42 gas inlet holes with 500 μm diameter (Fig. 1). Gas inlet holes are located shortly downstream after the liquid inlet channels – see Fig. 1 and the zoom-in circle in Fig. 2. The liquid gets into the inlets from the bigger cavity above, which is filled by two inlet holes connected to the pipeline from the pump. The pump type is annular gear pump (HNP Mikrosysteme GmbH) with the pumping speed of 0–288 ml/min. The gas gets into the inlets from a cylindrical cavity drilled in the plate behind the gas holes. This cavity is connected to the pipeline from the high pressure gas vessel with the flow controller. Both gas and liquid flows were continuous. Direction of the liquid inflow coincides with the direction of a mean flow in the reactor, and the direction of the gas inflow is orthogonal to the mean flow. The contact of the phases occurs in the reacting zone, which is 100 mm wide and 400 mm long. The reactor is vertically operated allowing to separate the fluids at the outlet section by gravity. To become fully developed the flow needs to pass 100–200 mm after the inlets.

After the model was built and tested for the square-structured microplate, it was used to test a number of alternative proposal structures, among which were squares, diamonds, rounds and triangles with different sizes and spacing. The best one was chosen on the basis of maximum interfacial area for building the next prototype. It has triangular structural elements with 1 mm base, 2 mm height and 2 mm horizontal and vertical spacing with checkerboard order – Fig. 3 (right). The fraction of elements in chosen structure was 25%. The second prototype for the hydrodynamical and mass transfer studies has 49 liquid and 50 gas inlets of the

same type as in the first one. The dimensions of the inlets are also the same.

Further these prototypes with different microplates will be referred to as 'first' and 'second' or 'square' and 'triangular'.

The experimental setup is shown in Fig. 4. <sup>2</sup> A water–air system at atmospheric pressure was used for hydrodynamic studies. Water was fed to the reactor with a range between 20 and 100 ml/min and gas flow rate ranging from 36 to 180 ml/min. Corresponding inlet velocities were in range 0.073–0.364 m/s for the gas and 0.11–0.56 m/s for the liquid. A high shutter speed camera was used to record the flow and to capture still images, from where the hydrodynamic parameters were estimated. The camera has resolution of 10.2 megapixels. The shutter speed was varied between from 1/2000 to 1/4000 s and ISO speed was varied between 100 and 400. The experiments were done continuously using constant flow rates of both fluids. Still images were captured at different flow conditions.

## 3. Model description

The model is based on the Navier–Stokes system of equations for incompressible fluid. Incompressibility assumption can be used because the pressure drop in the reactor is small enough, so the bubbles' volumes do not change significantly, and also the maximal velocity is of order of several m/s which is a way smaller than a compressibility limit of 100 m/s. A finite volumes method (FVM) was used to obtain a numerical solution of the equations. Volume of Fluid (VOF) method (Chen & Kharif, 1999; Hirt & Nichols, 1981) with piecewise linear interface calculation (PLIC) (Youngs, 1982) was utilized to model the two-phase flow of immiscible liquids with a free surface. This is a very common approach in microfluidics used by many authors (Chii-Dong et al., 2011; Gupta, Fletcher, & Haynes, 2009; Kositanont et al., 2011) According to the VOF method, both phases are considered as a single effective fluid but with variable properties. This allows to use a single continuity and momentum equations for a cost of introducing an additional indicator or color variable  $\alpha$  and an equation for it. It has a value 0 for one phase and 1 for another. In transition region close to the interface it has values in-between. This approach simplifies numerical calculations considerably while maintaining good accuracy. In some literature this indicator variable is referred to as a volume fraction, because its numerical representation for a two-component flow can be considered as a volume fraction of one component inside a computational element. The interface is captured as a region with a sudden change of fluid properties, i.e. change of its "color". With this, the free surface can be tracked for unsteady fragmentation and merging processes.

A surface tension force on the fluid interface was resolved by imposing a continuous surface force formulation (CSF) (Brackbill, Kothe, & Zemach, 1992). This formulation replaces the actual surface force by its volumetric representation in such a way, that the surface integral of the actual surface force over the interface element is replaced by the volume integral over the domain containing that surface element. This formulation allows to handle the force as a continuous volume field instead of imposing a pressure drop boundary condition on the interface. It is a way more convenient for the VOF method, and gives the correct integral values of the surface tension force.

The model equations can be written as follows:

Continuity equation:

$$\vec{\nabla} \cdot \vec{V} = 0 \quad (1)$$

<sup>1</sup> Reprinted from Chemical Engineering and Processing: Process Intensification, vol. 50, W. Ratchanansorn, D. Semyonov, D. Gudarzi, E. Kolehmainen, I. Turunen, Hydrodynamics and mass transfer studies on a plate microreactor, pages 1186–1192, 2011 with permission from Elsevier.

<sup>2</sup> See footnote 1.

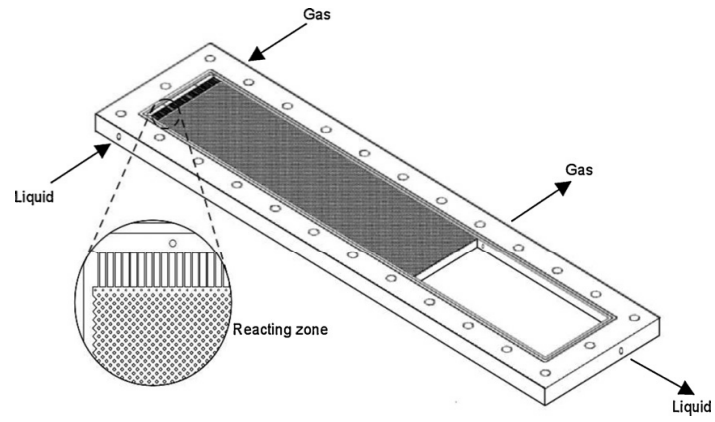


Fig. 2. Microreactor plate.

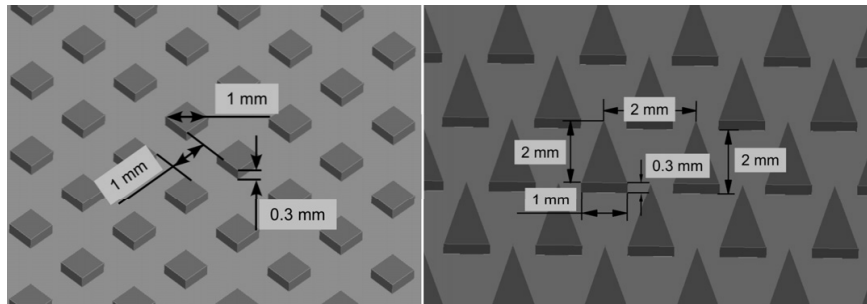


Fig. 3. Detailed view of the plates' (right and left) microstructure.

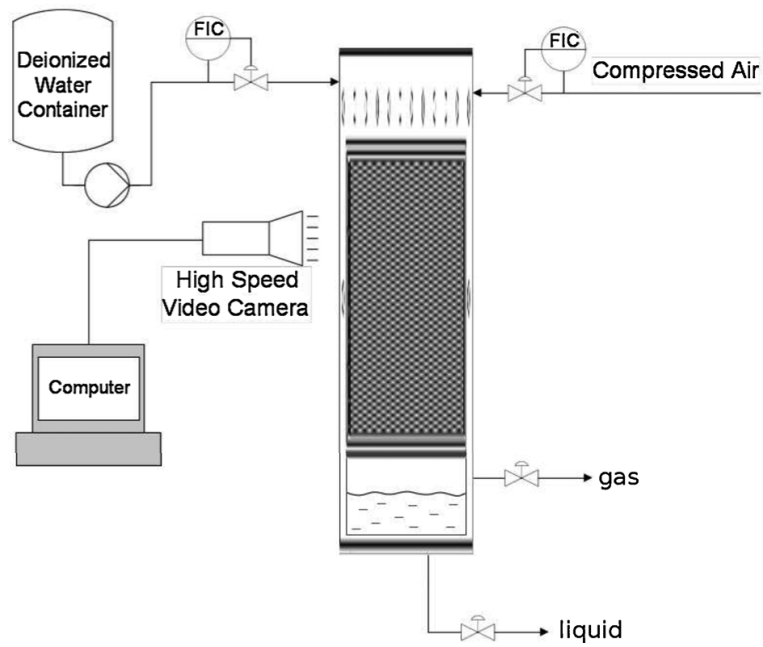


Fig. 4. Scheme of experimental setup.

Momentum equation for a single effective phase in a divergence form:

$$\frac{\partial(\rho\vec{V})}{\partial t} + \vec{V} \cdot \vec{\nabla}(\rho\vec{V}) = -\vec{\nabla}p + \mu\Delta\vec{V} + \vec{F}_{stv} \quad (2)$$

Equation for the indicator variable without the mass transfer is just a one-specie convection equation:

$$\frac{\partial\alpha}{\partial t} + \vec{V} \cdot \vec{\nabla}\alpha = 0 \quad (3)$$

Or in a form, more convenient for flux approximation, taking into the account (1):

$$\frac{\partial\alpha}{\partial t} + \vec{\nabla} \cdot (\alpha\vec{V}) = 0 \quad (4)$$

where  $\rho = \alpha \cdot \rho_1 + (1 - \alpha) \cdot \rho_g$  is the weighted average density,  $v = \mu/\rho = \alpha \cdot v_1 + (1 - \alpha) \cdot v_g$  is the weighted average kinematic viscosity and  $\vec{F}_{stv}$  is the CSF formulation of the surface tension force defined as in Brackbill et al. (1992):

$$\vec{F}_{stv} = \sigma\kappa \frac{\vec{\nabla}c}{|c|} \frac{\rho}{(\rho)} \quad (5)$$

where  $c$  is the color variable,  $[c] = c_l - c_g$  – its total jump over the fluid interface,  $(\rho) = (1/2)(\rho_1 + \rho_g)$  is the average density and  $\sigma$  is the surface tension coefficient.

The interface curvature:

$$\kappa = \vec{\nabla} \cdot \vec{n} \quad (6)$$

where  $\vec{n} = \vec{\nabla}\alpha/|\vec{\nabla}\alpha|$  is the unit vector normal to interface.

Although originally Brackbill et al. (1992) proposed density as a color variable for incompressible flows, nowadays indicator variable  $\alpha$  is more often used. Taking into account that  $[\alpha] = 1$ , we can rewrite Eq. (5) as:

$$\vec{F}_{stv} = \frac{2\sigma\kappa\rho\vec{\nabla}\alpha}{(\rho_1 + \rho_2)} \quad (7)$$

The flow in the microreactor is strictly non-stationary, therefore a transient formulation of the equations is used. The VOF formulation gives good flexibility to add more components and reactions for future studies. To add the reaction further it is needed to add a corresponding source term to Eq. (3) or (4). To add more components – define more levels of  $\alpha$  instead of just 0 and 1.

### 3.1. Non-dimensional analysis

To see, which forces in the flow playing important roles, a non-dimensional analysis was carried out. By choosing channel's width as the length scale  $L = 10^{-3}$  [m], and using the preliminary computed mean fluid velocities in the microreactor, the Reynolds number can be estimated for water as:

$$Re = \frac{vL}{\nu} = \frac{0.1 \dots 0.5 \text{ m/s} \times 10^{-3} \text{ m}}{10^{-6} \text{ m}^2/\text{s}} \approx 100 \dots 500$$

For air,  $Re \approx 10$ . This means that the flow can be considered laminar in the reacting zone, and there is no need to use additional turbulence models.

The range for the Capillary number is estimated as:

$$Ca = \frac{\mu v}{\sigma} = 0.001 \dots 0.055$$

This means that both viscosity and surface tension forces are playing equal roles in the flow.

The Weber number is:

$$We = \frac{\rho v^2 L}{\sigma} = 0.04 \dots 65$$

Therefore both inertia and viscosity forces are important in the flow.

The Bond number is:

$$Bo = \frac{\rho g L^2}{\sigma} \approx 0.01$$

So the gravity is dominated by the surface tension in the flow and therefore can be excluded from the consideration.

Non-dimensional analysis of the flow shows, that all forces except gravity should be taken into the account. In such an unpredictable flow pattern, as present in the investigated microreactor, at some conditions one force may take the upper hand and at another – the other. In general, it can be concluded, that all three forces: the inertia, the viscosity and the surface tension have an equal effect on the flow.

### 3.2. 2D approximation to a 3D flow

By utilizing the properties of the microreactor, in particular, the fact that it is very thin and the flow there is laminar, the real 3D flow in the microreactor can be replaced by a 2D formulation. This significantly reduces the computation costs. It is assumed here and everywhere below, that the microreactor's width is (only in left image) along the  $X$  axis, length is along the  $Y$  axis and thickness is along the  $Z$  axis. In a preliminary study it has been found that the velocity of the flow between the plates or in a square channel for a two-phase flow quickly obtains a parabolic profile in the  $Z$  direction, i.e. the flow is laminar for both phases. This was also reported by other authors for a Taylor flow in circular channels (van Baten & Krishna, 2004). Therefore it is possible to search for the solution for a mean velocity field in the  $X$ – $Y$  centerplane of the microreactor. To find then a real velocity in the centerplane, one should multiply the found mean velocity by a factor 1.5, obtained by integrating the parabolic profile along the  $Z$  direction. The same is also valid for the pressure and colour variable fields.

Modifications should be done to the model to correctly resolve the surface tension under a 2D formulation. For a general 3D case, the interface curvature can be presented as a sum of two terms:

$$\kappa = \frac{1}{R_x} + \frac{1}{R_z} = \kappa_{main} + \kappa_{add}$$

where  $\kappa_{main}$  is the curvature in the  $X$ – $Y$  plane. For a 2D model it will be calculated using (6) within the VOF procedure.

$\kappa_{add} = 1/R_z$  is the curvature in the plane, orthogonal to  $X$ – $Y$ . It will not be calculated within the VOF procedure in the 2D case, so to remain consistency with the 3D case, it should be added explicitly. In the general case, the bubble shape in  $Z$  direction depends on the bubble velocity and vary from the box with round caps to a bullet shape (Taha & Cui, 2006). Due to the unavailability of the experimental velocity scaling function for the bubble shape, it is assumed that the bubbles have the round shape which remains constant. This is a significant approximation, but the obtained results shows, that it is still reasonable. With this, the  $\kappa_{add}$  can be calculated explicitly and used as a model parameter. The particular value of this parameter is fully defined by the contact angle on top and bottom plates and by the distance between the plates using a geometric formula (for the same contact angles on the top and the bottom plates):

$$\kappa_{add} = \frac{2 \cos \theta}{h_z} \quad (8)$$

where  $\theta$  is the contact angle and  $h_z = 300$  [ $\mu\text{m}$ ] is the distance between the plates.

Another thing which should be considered when shifting from 3D equations to 2D equations is the correct modelling of friction pressure losses, which plays an important role in this and similar

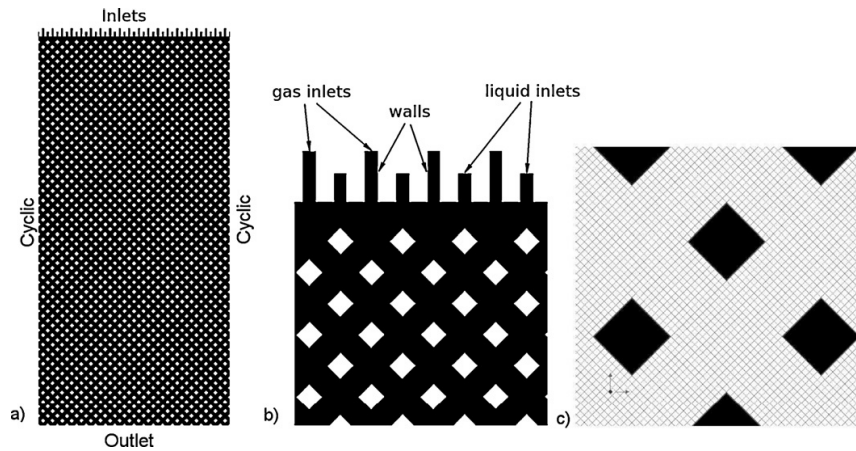


Fig. 5. Computational domain with boundary types (a), close-up of the inlet section (b), and a close look at the computational mesh (c).

cases. The 3D model computes the wall friction forces implicitly using the momentum equations and boundary conditions, but in 2D formulation wall friction will be correctly computed only for the side walls of the microreactor and structural elements. The friction on the top and the bottom walls, which are parallel to the  $X$ - $Y$  plane, will not be computed implicitly, so, like for the surface tension forces, it should be added explicitly to the model. From the viscous flow theory one can derive a formula for the pressure gradient due to the friction in a flow between two parallel infinite plates:

$$\vec{\nabla} p|_{\text{friction}} = -\frac{12\mu\vec{V}}{h_z^2}$$

This gradient can be considered as a volumetric friction force, acting in the averaged over the  $Z$  direction 2D flow. Therefore it can be added as a source term into the right hand side of the momentum equation (2):

$$\frac{\partial(\rho\vec{V})}{\partial t} + \vec{V} \cdot \vec{\nabla}(\rho\vec{V}) = -\vec{\nabla}p + \mu\Delta\vec{V} + \vec{F}_{stv} - \frac{12\mu\vec{V}}{h_z^2} \quad (9)$$

This approximation for infinite plates does not fully holds in the real channel case, where corner effects exist, but it is still good enough to be used in this case.

### 3.3. Final model formulation

The final model used in this study consists of a system of four partial differential equations (PDEs): the continuity equation (1), 2 projections of the momentum equation (9) and the equation for the color variable (4). This system can be resolved numerically for a given set of initial and boundary conditions.

## 4. Case definition

### 4.1. Geometry

A geometry, in which the numerical solution of the specified equations is searched, was created. In order to reduce the problem size only an idealized case with the fully developed flow and the favourable chaotic flow pattern is considered. Therefore the real microreactor with real inlets and a region with developing flow were not modelled. Instead, only the flow in the bottom part of the microreactor is modelled. Results, obtained from such case can be

considered as a limiting case, as if the flow was fully developed everywhere inside the microreactor. A flow evolution from the inlets into the fully developed were not studied. To do so, the computational domain geometry as well as boundary conditions were set appropriately. Inlet section of the computational domain was constructed in order to achieve a complete mixing of the gas and liquid streams already from the beginning of the domain. Unlike in the real inlet section where only part of the gas inlets are in operation and the flow rates through the different gas and liquid inlets are different, here, in the computational domain all the inlets should be operational and all the flow rates should be the same. Example of the geometry of the computational domain is presented in Fig. 5(a) and (b). Here the model inlet section does not reflect the real inlet section. The purpose of the model inlet is to get a fully developed flow for the most part of the computational domain. Otherwise there would be a waste of computed results, because only the fully developed flow is of interest and only the region with the fully developed flow is used to compute the mean quantities. The size of the modelled part was typically 24 mm × 75 mm (width by height) for the square structural elements and 24 mm × 64 mm for the triangular ones. Typically 10 and 12 pairs of gas and liquid inlets were used correspondingly for these domain sizes. Gas and liquid inlets have the same size. Width of a single inlet is 0.5 mm. Considered part was large enough to get the average hydrodynamic parameters for the fully developed flow. Geometry was prepared by an in-house Fortran-90 code, which creates the specified geometry in a commonly used IGES (Initial Graphics Exchange Specification) format (Formerly ANS US PRO/IPO-100-1996, 1996).

### 4.2. Computational mesh

Preliminary estimations showed that the maximal computational element size should not exceed 100 μm, otherwise the algorithm is unable to correctly resolve the interface between the two phases and therefore important small-scaled phenomena. Mesh length scale used to discretize the geometry was 40–80 μm. With 40 μm mesh length scale the problem size becomes 990,000 elements for the first plate and 770,000 elements for the second. More coarse meshes were tested, but they give less accurate results. Example of the mesh is presented in Fig. 5(c). Necessity to use very small mesh length scale was a limiting criteria for the domain size, because the simulations with the mesh of a full-size microreactor cannot be completed for a reasonable time with a given computational resources.

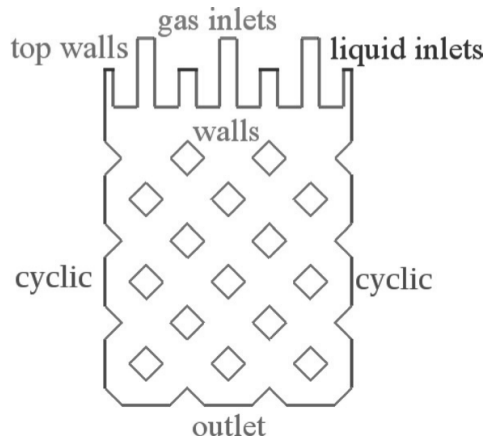


**Fig. 6.** Schematic view of boundary types of the computational domain. (For interpretation of the references to color in this figure legend, the reader is referred to the web version of the article.)

As it has been showed in Lopes and Quinta-Ferreira (2009), mesh and algorithm parameters have a great impact on the result reliability of the VOF method. In the present study, the numerical algorithms were selected to be optimal ones, but the mesh size could not be sufficiently optimized due to the computation power limitations.

#### 4.3. Boundary conditions

Boundary types for the specified domain are depicted in Fig. 6. Corresponding boundary conditions are as follows:

- Average gas and liquid velocities were set at the corresponding inlets. They are calculated to give the same inflow conditions as in the experiments. Values used for the gas inlet velocity for the first microplate are 0.1, 0.3 and 0.5 m/s, which correspond to the gas flow rates of 36, 108 and 180 ml/min in the reality. Values for the second microplate were 0.08, 0.24 and 0.4 m/s which corresponds to the same flow rates 36, 108 and 180 ml/s. Water velocity was fixed to 0.15 m/s for the first plate and to 0.12 m/s for the second, which corresponds in both cases to 54 ml/min in the full-scale microreactor.
- Different  $\alpha$  values were used to distinguish the gas and the liquid inlets:  $\alpha$  was set to 0 at the gas inlet, and to 1 at the liquid.
- Zero static pressure outlet condition was used.
- A no-slip condition was imposed on the walls of the structural elements in the reaction chamber.
- A free-slip condition was imposed on the top walls (coloured green in Fig. 6) which are close to the inlets. This is done in order to decrease the effect of computational inlet on the flow distribution and reduce the possible region with developing flow, to obtain already a fully developed flow as close to the inlet part as possible.
- A zero contact angle for all surfaces was assumed as proposed in literature (Bretherton, 1961). The real gas–liquid–solid contact angle should be used only for the cases with a real simultaneous contact of 3 phases. In this and similar cases the gas phase very seldom has a contact with walls, because of presence of a thin liquid film on the walls. For the gas holdup and the velocity range used in this case the liquid film on the wall remains permanent. Numerical simulations of Taylor bubbles in microchannels also prove this assumption (Gupta et al., 2009; Taha & Cui, 2006).

- A cyclic boundary condition was imposed on left and right domain borders to reduce the effect of the smaller domain width on the flow.

Initial conditions were set to be zero for the velocity and pressure fields. Volume fraction  $\alpha$  was set to be 1 everywhere, which means that the microreactor is initially filled with water.

#### 4.4. Obtaining a solution

Numerical solution of this system with given boundary and initial conditions was obtained using the open-source CFD library package OpenFOAM. A predefined solver module “interFoam” which implements the VOF method was used as a basis for modifications. It was then modified accordingly to contain the described model. It should be noted that the original implementation of the VOF method in interFoam does not have the  $2\rho/(\rho_1 + \rho_2)$  factor for the surface tension force, as in Eq. (7). This term might not be so crucial for a macro-scale computations, but in micro-scale, as in the considered microreactor, the lack of this term leads to the high parasitic currents close to the interface in a light fluid (gas phase here). A pre-computed value of the additional curvature was added to the curvature, computed in the interFoam for a 2D case. Using the formula (8), for  $h_z = 300$  [ $\mu\text{m}$ ] and  $\theta = 0^\circ$ , this value equals to 6667 [ $\text{m}^{-1}$ ]. The friction term from Eq. (9) was also added to the code.

Linear discretization schemes were used to compute gradients and laplacian. Linear interpolation was used to obtain values on the computational cell faces from the cell-centred values. Discretization scheme for the divergence of the indicator  $\alpha$  includes also the interface compression term to keep the interface sharp. With this term the actual equation for the  $\alpha$  (4) becomes:

$$\frac{\partial \alpha}{\partial t} + \vec{\nabla} \cdot (\alpha \vec{V}) + \vec{\nabla} \cdot (\alpha(1 - \alpha) \vec{V}_r) = 0 \quad (10)$$

The appropriate value for the interface compression velocity  $\vec{V}_r$  has been already settled in the library.

Explicit Euler time-stepping was used for the time marching. Timestep was automatically adjusted based on the predefined limiting Courant number. Several limiting Courant numbers were tested – 0.2, 0.5 and 0.8. It has been found that the solution does not depend on these values provided that the local Courant number do not exceed the stability limit  $Co < 1$ . The most robust limiting Courant number was 0.2 for which the solution never becomes unstable. For the higher values, the solution may become unstable under certain conditions.

0.8–1.5 s of simulated time are needed to obtain a fully developed flow from the specified initial conditions.

#### 4.5. Parallel computing

Because the problem size is considerably large, it cannot be solved in a reasonable time using only one processor. Parallel computing is implemented with the help of routines included in the OpenFOAM package. They allow the distribution and solution of the problem using unlimited number of processors based on a message passing interface (MPI). The specified problem was solved with the help of supercomputers of the Finnish Center for Scientific Computing (CSC). Scalability tests showed that the problem of this size scales well up to 128 processors, but the optimal number of 64 processors was used to distribute the problem. With this number of processors it takes approximately 50–150 h of a wall-clock time, depending on a case, to obtain a fully developed flow in the whole computational domain.

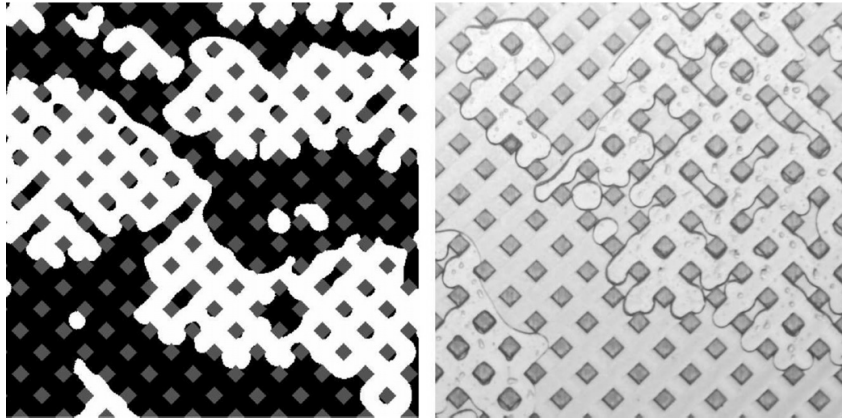


**Fig. 7.** Comparison of flow patterns obtained from the model (left) and from the experiments (right) for the first prototype. White/bright color – gas bubbles, black/dark – liquid, grey – structural elements.

## 5. Results and discussion

The results were first compared visually. An example of a such comparison for the square-structured microplate is presented in Fig. 7. Corresponding results for the triangle-structured microplate are in Fig. 8. In these figures a bright/white color represents a gas phase and a dark/black color represents a liquid phase. Square structural elements are of grey colour. On the experimental photo of the flow in a triangle-structured microreactor (Fig. 8, right) structural elements are not seen because the material of the plate has the same refraction index as the water. Experimental figures were taken from the bottom-central part of the reactor, where the flow was fully developed. From these figures it can be seen that the model was able to capture most of the small-scale phenomena in the studied two-phase flow, such as separate gas bubbles of different size, liquid enclosures inside gas bubbles and liquid droplets on structural elements. This comparison indicates that the model is adequate in principle to resolve the flow. For a more strong model validation quantitative comparison has been done. In the framework of the hydrodynamic study of the microreactor the quantitative parameters were the interfacial area of gas bubbles

and the gas holdup in the flow. The experimental data was obtained from the parallel research (Ratchananusorn et al., 2011). A set of images similar to the one shown in Fig. 7 (right) and Fig. 8 (right) was obtained for the every operating condition in the range specified above in Section 4. Similar images with flow patterns were obtained from the CFD simulation. Both sets of images were then processed by an image processing routine written in Matlab to calculate the mentioned quantities. The same routine was used for the both experimental and simulated images to ensure the comparability of the obtained values. Due to a natural troubles of obtaining and processing images with the real flow pattern, accuracy of estimated experimental values is much lower than of simulated ones, especially for the first prototype where the accuracy approaches to 20%. Accuracy of the simulated parameters was high because of appropriate choice of the numerical domain size and the simulated time. The image size with the flow pattern in the first microreactor prototype with square elements was relatively small, because only small portion of the full raw image was appropriate for the image processing. This yields in the lower accuracy of the estimated average parameters.

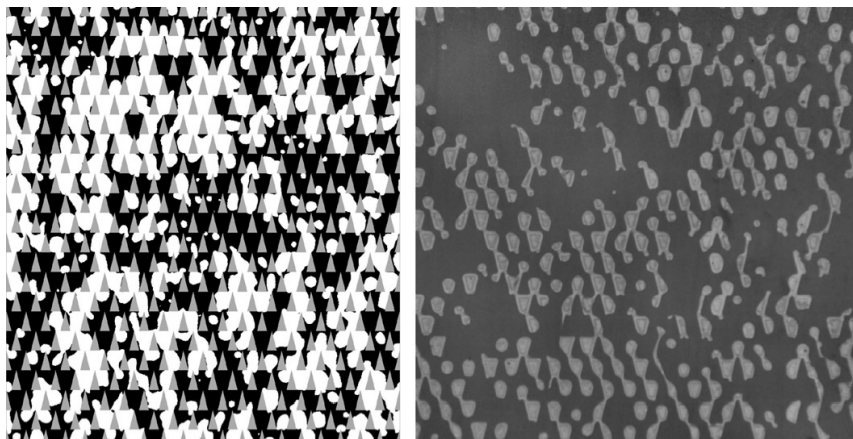


**Fig. 8.** Comparison of flow patterns obtained from the model (left) and from the experiments (right) for the second prototype. White/bright color – gas bubbles, black/dark – liquid, grey (only in left image) – structural elements.

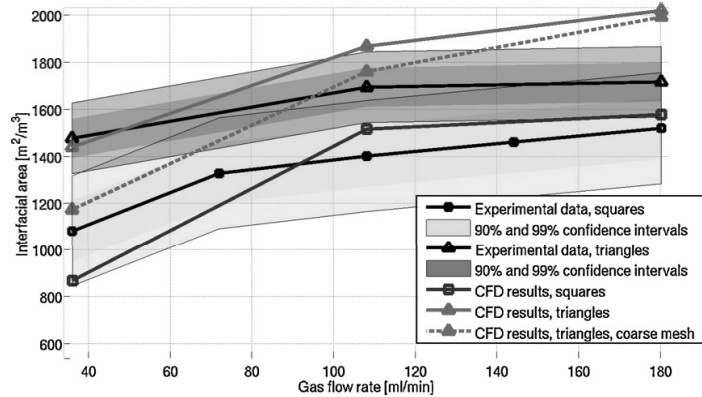


Fig. 9. Comparison of the experimental and simulated interfacial area. (For interpretation of the references to color in this figure legend, the reader is referred to the web version of the article.)

The interfacial area was calculated based on the perimeter of the gas bubbles excluding the top and bottom sides of the gas bubbles. Comparison between the experimental and the simulated interfacial area is shown in Fig. 9. Corresponding comparison plots for the gas holdup and gas to liquid residence time ratio are presented in Figs. 10 and 11.

It can be seen, that there is a relatively good match between the simulated and the experimental data. The error between them does not exceed 20% in the worst case. Simulated data follow all the trends for both square-structured and triangle-structured plates, but it is also noticeable that for the higher flow rates the model gives values higher than the experiments, especially for the microplate with triangles. This indicates that the model is still more idealized than the reality and does not take into account phenomena which occur on a very large scale. An assumption was made that the channeling phenomenon was presented in the flow, i.e. when all or part of the incoming gas is not actually evenly distributed in the reactor and mixed with the liquid, but rather travels at high speed on a particular route, or channel through the liquid phase. A channeling, captured by the simulation is presented in Fig. 12. From there it can be seen that even when the average flow speed does not exceed 0.2–0.5 m/s, there are almost always exist streams with the velocity considerably higher than the average. Velocity in such streams

may exceed 2 or even 4 m/s. These streams usually are not permanent and disappear completely after tens of milliseconds in the simulation. In the experiments they may last longer – up to several seconds, making the mixing of the gas and the liquid worse than the simulations show. When looking at the velocity plots, the whole phenomenon looks like appearance of thunderbolts – the streams of different size and strength keep emerging in the flow randomly in the different parts of the computational domain. Another explanation of the overestimation of the flow parameters is that the model gives an ideal fully developed flow, but in the reality the flow might not still be as well developed as in the model.

From Fig. 10 it can be seen that in the test reactors after some point the gas holdup almost does not rise as the gas inflow rate increases. This might indicate that the flow there is purely dominated by the channeling effect and all excess of the gas is just flushed through the reactor. CFD results are a bit more optimistic and show that the gas holdup slightly increases as the inflow rate grows, but they are also far from the theoretical holdup (Fig. 10, dashed line). Theoretical gas holdup represents the case when gas and liquid has the same residence time, i.e. when no phase travels through the microreactor faster than another, then gas and liquid superficial velocities should be proportional to their corresponding flow rates. Both the model and the experiment show that for

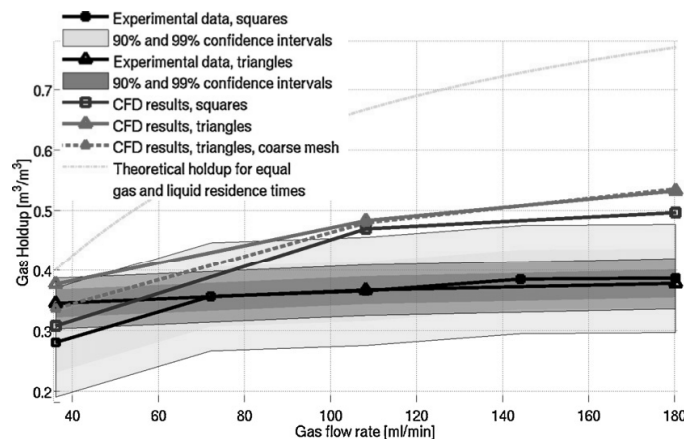


Fig. 10. Comparison of the experimental and simulated gas holdup. (For interpretation of the references to color in this figure legend, the reader is referred to the web version of the article.)

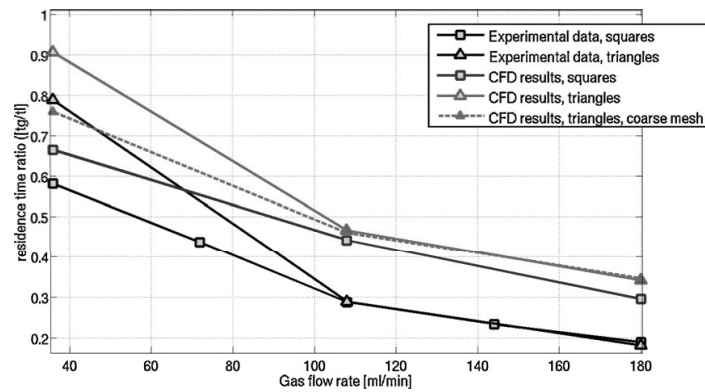


Fig. 11. Comparison of the experimental and simulated gas to liquid residence time ratio. (For interpretation of the references to color in this figure legend, the reader is referred to the web version of the article.)

the high flow rates the gas superficial velocity is much higher than it should be, which also might indicate the presence of the gas channeling similar to the depicted in Fig. 12. This means that the model is able to capture the channeling, but because of the computational domain size and the uniform distribution of phases at the inlet, it is not as strong, as in the reality, and therefore the results are more optimistic. For the low flow rates the model gives quite accurate predictions for the interfacial area and the gas holdup. The gas holdup now is much closer to the theoretical one, which may indicate that the channeling effect is low. Fig. 11 indicates that as the gas inflow rate increases, the average gas residence time inside the reactor becomes smaller and smaller compared to an average liquid residence time. This means that the gas superficial velocity grows non-linearly as the gas flow rate increases. This

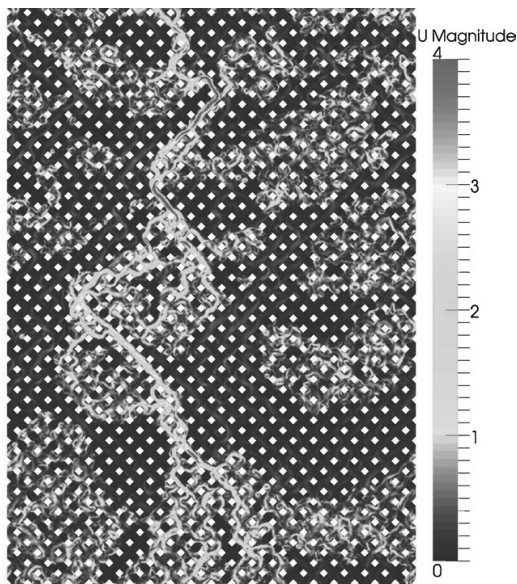


Fig. 12. Velocity plot with the channelling effect for the square-structured plate at gas flow rate 108 ml/min and liquid flow rate 54 ml/min. (For interpretation of the references to color in this figure legend, the reader is referred to the web version of the article.)

confirms the proposal, that for the higher flow rates, the channeling effect is stronger. For the low flow rates the residence times ratio approaches unity, i.e. theoretical optimal rated conditions without any gas flushing. Here it is also can be seen that at lower flow rates the triangular-structured microplate performs much better than the square-structured microplate – the channeling effect is smaller there, while for a higher flow rates the plate structure seems does not affect on the channeling. This can be seen from both the simulated and the experimental data, which proves, that the model is able to describe the important flow phenomena.

With a more coarse mesh with edge length twice as big (80  $\mu\text{m}$ , dashed line in Fig. 9) the model gives roughly the same results for the higher flow rates, but for a lower flow rates the results are considerably lower. Lower interfacial area can be due to two facts: the more coarse mesh unable to resolve smallest bubbles which are resolved by the more fine mesh and therefore the total area of bubbles is smaller, or the coarse mesh introduces significant amount of numerical viscosity, which is not important for the higher flow rates, but plays a significant role in a bubble formation mechanism at low flow rates. Because the coarse mesh gives roughly the same values as the fine mesh for the high flow rates, it can be concluded that the coarse mesh is still able to resolve as many bubbles as the fine one, especially taking into account that for the higher flow rates portion of smaller bubbles in the flow is larger than for the lower flow rates. Therefore it is possible to conclude that at the low flow rates viscosity forces dominates in the flow, while at the high flow rates they are not that important in the bubble formation mechanism. Effect of the coarse mesh, i.e. the greater numerical viscosity on the gas holdup and the residence times ratios at high flow rates is negligible, while for the lower flow rates coarse mesh gives smaller values. With this, a proposal can be made that at the higher flow rates the channeling (or in other words, the inertia) is the effect which defines the flow and limits the bubble formation, meanwhile at low flow rates the bubble formation is limited by the viscosity.

## 6. Conclusion

A CFD model of an existing microreactor was developed and implemented. The model is based on the open-source CFD toolbox OpenFOAM. The VOF-PLIC method was used to model a flow with free surface. CSF method was used to model the surface tension force. The model is able to describe most of the general phenomena of non-reacting two-phase gas liquid flow in the microreactor. The model is designed to describe a fully developed flow. It cannot

compute developing or stagnant flows, which are present in the upper and side parts of the real microreactor prototypes.

Computed values of the interfacial area are in a good agreement with the experiment for the first prototype, but overestimated for the second one at high flow rates. Computed values of the gas holdup are in an agreement with the experiment for low flow rates, but higher for the higher flow rates. The reason, why the model over-predicts the experiments is that the model considers the ideal fully developed flow, which still may not be true in reality. For the high flow rates the gas holdup is considerably lower than the theoretical value for both the experiments and the simulation. It was proposed that the reason for that is the gas channeling. The model was able to adequately resolve the channeling and to show that there is a significant channeling exist even in the idealized fully developed flow. The model was successfully implemented to select an optimal plate structure for the second prototype. The second prototype with the triangular structured microplate was built based on the CFD simulation results, and the enhancement in the interfacial area and the mass transfer then have been observed experimentally. It can be concluded that the model suits well for the structured plate microreactors.

Effect of channeling and liquid viscosity on a bubble formation inside the microreactor has been also studied with the help of the model.

Although the model considers only fully developed flow, it gives comprehensive enough results, has acceptable accuracy and a reasonable computation time. It also proved its applicability. Application area of the model is limited because of simplifications.

The model is valid for the structured plate multiphase microreactors, where the gas or liquid cannot flow above the structural elements. Reactor should be sufficiently thin, so the laminar flow with parabolic profile assumption can be fulfilled.

The presented model resembles several features compared to other methods which can be found in the literature. It is able to resolve the unsteady flow with complex evolution of the phase interface in a considerably large domain. The accuracy of the model is good enough to compute macroscopic flow parameters such as interfacial area and gas holdup directly from the images, obtained in the CFD simulations. The model was successfully reduced from 3 dimensions to 2, yet maintaining reasonable accuracy. The reduction made the problem feasible for the numerical simulation using the supercomputer power.

## Appendix A. Supplementary Data

Supplementary data associated with this article can be found, in the online version, at: doi:<http://dx.doi.org/10.1016/j.compchemeng.2012.12.006>.

## References

- Al-Rawashdeha, M., Hessela, V., Loba, P., Mevissena, K., & Schonfelda, F. (2008). Pseudo 3-D simulation of a falling film microreactor based on realistic channel and film profiles. *Chemical Engineering Science*, *63*, 5149–5159.
- Brackbill, J., Kothe, D., & Zemach, C. (1992). A continuum method for modeling surface tension. *Journal of Computational Physics*, *100*, 335–354.
- Bretherton, F. P. (1961). The motion of long bubbles in tubes. *Journal of Fluid Mechanics*, *10*, 166–188.
- Chen, G., & Kharif, C. (1999). Two-dimensional Navier–Stokes simulation of breaking waves. *Physics of Fluids*, *11*, 121–133.
- Chii-Dong, H., Hsuan, C., Hsi-Jen, C., Cheng-Liang, C., Hsieh-Hsung, L., & Yin-Yu, C. (2011). CFD simulation of the two-phase flow for a falling film microreactor. *International Journal of Heat and Mass Transfer*, *54*, 3740–3748.
- Deshmukh, S. R., Mhadeshwar, A. B., & Vlachos, D. G. (2004). Microreactor modeling for hydrogen production from ammonia decomposition on ruthenium. *Industrial and Engineering Chemical Research*, *43*, 2986–2999.
- Formerly ANS US PRO/IPO-100-1996. (1996). *Initial Graphics Exchange Specification, IGES 5.3*. IGES/PDES Organization.
- Gupta, R., Fletcher, D. F., & Haynes, B. S. (2009). On the CFD modelling of Taylor flow in microchannels. *Chemical Engineering Science*, *64*, 2941–2950.
- Harries, N., Burns, J. R., Barrow, D. A., & Ramshaw, C. (2003). A numerical model for segmented flow in a microreactor. *International Journal of Heat and Mass Transfer*, *33*, 3313–3322.
- Hirt, C. W., & Nichols, B. D. (1981). Volume of fluid (VOF) method for the dynamics of free boundaries. *Journal of Computational Physics*, *39*, 201–225.
- Kashid, M. N., Agar, D. W., & Turek, S. (2007). CFD modelling of mass transfer with and without chemical reaction in the liquid–liquid slug flow microreactor. *Chemical Engineering Science*, *62*, 5102–5109.
- Kositantont, C., Putvisutisak, S., Praserttham, P., Assabumrungrat, S., Yamada, H., & Tagawa, T. (2011). Flow pattern of liquid multiphase flow in microreactors with different guideline structures. *Journal of Chemical Engineering of Japan*, *44*, 649–652.
- Lopes, R. J. G., & Quinta-Ferreira, R. M. (2009). Volume-of-fluid-based model for multiphase flow in high-pressure trickle-bed reactor: Optimization of numerical parameters. *AIChE Journal*, *55*, 2920–2933.
- Qian, D., & Lawal, A. (2006). Numerical study on gas and liquid slugs for Taylor flow in a T-junction microchannel. *Chemical Engineering Science*, *61*, 7609–7625.
- Ratchanusorn, W., Semyonov, D., Gudarzi, D., Kolehmainen, E., & Turunen, I. (2011). Hydrodynamics and mass transfer studies on a plate microreactor. *Chemical Engineering and Processing: Process Intensification*, *50*, 1186–1192.
- Taha, T., & Cui, Z. F. (2006). CFD modelling of slug flow inside square capillaries. *Chemical Engineering Science*, *61*, 665–675.
- van Baten, J., & Krishna, R. (2004). CFD simulations of mass transfer from Taylor bubbles rising in circular capillaries. *Chemical Engineering Science*, *59*, 2535–2545.
- Youngs, D. L. (1982). Time-dependent multi-material flow with large fluid distortion. *Numerical Methods for Fluid Dynamics*, *24*, 273–285.

## **Publication IV**

Gudarzi, D., Ratchananusorn, W., Turunen, I., Salmi, T., Heinonen, M. (2013)  
Preparation of Pd catalysts supported on activated carbon cloth (ACC) for  
direct synthesis of H<sub>2</sub>O<sub>2</sub> from H<sub>2</sub> and O<sub>2</sub>  
*Topics in Catalysis*, 56, 527-539.

Reprinted by permission of Springer Publishing  
© Springer Publishing



## Preparation and Study of Pd Catalysts Supported on Activated Carbon Cloth (ACC) for Direct Synthesis of H<sub>2</sub>O<sub>2</sub> from H<sub>2</sub> and O<sub>2</sub>

Davood Gudarzi · Warin Ratchananusorn ·  
Ilkka Turunen · Tapio Salmi · Markku Heinonen

Published online: 16 April 2013  
© Springer Science+Business Media New York 2013

**Abstract** Activated carbon cloths (ACCs) were used as supports for Pd catalysts. The catalyst preparation was carried out by the impregnation method using acidic solution of palladium dichloride (PdCl<sub>2</sub>) as metal precursor. The effects of the oxidation state of the loaded metal, heat treatment of the catalysts in different atmosphere (H<sub>2</sub>, air) at different temperatures and surface chemistry of the support on the catalyst characterizations and the catalytic activities were investigated. Wet oxidation of ACC was done by nitric acid in order to induce oxygen-containing surface functional groups. Surface chemistry of the support and oxidation state of the metallic phase was investigated by means of XPS, TPD, SEM, DTA and TGA tests. Direct synthesis of hydrogen peroxide from H<sub>2</sub> and O<sub>2</sub> was performed batch wise in a stainless steel autoclave. The reactions were conducted under high pressure (38 bar) at 0 °C and methanol was used as reaction medium. The direct synthesis results showed that the oxygen-containing surface functional groups increase the selectivity of the catalysts by reducing the rate of water production. Existence of the oxidized state of Pd (PdO) also makes the catalyst more selective than the corresponding zerovalent state (Pd<sup>0</sup>). PdO affected on selectivity by increasing the

rate of H<sub>2</sub>O<sub>2</sub> production and reducing the amount of production of water, simultaneously.

**Keywords** Hydrogen peroxide · Direct synthesis · Palladium catalyst · Activated Carbon Cloth · Catalyst characterization

### 1 Introduction

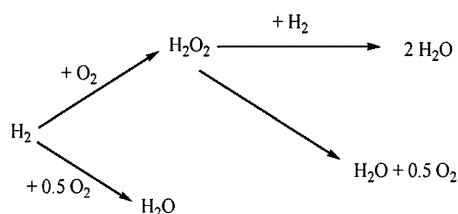
Hydrogen peroxide (H<sub>2</sub>O<sub>2</sub>) is one of the most powerful and environmentally friendly known oxidizers with a wide range of applications in pulp bleaching, waste water treatment, cosmetic and pharmaceutical industries. Commercially, hydrogen peroxide is mainly produced by the sequential hydrogenation and oxidation of an alkyl anthraquinone (auto-oxidation method). This method is more economical for large-scale production. The simplest method to produce hydrogen peroxide and the main challenger of anthraquinone auto-oxidation method is the direct catalytic synthesis of hydrogen peroxide from elemental hydrogen and oxygen. The direct method suffers from two serious technical challenges. Firstly, mixtures of hydrogen and oxygen are explosive over a wide range of concentrations (4–94 % H<sub>2</sub> in O<sub>2</sub>) [1]. Secondly, the catalytic reaction of hydrogen and oxygen involves several reaction pathways and most of them result in the production of water (Scheme 1). Mainly because of these two challenges, the direct method has not been commercialized yet even though it has been widely studied.

Supported Pd catalysts are the most common ones for the direct synthesis of hydrogen peroxide [2]. The most common supports have been carbon, silica (high surface area materials), alumina and silica-alumina (relatively low surface area materials). From these, activated carbon

D. Gudarzi (✉) · W. Ratchananusorn · I. Turunen  
Department of Chemical Technology, Lappeenranta University  
of Technology, Lappeenranta 53851, Finland  
e-mail: davood.gudarzi@lut.fi

T. Salmi  
Laboratory of Industrial Chemistry and Reaction Engineering,  
Åbo Akademi University, Turku 20500, Finland

M. Heinonen  
Department of Physics and Astronomy, University of Turku,  
Turku 20014, Finland



**Scheme 1** Reactions involved in the direct synthesis of  $\text{H}_2\text{O}_2$

materials as support have resulted in best activity and selectivity [3]. In addition, Pd on activated carbon has many advantages, e.g. chemical stability, availability, and easy recovery of Pd metal by just burning off carbon components [3]. Structured forms of activated carbons, such as activated carbon felts and activated carbon cloths (ACCs) represent promising alternatives due to their excellent characteristics and properties [4]. Literature concerning activated carbon cloths and felts as catalyst supports is relatively limited so far, while granular carbonaceous supports are well covered.

The direct catalytic synthesis of  $\text{H}_2\text{O}_2$  from  $\text{H}_2$  and  $\text{O}_2$  has remained a challenging research target for over 90 years [5]. Choudhary et al. [6] have shown that catalyst properties such as particle size and surface area are less important than the oxidation state of Pd in determining selectivity of Pd catalysts for this reaction. They have claimed that existence of the oxidized state of Pd ( $\text{PdO}$ ) makes the catalyst more selective than the corresponding zerovalent state ( $\text{Pd}^0$ ) catalyst [7–9]. In contrast, some studies have declared that higher  $\text{H}_2\text{O}_2$  activity and selectivity can be achieved with  $\text{Pd}^0$  catalysts [10–12]. Fu et al. [13] demonstrated that metal particle size and specific surface area affect less on  $\text{H}_2\text{O}_2$  yield and selectivity than the surface chemistry of the support. The acidity of the support is also an important characteristic of the Pd catalysts [5]. Pd catalysts on acidic support e.g.  $\text{Pd}/\text{SiO}_2$  were found to be more active than basic catalysts ( $\text{Pd}/\text{Al}_2\text{O}_3$ ) [5]. Using of halide ions (especially  $\text{Cl}^-$  and  $\text{Br}^-$ ) and protons ( $\text{H}^+$ ) as promoters, in order to improve the selective oxidation of  $\text{H}_2$  to  $\text{H}_2\text{O}_2$  over Pd-based catalysts, have been investigated in several papers [7–12, 14–26]. The catalytic performance of the Pd catalysts is also strongly dependent on the  $\text{H}_2:\text{O}_2$  composition, total pressure, and the reaction temperature. Low temperature, high pressure, and the presence of a stabilizer in the reactant all lead to improved yields of  $\text{H}_2\text{O}_2$  [5].

The goal of this paper is to study and test Pd catalysts on activated carbon cloth in the direct synthesis of  $\text{H}_2\text{O}_2$ . This kind of catalyst will be used in a novel microreactor [27].

## 2 Catalyst Preparations

A commercial activated carbon cloth ACC-5092-20 (Kynol Europa GmbH), after a thermal and a chemical treatment, was employed as support. Palladium (II) chloride ( $\text{PdCl}_2$ , purity 99.999 %, Sigma-Aldrich) was used as a precursor for the metallic palladium catalyst. Nitric Acid (Merck) was used for acid pretreatment of the support.

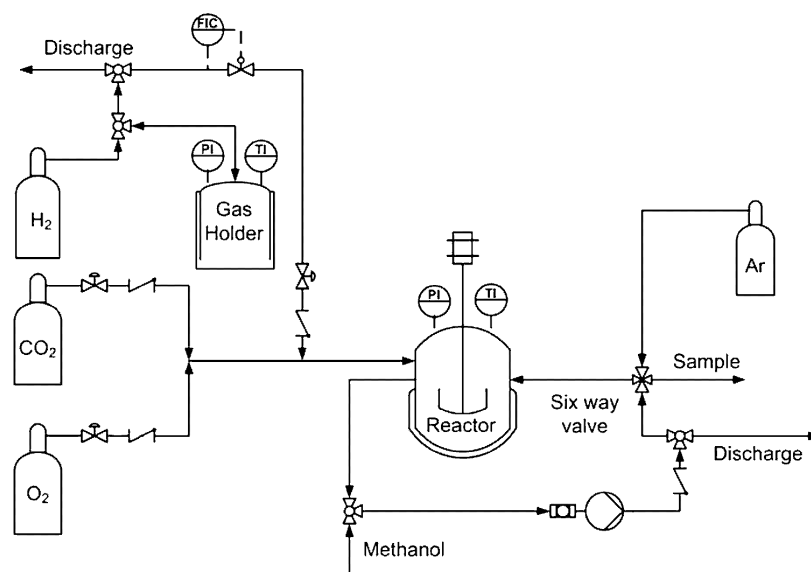
The activated carbon cloth was first treated in the oven at  $100\text{ }^\circ\text{C}$  for about 12 h. Then acid pretreatment was accomplished by a 20 % solution of nitric acid at room temperature for 40 h. After this oxidative treatment the samples were washed with distilled water until neutral conditions were reached, and then dried at  $100\text{ }^\circ\text{C}$  for 24 h. This sample is referred as oxidized ACC. Acid treatment is a common method to create oxygen-containing functional groups on the surface of activated carbon, to remove the mineral elements and to modify the surface of activated carbon materials [28–31].

A series of Pd catalysts on non-oxidized and oxidized activated carbon cloth were prepared by impregnation of the supports with an aqueous acidic solution of  $\text{PdCl}_2$  at room temperature for 12 h. The impregnation was done in a 100 ml reactor with stirring rate of 1,000 rpm. The ratio of the solution volume to catalyst mass was 200 ml/g. The concentration of the metal precursor between 174.9 and 874.68 mg/l for 1 g of the support gave palladium loading in the range 1–5 wt%. After impregnation, the catalysts were left at room temperature for 3 h, and then dried at  $60\text{ }^\circ\text{C}$  during 24 h. To investigate the effects of the oxidation state of the metallic phase on the catalytic performances, the dried fresh catalysts were finally treated with different processes. The reduced samples were prepared by treating the fresh dried catalysts with  $\text{H}_2$  at  $185\text{ }^\circ\text{C}$  under 3.5 bar overnight. A series of different calcined samples were prepared by oxidizing the fresh dried catalysts at temperatures 135, 185 and  $235\text{ }^\circ\text{C}$  in static air overnight. The calcination temperatures were selected according to the TGA/DTA results in order to be in the safe thermal treatment region of ACCs.

## 3 Characterization of the Catalysts

### 3.1 Textural Characterization

The distribution of pore volume with respect to pore size (pore-size distribution), the specific surface area and the pore volumes were deduced for each sample from  $\text{N}_2$  adsorption and desorption isotherms at  $-196\text{ }^\circ\text{C}$  in an automatic system Sorptomatic 1900 from Carlo Erba Instruments. Before  $\text{N}_2$  adsorption tests, the samples were treated by degasification process. For degassing, about

**Fig. 1** Experimental set up for direct synthesis of H<sub>2</sub>O<sub>2</sub>

200 mg of the sample was put in the sample tube and left for constant heating at 100 °C until the pressure was stable at  $1.06 \times 10^{-3}$  Pa. This treatment removed water, volatile impurities and other gases adsorbed or trapped in the porous texture. The surface area obtained from N<sub>2</sub> adsorption ( $S_{N_2}$ ) was calculated by using the Dubinin-Radushkevich equation.

### 3.2 Surface Morphology of the ACC and Pd/ACC Catalysts

Surface morphology of the ACC (oxidized and non-oxidized) and Pd/ACC catalysts were investigated by scanning electron microscopy (SEM). The SEM/EDS analysis was done by using a JEOL JSM-5800 microscope with X-ray detector for microanalysis (Noran Instrument Co.).

### 3.3 Thermal Analysis

Thermal characterization of the supports and the catalysts were done by differential thermal analysis (DTA) and thermogravimetry (TGA) using a NETZSCH STA 449 C Jupiter analyzer. Weight loss and heat flow during linear heating were measured. The analyses were done in oxidized conditions. He was used as protective gas and O<sub>2</sub> as purge gas. The flow rates of He and O<sub>2</sub> were 40 ml/min and 20 ml/min, respectively. The furnace was heated up from 20 to 700 °C with heating rate 5 °C/min.

The observed thermal effects in the TGA/DTA curves were interpreted according to the methodology presented by G. E. Shter et al. [32].

### 3.4 Characterization of the Surface Chemistry

The surface chemistry of the carbon materials is defined by the nature of the functional groups present on the surface. The surface chemistry of the oxidized and the non-oxidized activated carbon cloth was investigated by temperature programmed desorption (TPD) experiments. The TPD runs were carried out in a set-up made up of a U-shaped tubular reactor, placed inside an electrical furnace coupled to a Balzers OmniStar mass spectrometer for gas analysis. Around 200 mg of

**Fig. 2** Metal stand for catalyst installation in the autoclave

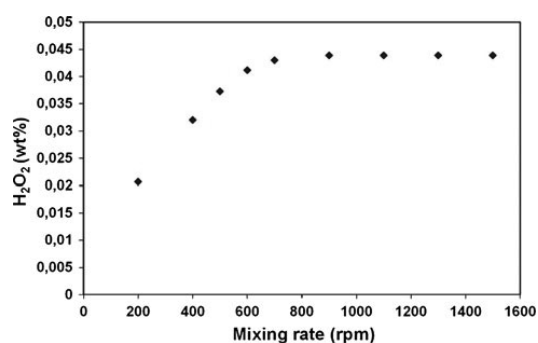


**Fig. 3** The effect of the mixing rate on the reaction rate (3 % Pd/OACC, mass of catalyst = 55 mg, temperature = 0 °C)

the samples were heated with the rate of 50 °C/min up to 900 °C. During the tests, He was passed through the reactor with the flow rate equal to 60 ml/min [4]. The amounts of CO and CO<sub>2</sub> desorbed from the different samples were monitored and recorded with the mass spectrometer.

### 3.5 Metal Phase Characterization

#### 3.5.1 The Amount of the Loaded Metal

Atomic absorption spectroscopy (AAS) was used to determine the amount of Pd in the support after impregnation, as well as the concentration (ppm) of Pd leached out into the solution during reaction. Latter figure was found out by determining the residual Pd content of the used catalyst and comparing it with that of the fresh catalyst. Atomic absorption spectroscopy was performed with a Thermo Scientific ICE 3000 series atomic absorption spectrometer using an air-acetylene flame.

#### 3.5.2 Oxidation State of the Metal Phase

The chemical state of the metal phase in the different catalysts was investigated by X-ray photoelectron spectroscopy (XPS). The spectra were obtained with a Perkin Elmer 5400 spectrometer, by using the Mg K $\alpha$  (1,253.6 eV) radiation of twin anode in the constant analyzer energy mode with pass energy of 37.75 eV. The pressure of the analysis chamber was maintained at

**Table 1** Textural properties of Non-oxidized and oxidized ACC with HNO<sub>3</sub>

Sample	$S_{N_2}$ (m <sup>2</sup> g <sup>-1</sup> )	Pore volume (cm <sup>3</sup> g <sup>-1</sup> )	Pore size distribution (nm)
Non-oxidized ACC	1,788	0.63	9–25
Oxidized ACC	1,520	0.54	8–25

$2 \times 10^{-7}$  Pa. The binding energy scale was calibrated by setting the Au 4f7/2 transition to 84.0 eV. The spectra were analyzed by using Unifit peak-fitting program.

## 4 Catalytic Activity

The direct synthesis of hydrogen peroxide was carried out in a stainless steel autoclave (Parr Instruments Ltd) with a nominal volume of 450 ml and a maximum working pressure of 140 bar. The autoclave was equipped with an overhead stirrer (0–2,000 rpm) and facilities to measure the temperature and pressure. Hydrogen was fed into the reactor through a gas-holder with a volume of 33 ml and by means of a mass flow controller. The gas-holder was used to measure the precise amount of hydrogen fed to the system. A recirculation line equipped with a six-way valve was installed for sampling at different times (Fig. 1). The sampling line was designed in a way minimizing pressure changes (and consequently, loss of gases) in the reactor during sampling. ACC catalysts were fixed in the reactor by means of a metal stand (Fig. 2). The position of the catalyst and the stirrer in the autoclave were selected to generate similar flow condition as in the microreactor. Typically, the reactor was charged with about 55 mg of catalyst and successively with carbon dioxide up to 15.2 bar. The pressure was thereafter elevated to 20.2 bar with oxygen and further to 35.2 bar with carbon dioxide again. Methanol was employed as reaction medium. 175 g of methanol was pumped in and the reactor was cooled down to around  $-1$  °C. Stirring (1,250 rpm) was begun after 2/3 of the methanol had been fed. Sufficient stirring speed for activity measurements was determined beforehand by carrying out a series of activity tests varying the stirring speed. As shown in Fig. 3, 1,250 rpm is sufficient speed to eliminate the effect of mass transfer phenomena. When the desired temperature was reached, the partial pressure of hydrogen was raised up to 3.2 bar by feeding

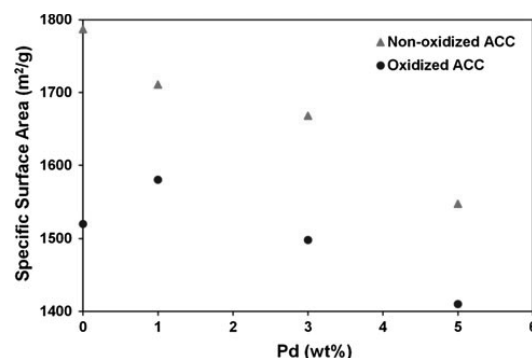
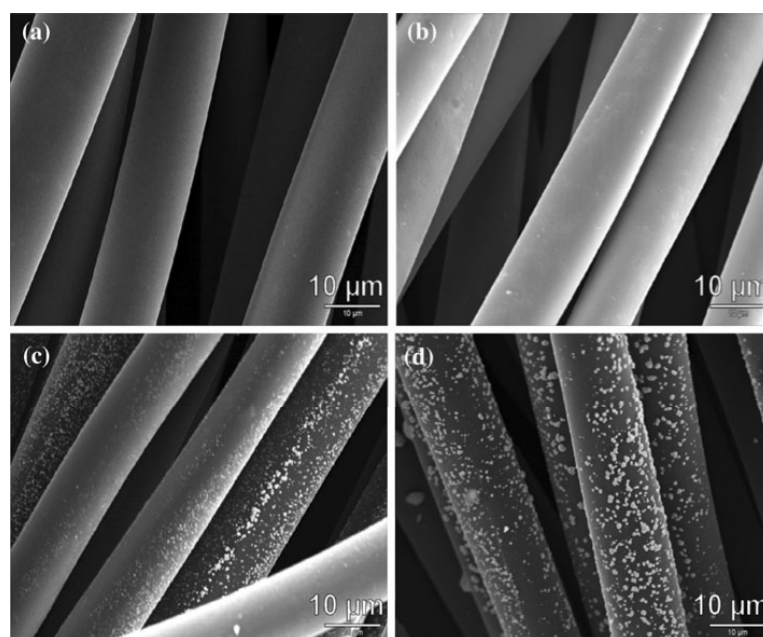


**Fig. 4** Specific surface area vs. Pd content of the Pd catalysts

**Fig. 5** SEM images of oxidized ACC with different Pd contents: **a** virgin oxidized ACC, **b** impregnated with 1 wt% Pd, **c** impregnated with 3 wt% Pd, **d** impregnated with 5 wt% Pd



from gas holder. The reaction time was now started. The tests were run for 3 h during which 11 samples were taken. During the experiments pressure went slightly down because hydrogen and oxygen were consumed.

The concentration of  $H_2O_2$  which was formed in the reaction was measured quantitatively by a volumetric iodometry titration method, whereas the produced water was determined by coulometric Karl–Fischer titration using a Mettler DL35 Karl–Fischer titrator. The water content in the reaction medium before catalyst addition was determined prior to each experiment. Research grade oxygen, hydrogen and carbon dioxide were purchased from AGA Gases. Methanol with a purity of 99.9 % was used as solvent (Merck). KI (Merck),  $CH_3COOH$  (Purity 100 %, Merck),  $K_2Cr_2O_7$  (purity 99.99 %, Aldrich) and  $Na_2S_2O_3 \cdot 5H_2O$  (Merck) were used for iodometric titration of hydrogen peroxide. Water formation was determined by Karl–Fischer titration using hydranal reagents (Fluka).

## 5 Results and Discussions

### 5.1 Catalyst Properties

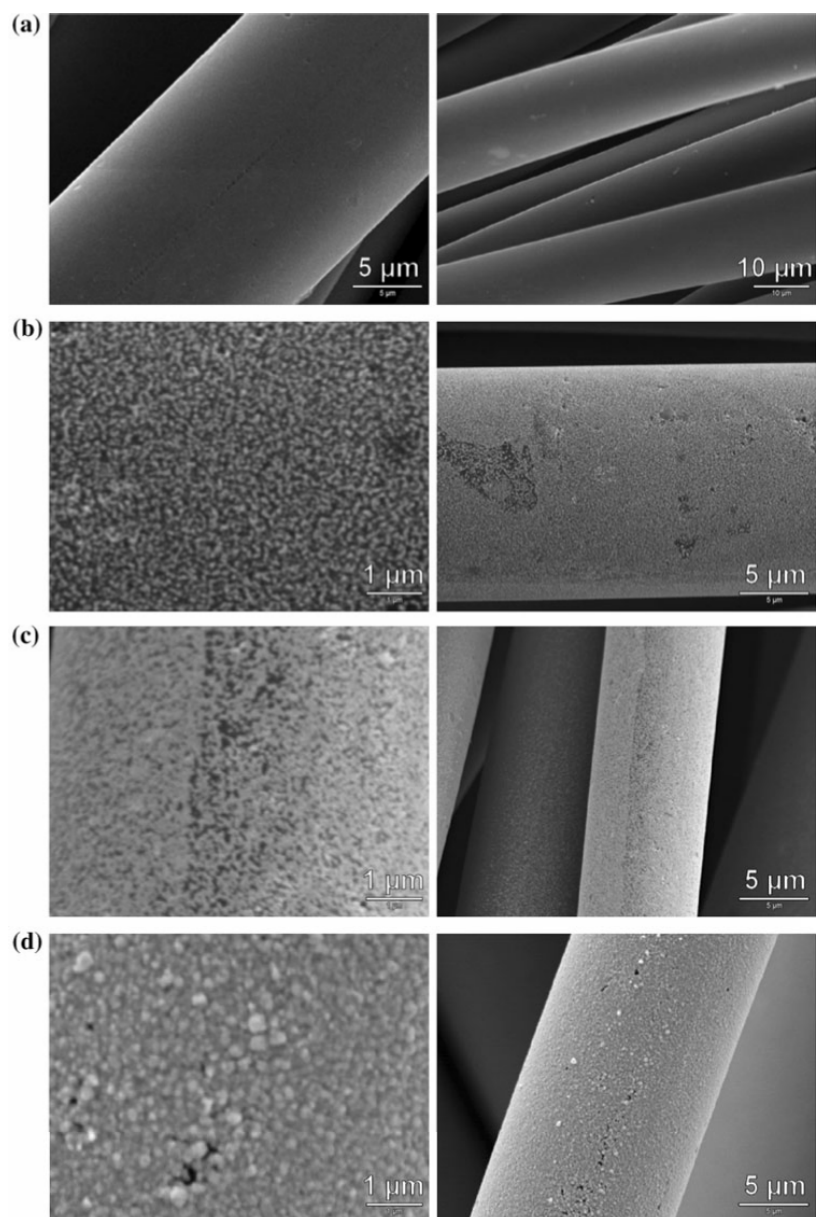
#### 5.1.1 Surface Morphology and Textural Characterization of the ACC and Pd/ACC Catalysts

Textural characteristics of the non-oxidized and oxidized activated carbon cloth are shown in Table 1. It can be

observed that the acid pretreatment with  $HNO_3$  decreased the specific surface area (SSA) and porosity of the activated carbon cloth. This occurs because activation of carbon makes the pore walls thinner and, thus, more easily destroyable by the oxidizing agent [33]. However, the pore size distribution did not significantly change after the wet oxidation of ACC (Table 1). The effects of impregnation with Pd on the textural characteristic (SSA) of oxidized and non-oxidized ACC are shown in Fig. 4. These effects will be explained with the aid of SEM images in the following paragraphs.

The SEM images of the oxidized ACC without and with different Pd contents are presented in Fig. 5. The virgin oxidized ACC (Fig. 5a) almost looks like a flat fiber without any visible pores, cavities or bulk solid on the surface. This also agrees well with the results of the specific surface area and pore size distribution measurements (Table 1). It demonstrates that the ACC fibers contain mainly micropores with narrow size distribution between 8 to 10 nm which are invisible in the SEM image in Fig. 5a. The SEM image of oxidized ACC impregnated with 1 % Pd is almost the same as the virgin oxidized ACC. This observation demonstrates that almost all of the loaded Pd is located inside the micropores and, consequently, it is dispersed into very small sizes (less than the micropores size). Pd contents above 1 wt% lead to drastic morphology changes: large Pd particles on the outer surface of the ACC are clearly visible and presented in Fig. 5c–d for Pd loading of 3 and 5 %, respectively.

**Fig. 6** SEM images of non-oxidized ACC with different Pd contents: **a** virgin non-oxidized ACC, **b** impregnated with 1 wt% Pd, **c** impregnated with 3 wt% Pd, **d** impregnated with 5 wt% Pd



The deposition of the big Pd particles on the outer surface of the ACC fibers resulted in clogging of ACC micropores and this fact is in well agreement with specific surface area measurements (Fig. 4). In fact, increasing Pd content from 1 to 5 wt% decrease the specific surface area (from 1,580 to 1,409  $\text{m}^2/\text{g}$ ). While impregnation with 1 wt% Pd even leads to an small increase in specific surface area (from 1,520 to 1,580  $\text{m}^2/\text{g}$ ). Locating of small Pd

particles in the micropores can increase the roughness of the micropores' surface and consequently result in a small increase in micropores surface area.

Unlike oxidized ACC, impregnation of the non-oxidized ACC with Pd, even with low content of Pd, leads to form a very thin layer of small Pd particles on the outer surface of the ACC fibers (Fig. 6). The metallization of the outer surface of carbon fibers immersed in the acidic solution of

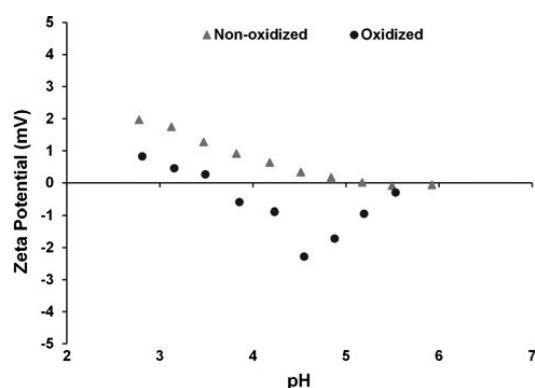


**Fig. 7** Isoelectric point measurements of oxidized and non-oxidized ACC

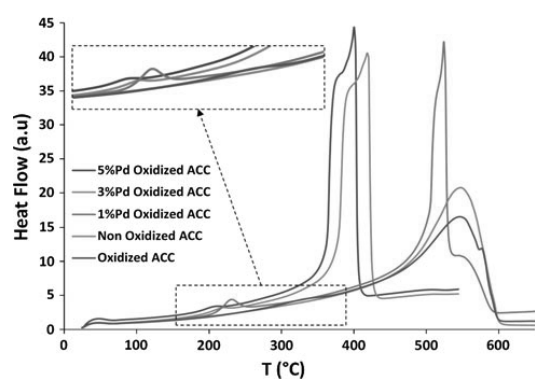


**Fig. 8** DTA curves for oxidized ACC and Pd/ACC systems in oxidative atmosphere

$\text{PdCl}_2$  can be even observed visually. The outer surface of the black ACC turned grey which is typical for palladium; while their interior, as seen upon cleavage of the fibers, remained black. Formation of the Pd particles and their crust-like distribution on the outer surface of the ACC fibers resulted in clogging of ACC micropores and this fact is well confirmed with specific surface area measurements (Fig. 4). In fact, impregnation with 1 % Pd results in a decrease in specific surface area (from 1,787 to 1,711  $\text{m}^2/\text{g}$ ). Increasing the amount of Pd content leads to bigger Pd particles and denser layer of Pd particles on the outer surface of the ACC fibers (Fig. 6c–d).

Simonov et al. [34] showed that ionic palladium ( $\text{Pd}^{2+}$ ) in acidic solution of palladium dichloride ( $\text{PdCl}_2$ ) appears mainly as tetrachloropalladic ion complex ( $\text{PdCl}_4^{2-}$ ). The pH of the Pd precursor during the impregnation of the ACC was in the range of 3.5–4. According to isoelectric point measurements (Fig. 7), the  $\text{pH}_{\text{IEP}}$  of the oxidized and non-oxidized ACC were 3.5 and 5 respectively. The surface

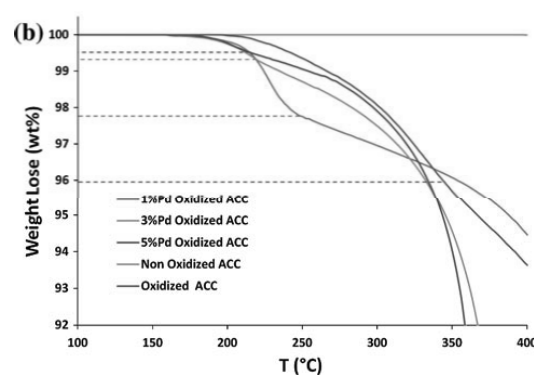
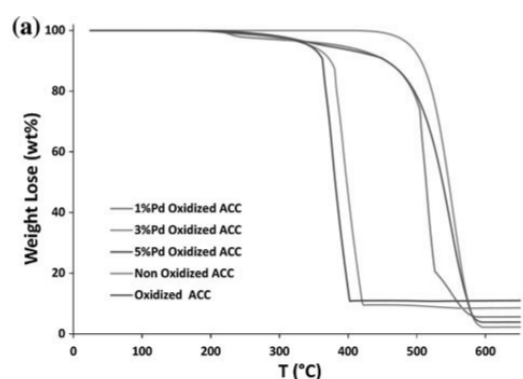


**Fig. 9** TGA a curves and corresponding close-up of the first exothermic effect b for oxidized ACC and Pd/ACC systems in oxidative atmosphere

morphology changes of the non-oxidized and oxidized ACC impregnated with Pd could be explained as follow:

- During the impregnation of non-oxidized ACC with Pd precursor, the pH of the precursor is considerably less than  $\text{pH}_{\text{IEP}}$  of the surface of the ACC. So, the electrostatic attraction between the positively charged surface ( $\text{pH} < \text{pH}_{\text{IEP}}$ ) and the catalyst precursor anions ( $\text{PdCl}_4^{2-}$ ) facilitate the adsorption of Pd anions ( $\text{PdCl}_4^{2-}$ ) on the surface of the ACC fibers. Because the outer surface of the fibers is directly exposed to the Pd precursor, the adsorption of ( $\text{PdCl}_4^{2-}$ ) occurs rapidly and leads to formation of the crust-like distribution of the Pd particles on the outer surface. It can be observed visually that the pale yellow color of the precursor disappears after a short contact of non-oxidized ACC with precursor. Indeed, the adsorption equilibrium was found to be established in ca. 20 min on the non-oxidized ACC and in about 3 h on the oxidized one.
- Since carbon is essentially not hydrophilic in nature, it has a very low affinity for solvents of polar character

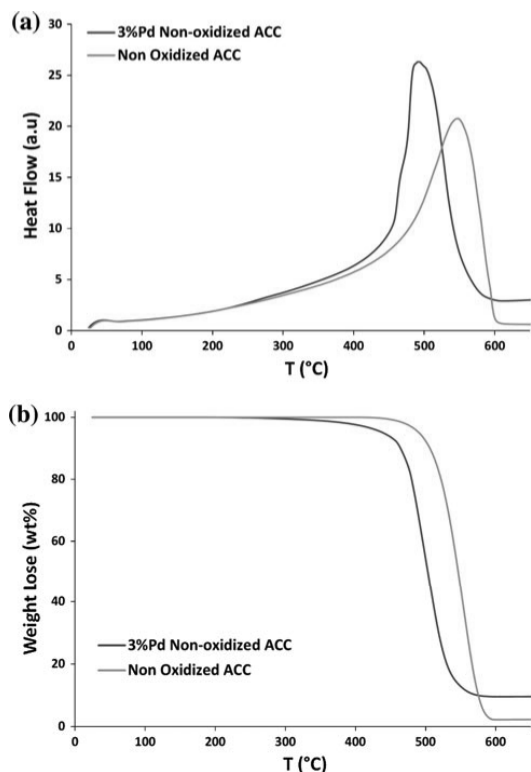


**Fig. 10** DTA (a) and TGA (b) curves for non-oxidized ACC and 3 wt% Pd/ACC in oxidative atmosphere

**Table 2** The characteristic temperatures in DTA/TGA curves

Sample	$T_c$ (°C)	$T_g$ (°C)	Burn-off (°C)
Non-oxidized ACC		455–465	495–595
3 % Pd/Non-oxidized ACC		300–320	460–580
Oxidized ACC	310–320	400–415	495–585
1 % Pd/Oxidized ACC	215–220	355–370	500–580
3 % Pd/Oxidized ACC	200–205	290–300	380–420
5 % Pd/Oxidized ACC	195–200	275–285	360–405

$T_c$  the temperature at which oxygen starts to attack the ACC oxygen surface functional groups,  $T_g$  the temperature at which oxygen starts to attack the carbon fiber skeleton,  $T_{burn-off}$  the burn-off temperature of the ACC

such as water [35]. The metal precursor will be mostly exposed to the outer surface of the carbon particle when using water, but it will penetrate to the interior pores when the hydrophobicity of carbon decreases. Acidic functional groups introduced by the treatment with  $\text{HNO}_3$  decreases the hydrophobicity of the carbon [4] thus making the interior of the micropores more accessible to the aqueous solution of the metal

**Table 3** Weight loss corresponding to the decomposition of the oxygen surface functional groups

Sample	Weight loss (wt%)
Oxidized ACC	4.12
1 % Pd/oxidized ACC	2.32
3 % Pd/oxidized ACC	0.71
5 % Pd/oxidized ACC	0.41

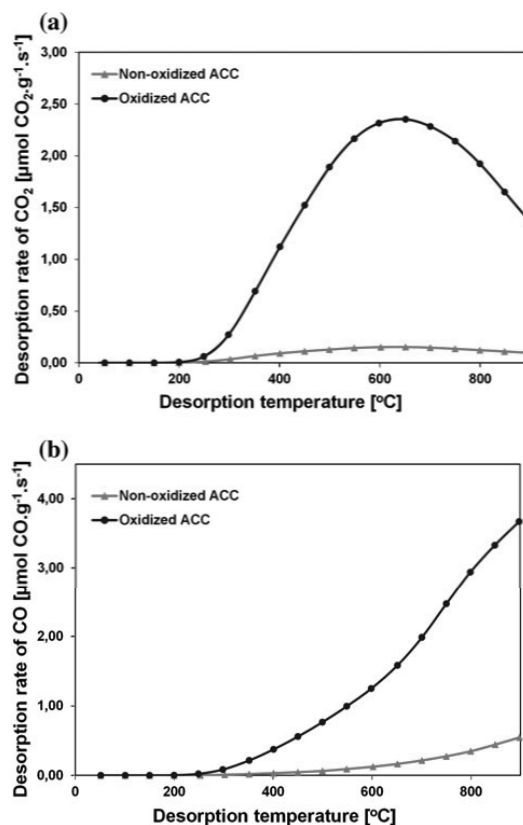


**Fig. 11** The  $\text{CO}_2$  (a), and  $\text{CO}$  (b) temperature programmed desorption profiles of the non-oxidized and oxidized of ACC

precursor during impregnation. Indeed, acid pretreatment of the ACC facilitates the access to the interior surfaces of the ACC fibers. Therefore, it could lead to deposition of Pd particles during the impregnation in the interior surface area.

### 5.1.2 Thermal analysis

DTA and TGA profiles of virgin ACC (non-oxidized and oxidized) and impregnated ones with different Pd contents

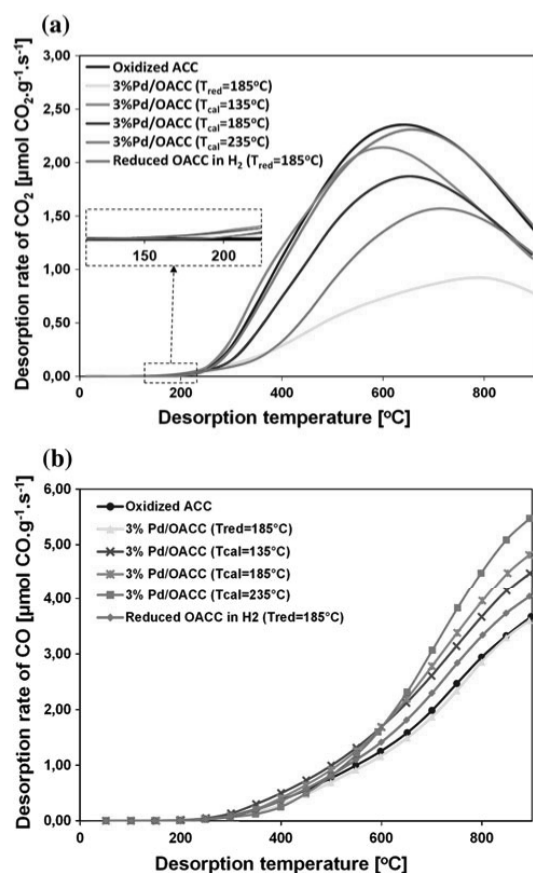


**Fig. 12** The CO<sub>2</sub> (a), and CO (b) temperature programmed desorption profiles of the oxidized ACC and Pd catalysts on oxidized of ACC

are presented in Figs. 8, 9 and 10. No thermoeffect was detected by DTA for non-oxidized ACC below 455 °C. The only exothermic effect starts at 455–465 °C followed by a large and sharp weight loss in the TGA curve (Fig. 10). This effect corresponds to the burn-off of the ACC fibers and,  $T_g$  is the temperature at which the burn-off of the ACC fibers starts.

The DTA thermogram for oxidized ACC includes two exothermic effects. The first starts at around 310–320 °C and shows a peak at 350 °C with a small weight loss (about 4 %) in the corresponding TGA profile (Fig. 9b; Table 3). The burn-off of the ACC fibers starts at 400–415 °C and is followed by a drastic and sharp weight loss in the TGA profile (Fig. 9a). The first slight observed peak corresponds to the decomposition of the oxygen-containing surface functional groups to CO and CO<sub>2</sub> [32].  $T_c$  is the temperature at which the first thermoeffect starts.

**Table 4** Total amount of CO and CO<sub>2</sub> desorbed according to temperature programmed desorption curves

Sample	CO (μmol/g)	CO <sub>2</sub> (μmol/g)
Non-oxidized ACC	130.13	91.73
Oxidized ACC (OACC)	1,137.82	1,296.30
Reduced OACC with H <sub>2</sub> ( $T_{red} = 185$ °C)	1,206.19	1,224.44
3 % Pd/OACC ( $T_{red} = 185$ °C)	1,050.86	470.43
3 % Pd/OACC ( $T_{cal} = 135$ °C)	1,369.89	1,135.57
3 % Pd/OACC ( $T_{cal} = 185$ °C)	1,392.24	943.12
3 % Pd/OACC ( $T_{cal} = 235$ °C)	1,492.78	734.22

For Pd catalysts on oxidized ACC the following observations can be made:

- $T_c$  was shifted to lower values and it was dependent on the Pd content (Table 2; Fig. 9b). The reduction rate in  $T_c$  value for impregnated ACC, at the beginning was very sharp and  $T_c$  was reduced to 215–220 °C for 1 % Pd/ACC (Table 2). After that, the rate of change of  $T_c$  as a function of Pd content was decreased.  $T_c$  is an important criterion in selection of calcination temperatures for Pd catalysts on oxidized ACC. In fact, treating of the catalysts above their  $T_c$  temperatures could damage and finally destroy the oxygen-containing surface functional groups which were introduced by acid pretreatment of ACC.
- The maximum weight loss by the decomposition of the oxygen-containing surface functional groups (4.12 wt%) belongs to virgin oxidized ACC (Table 3). Impregnating oxidized ACC with Pd, reduced the bare surface of the ACC fibers for the first exothermic effect. This diminished the weight loss values because of the decomposition of the oxygen surface functional groups (Table 3).
- In the same way as  $T_c$  values,  $T_g$  for the impregnated ACC with Pd were considerably decreased (Table 2). The value of reduction in  $T_g$  also depended on the Pd content.
- Impregnating the oxidized ACC with Pd leads to the sharper and more intensive exothermic peaks and weight loss corresponding to burn-off of the ACC fibers.

The DTA curve of impregnated non-oxidized ACC with 3 % Pd, the same as the virgin non-oxidized ACC, showed no peak corresponding to the decomposition of oxygen surface functional groups (Fig. 10). But, burn of the ACC fibers were started earlier ( $T_g = 300$ – $320$  °C) in 3 % Pd/ACC compare to the virgin non-oxidized ACC (Table 2).

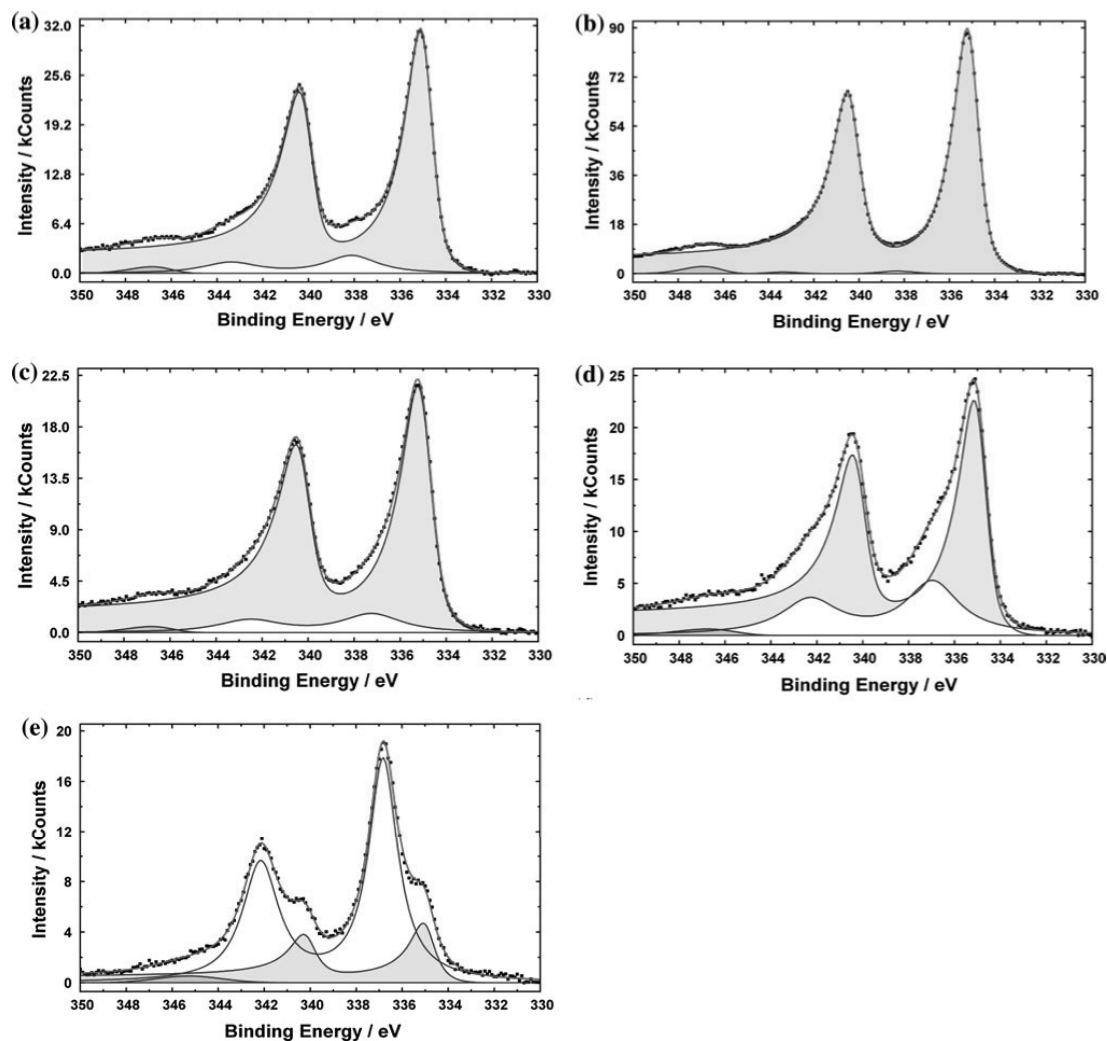


**Fig. 13** The Pd3d XPS spectra of 3 wt% Pd/OACC **a** fresh virgin dried one, **b** reduced one with H<sub>2</sub> at 185 °C and the calcined ones in the air at **c** 135 °C, **d** 185 °C, **e** 235 °C

### 5.1.3 Surface chemistry of the support materials

Wet oxidation treatments of carbon materials result in the formation of different oxygen-containing surface groups. These functional groups consist of strong acidic ones (like carboxylic and anhydride groups) and weak acidic ones (like lactones, phenols and carbonyl groups) [5, 36]. These surface functional groups can be characterized by TPD desorption tests [33]. The stronger acidic groups lead to desorption of CO<sub>2</sub> at lower temperatures, while the weaker acidic ones show desorption zone of CO at higher

temperatures [5, 29, 33]. The CO- and CO<sub>2</sub>-TPD profiles of the non-oxidized and oxidized activated carbon cloths are shown in Fig. 11. The CO<sub>2</sub>-TPD profile of the oxidized ACC shows a wide peak which starts at approximately 180 °C and reaches a maximum at approximately 620 °C. The corresponding CO-TPD profile begins to release CO at higher temperature (220 °C) and continuing this with increasing flow rate up to 900 °C. Indeed, it implies that the pretreatment of the ACC with HNO<sub>3</sub> introduces considerable amounts of oxygen containing functional groups on the surface of ACC fibers.

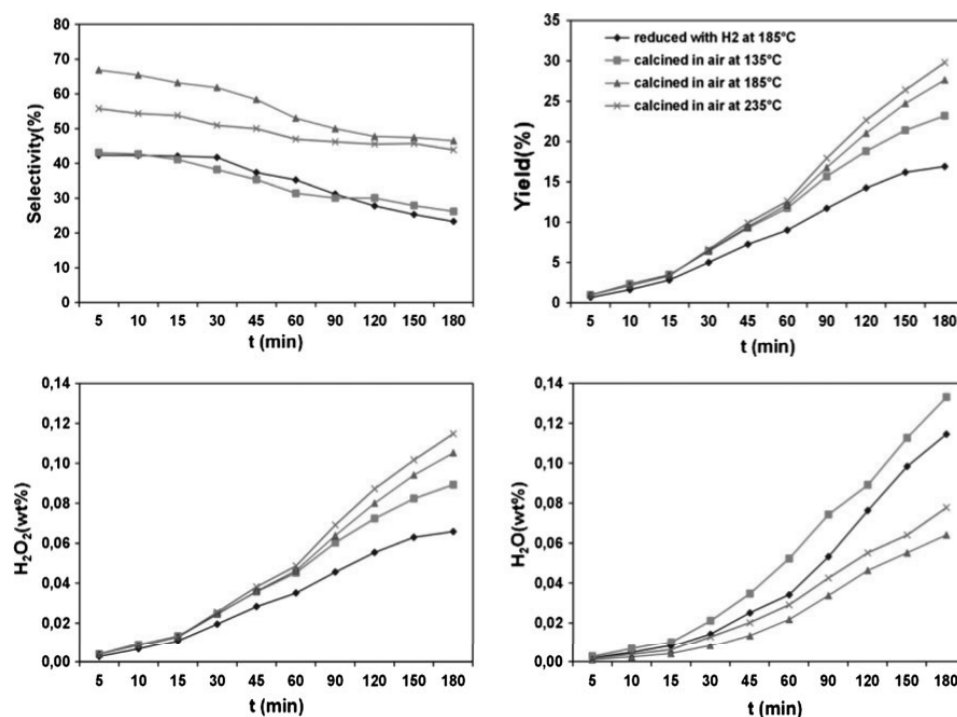


**Fig. 14** Performance of 3 % Pd catalysts on oxidized ACC (mass of catalyst = 55 mg, temperature = 0 °C)

The CO<sub>2</sub>- and CO-TPD profiles of the oxidized ACC (virgin oxidized ACC and the one reduced with H<sub>2</sub> at 185 °C) and the corresponding 3 wt% Pd catalysts are presented in Fig. 12. On the basis of them the following observations can be made:

- The CO<sub>2</sub>-TPD profiles of the different 3 wt% Pd catalysts started to release CO<sub>2</sub> at around 150 °C while in virgin oxidized ACC it started at around 200 °C.
- Increasing the calcination temperature reduced the amount of the released CO<sub>2</sub> represented by the area under the CO<sub>2</sub> curve (Table 4). In other words, calcination of the Pd catalyst in the air resulted in decomposition of the stronger acidic surface functional groups. This agrees well with the DTA/TGA results (Sect. 5.1.3).
- Minimum amount of the released CO<sub>2</sub> belongs to the reduced Pd supported catalyst in H<sub>2</sub> at 185 °C. While the same treatment of the virgin oxidized ACC did not change the CO<sub>2</sub>-TPD profile considerably (Table 4).
- Considering the CO<sub>2</sub>- and CO-TPD profiles of Pd supported catalyst implies that the calcination of Pd catalysts in the air led to decomposition of the stronger acidic surface groups in the way which increased the thermal CO release (Table 4).

#### 5.1.4 Metal Phase

The metal phase of Pd catalysts on oxidized ACC (the fresh dried catalyst, the one reduced with H<sub>2</sub> and the calcined ones) were characterized by the X-ray photoelectron spectroscopy (XPS). The Pd3d XPS spectra of the different 3 wt% Pd catalysts are displayed Fig. 13. The XPS spectrum of the catalyst reduced with H<sub>2</sub> at 185 °C (Fig. 13b) shows two peaks with binding energy at around 340.5 and 335.3 eV, corresponding to zerovalence of Pd (Pd<sup>0</sup>) in the 3d<sub>3/2</sub> and 3d<sub>5/2</sub> level [37]. It indicates that the Pd species in the reduced catalyst appear in metallic state. From the segregation of the Pd3d XPS spectra of the catalysts which were calcined at 135, 185, and 235 °C (Fig. 13c, d, e), two doubles were obtained: one at a lower binding energy, which can be assigned to metallic palladium (Pd<sup>0</sup>), and a second one at a higher binding energy, corresponding to Palladium oxide (PdO). The calcined Pd/OACC catalysts showed the presence of a PdO phase as well as a metallic phase (Pd<sup>0</sup>), which indicated a partial oxidation of the Pd particles with calcination in static air. As it can be observed, with increasing the calcination temperature the amount of palladium oxide (PdO) is also increased. The catalyst which was calcined at

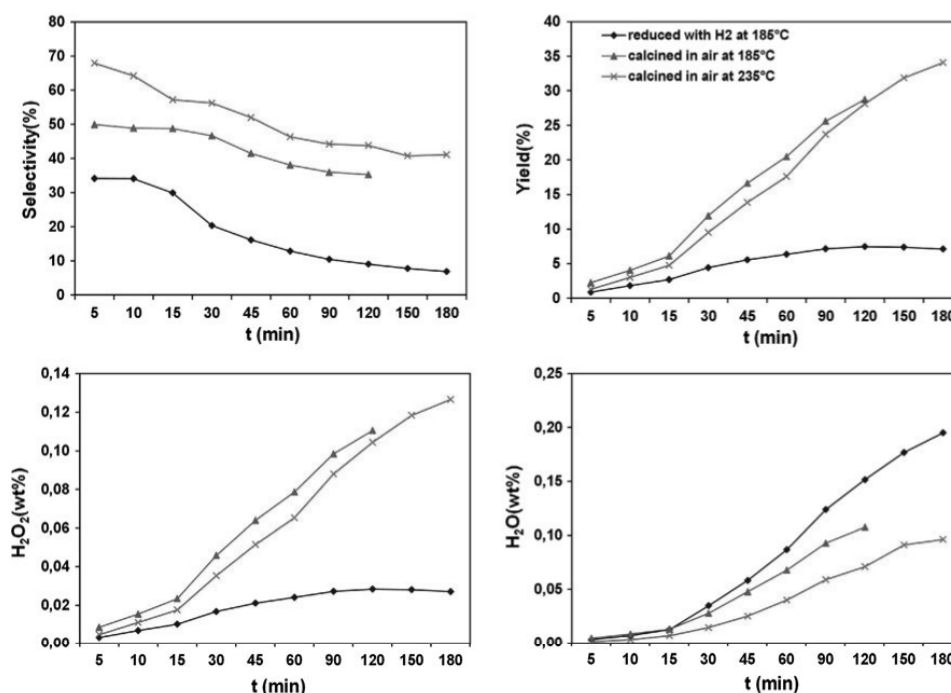


Fig. 15 Performance of 3 wt% Pd on non-oxidized ACC (mass of catalyst = 55 mg, temperature = 0 °C)

235 °C contained the maximum amount of palladium oxide (around 72.1 wt% of total metal phase).

The Pd3d XPS spectrum of the fresh virgin catalyst shows palladium mostly in the metallic form (Pd<sup>0</sup>) instead of Pd<sup>2+</sup>. The appearance of Pd<sup>0</sup> species in the virgin and oxidized catalysts could be due to a reducing effect of the activated carbon fibers during the impregnation step, because of the native charge of their surfaces (Fig. 7).

## 5.2 Catalytic activity

Activity of the catalysts was evaluated by yield and selectivity. These two parameters are defined as:

$$\text{Yield (\%)} = \frac{\text{Moles of produced H}_2\text{O}_2}{\text{Moles of H}_2 \text{ fed}} \times 100$$

$$\text{Selectivity (\%)} = \frac{\text{Moles of produced H}_2\text{O}_2}{\text{Moles of consumed H}_2} \times 100$$

The results of the direct synthesis of hydrogen peroxide over 3 wt% Pd catalysts on oxidized and non-oxidized ACC are shown in Figs. 14 and 15, respectively. From them, the following observations can be made:

a) The calcined catalysts are more active and selective than the corresponding reduced catalysts.

- b) In the case of catalysts on non-oxidized ACC, increasing the calcination temperature improves the selectivity. These (a,b) imply that the oxidized state of Pd (PdO) in the catalyst makes the catalyst more active and selective than the corresponding Pd<sup>0</sup> catalyst.
- c) In the case of catalysts on oxidized ACC, increasing the calcination temperature up to 185 °C improves both the activity and selectivity. Increasing the calcination temperature from 185 to 235 °C leads to slightly more active but less selective catalyst.
- d) Pd catalysts on oxidized ACC are significantly more selective than the corresponding Pd catalysts on non-oxidized ACC, except the calcined catalysts at 235 °C. This observation implies that oxygen containing surface functional groups make the Pd catalyst more selective in the direct synthesis of H<sub>2</sub>O<sub>2</sub>.

Heat treatment of oxidized ACC in the presence of Pd at temperatures higher than 190 °C can seriously damage the oxygen-containing functional groups. Because of this, calcination at 185 °C led to better selectivity than at 235 °C. This was the case even though the amount of palladium oxide (PdO) was higher in the catalyst calcined at 235 °C.

Heat treatment of oxidized ACC in H<sub>2</sub> causes the substantial damage to the oxygen-containing functional groups (Figs. 11, 12). On the other hand, there is no palladium in the form of palladium oxide in the reduced Pd catalysts. Lack of PdO and damaged oxygen-containing functional groups result in poor performance of the reduced catalysts.

## 6 Conclusions

According to the observations and discussion, it can be concluded that activity and selectivity of the Pd catalysts on ACC in direct synthesis of H<sub>2</sub>O<sub>2</sub> are greatly affected by two important characteristics of the catalyst: 1) oxidation state of Pd in metallic phase; 2) surface chemistry of the support which is determined by the nature and the amount of surface functional groups.

The existence of the oxidized state of Pd (PdO) makes the catalyst more active and selective than the corresponding zerovalent Pd<sup>0</sup> catalysts. PdO affected on selectivity by increasing the rate of H<sub>2</sub>O<sub>2</sub> production and reducing the rate of water production, simultaneously.

Pd catalysts on oxidized ACC were significantly more selective than the corresponding ones on non-oxidized ACC. This implies that oxygen containing surface functional groups make the Pd catalyst more selective. Reduction of Pd catalysts supported on the oxidized ACC with H<sub>2</sub> at 185 °C substantially damaged the oxygen-containing functional groups. Moreover, calcination with the air at temperatures higher than 190 °C could also damage oxygen-containing functional groups.

**Acknowledgments** The authors thank Dr. Kari Eranen for helping with the TPD and SSA measurements and Toni Väkiparta for SEM images.

## References

- Baukal CE (1998) Oxygen-enhanced combustion. CRC, New York
- Solsona BE, Edwards JK, Landon P, Carley AF, Herzing A, Kiely CJ, Hutchings GJ (2006) Chem Mater 18:2689
- Harada T, Ikeda S, Miyazaki M, Sakata T, Mori H, Matsumura M (2007) J Mol Catal A 268:59
- de Miguel SR, Vilella JI, Jablonski EL, Scelza OA, Salinas-Martínez de Lecea C, Linares-Solano A (2002) Appl Catal A 232:237
- Edwards JK, Hutchings GJ (2008) Angew Chem Int Ed 47:9192
- Choudhary VR, Jana P, Bhargava SK (2008) Catal Lett 125:296
- Gaikwad AG, Sansare SD, Choudhary VR (2002) J Mol Catal A 181:143
- Choudhary VR, Gaikwad AG, Sansare SD (2002) Catal Lett 83:235
- Choudhary VR, Sansare SD, Gaikwad AG (2002) Catal Lett 84:81
- Krishnan VV, Dokoutchaev AG, Thompson ME (2000) J Catal 196:366
- Dissanayake DP, Lunsford JH (2003) J Catal 214:113
- Burch R, Ellis PR (2003) Appl Catal B 42:203
- Fu L, Chuang KT, Fiedorow R (1992) Stud Surf Sci Catal 72:33
- Abate S, Centi G, Melada S, Perathoner S, Pinna F, Strukul G (2005) Catal Today 104:323
- Melada S, Pinna F, Strukul G, Perathoner S, Centi G (2005) J Catal 235:241
- Melada S, Pinna F, Strukul G, Perathoner S, Centi G (2006) J Catal 237:213
- Pospelova TA, Kobozev NI, Eremin EN (1961) J Phys Chem 35:143
- Pospelova TA, Kobozev NI (1961) J Phys Chem 35:262
- Fu F, Chuang KT, Fiedorow R (1992) Stud Surf Sci Catal 72:33
- Reis KP, Joshi VK, Thompson ME (1996) J Catal 161:62
- Dissanayake DP, Lunsford JH (2002) J Catal 206:173
- Chinta S, Lunsford JH (2004) J Catal 225:249
- Han Y-F, Lunsford JH (2005) J Catal 230:313
- Han Y-F, Lunsford JH (2005) Catal Lett 99:13
- Liu Q, Lunsford JH (2006) J Catal 239:237
- Liu Q, Lunsford JH (2006) Appl Catal A 314:94
- Ratchanansorn W, Simonov D, Gudarzi D, Kolehmainen E, Turunen I (2011) Chem Eng Process 50:1186
- Radkevich VZ, Senko TL, Wilson K, Grishenko LM, Zaderko AN, Diyuk VY (2008) Appl Catal A 335:241
- Toebe ML, van Dillen JA, de Jong KP (2001) J Mol Catal A 173:75
- Gudarzi D, Simakova OA, Hernández Carucci JR, Biasi PD, Eränen K, Kolehmainen E, Turunen I, Murzin DY, Salmi T (2010) Chem Eng Tran 21:925
- Shen W, Li Z, Liu Y (2008) Recent Patent Chem Eng 1:27
- Melada S, Pinna F, Strukul G, Perathoner S, Centi G (2006) J Catal 237:213
- Moreno-Castilla C, López-Ramón MV, Carrasco-Marin F (2000) Carbon 38:1995
- Simonov PA, Romanenko AV, Prosvirin IP, Moroz EM, Boronin AI, Chuvilin AL, Likhobolov VA (1997) Carbon 35(1):73
- Rodríguez-Reinoso F (1998) Carbon 36(3):159
- Lee KY, Na JE, Lee JY, Kim JN (2004) Bull Korean Chem Soc 125, Nr.8:1280
- Wang H, Wan Y (2009) J Mater Sci 44:6553



## **Publication V**

Ratchanausorn, W., Gudarzi, D., Turunen, I.

Catalytic direct synthesis of hydrogen peroxide in a novel microstructured reactor

*Submitted to Chemical Engineering and Processing: Process Intensification.*



## Catalytic direct synthesis of hydrogen peroxide in a novel microstructured reactor

Warin Ratchananusorn\*, Davood Gudarzi, Ilkka Turunen

*Department of Chemical Technology, Lappeenranta University of Technology,  
Lappeenranta, FI-53851 Finland*

\* Corresponding author. E-mail: [warin.ratchananusorn@lut.fi](mailto:warin.ratchananusorn@lut.fi); Tel: +358 40 4804963;

### Abstract

The direct synthesis of hydrogen peroxide was investigated in a bench-scale continuous process using a novel microstructured reactor. This plate-type reactor was developed to offer favorable hydrodynamic and mass transfer conditions. Supported Pd catalyst on activated carbon cloths was employed. The experiments were conducted with hydrogen and oxygen using methanol as a solvent. Effects of process conditions, e.g. gas composition, gas and liquid flow rates, pressure and amount and composition of catalyst were studied. The promising results and plans for further development of the reactor and process concept are discussed.

Keywords: microreactor, hydrogen peroxide, direct synthesis, Pd catalyst

### 1. Introduction

Hydrogen peroxide is a very powerful and green oxidant used in many industries. Currently, hydrogen peroxide is mainly produced by auto-oxidation in anthraquinone process. This process, however, has certain drawbacks. The chemistry is complicated with plenty of side reactions and byproducts. The investment costs are relatively high because of high number of equipment and large capacity is needed to achieve acceptable profitability. Moreover, using of a large amount of organic solvent makes the process less sustainable [1-2].

Direct synthesis of hydrogen peroxide has been studied as an attractive, green alternative over past decades [3]. The main benefits include:

- The chemistry is more straightforward than in the case of anthraquinone process.
- Lower investment and operating costs due to a substantially smaller number of equipment.
- The process is green when compared to anthraquinone process. This is clear if water is used as a solvent. The direct synthesis is greener even with methanol as a solvent because the total volume of organic liquid in the process would be substantially less.
- The process is favorable for on-site production.

However, there are a number of technical challenges in the direct synthesis. Hydrogen and oxygen generate an explosive mixture at wide range of concentrations (5-96 vol% H<sub>2</sub>) [4]. Moreover, several side reactions are involved, as shown in Fig. 1. Therefore, selectivity is a challenge.

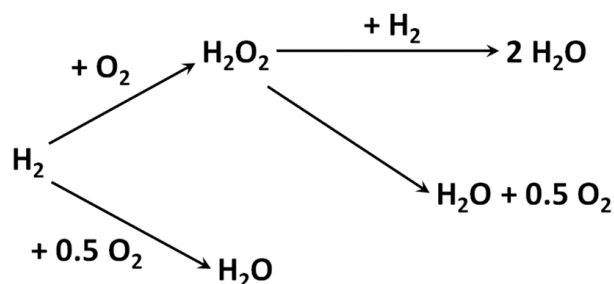


**Fig. 1.** Reactions in the direct synthesis of  $\text{H}_2\text{O}_2$ .

The safety risk can be decreased by utilizing microreactor technology. Proceeding of explosion could be suppressed by small dimensions of the reaction space. Moreover, the small holdup in microreactor limits the damage to be small even in the case of explosion. Therefore microreactors can be considered as inherently safe tools for hydrogen peroxide synthesis. Microreactors might even be able to be operated at explosive regime of gas mixture [5-8] allowing then also higher gas concentrations in the solvent, leading to higher yield.

The selectivity problem (see Fig. 1) can be solved by catalyst development [9]. Catalyst is very crucial to obtain high yield and selectivity, which tend to be rather low. Supported Pd catalysts, such as Pd/C, Pd/SiO<sub>2</sub>, and Pd/Al<sub>2</sub>O<sub>3</sub>, are traditionally used in the direct synthesis [3]. In recent years, bimetallic Au-Pd catalysts were found to exhibit high activity with high selectivity [10-12].

The direct synthesis has been studied in various types of reactors from conventional ones to microreactors. A number of investigations in batch reactors [9, 13-17] and trickle bed reactors has been carried out [12, 18-19]. Pd catalysts on various support materials including activated carbon [9, 12-15, 17], SiO<sub>2</sub>, CeS, and ZrO<sub>2</sub> [19] have been used. Many attempts to use single channel and multi-channel microreactors have been done [5-8, 11, 20-21]. Some of the experiments were done in the explosive regime [5-8] and sometimes small explosions were detected by Inoue, et al. [7].

The goal of this study is to investigate the direct synthesis in a novel microstructured reactor which was developed in previous studies [22]. Pd supported catalysts on activated carbon cloths [9] were used. Effects of gas composition, pressure, catalyst, and hydrodynamic conditions were studied.

## 2. Experimental setup

### 2.1 Microreactor

The development of the plate type microstructured reactor used in this study has been reported by Ratchananusorn et al. [22] and Semyonov et al. [23]. This structure was chosen because of several benefits. Firstly, gas-liquid mass transfer might be faster than in the reactor with parallel microchannels. The reason is that the gas slugs in the channels are surrounded by thin liquid films which easily become saturated with gas. In that case, mass transfer can only take place through the ends of the slugs [24], i.e. through reduced interfacial area. Moreover, the reactor can be easily opened for cleaning and catalyst replacement or regeneration. The plugging problem is also expected to be less severe when compared to

conventional microreactors with several microchannels. The safety is enhanced by small dimensions and holdup. Moreover, the scale up of this type of microreactor is straightforward. Several parallel plates can be installed (numbering up).

The configuration of the reactor is shown in Fig. 2. It is made of stainless steel and consists of several sections. The reactor plate is installed in vertical position. The inlets for gas and liquid feeds are located at the top section. Bifurcation configuration was used for the liquid feed to improve the distribution and prevent channeling problem. The gas feed takes place through the cover plate which is installed against the microreactor plate. The microstructure section is located below the inlet section. The width of this section is 32 mm, height 300 mm and depth 300  $\mu\text{m}$ . The microstructure consists of number of triangular elements (see Fig.2). The size of each element is 1 mm  $\times$  2 mm  $\times$  300  $\mu\text{m}$  (base  $\times$  height  $\times$  depth). The elements are arranged in staggered arrays providing void fraction of 75 % for reaction space. The holdup for gas/liquid mixture was 3.84  $\text{cm}^3$ . The microstructure was designed to improve the mixing of the two phases and to generate high interfacial area. Below the microstructure section is the catalyst bed. Pd catalyst was supported on active carbon cloth. A single layer of the cloth was installed in the catalyst bed between the plates.

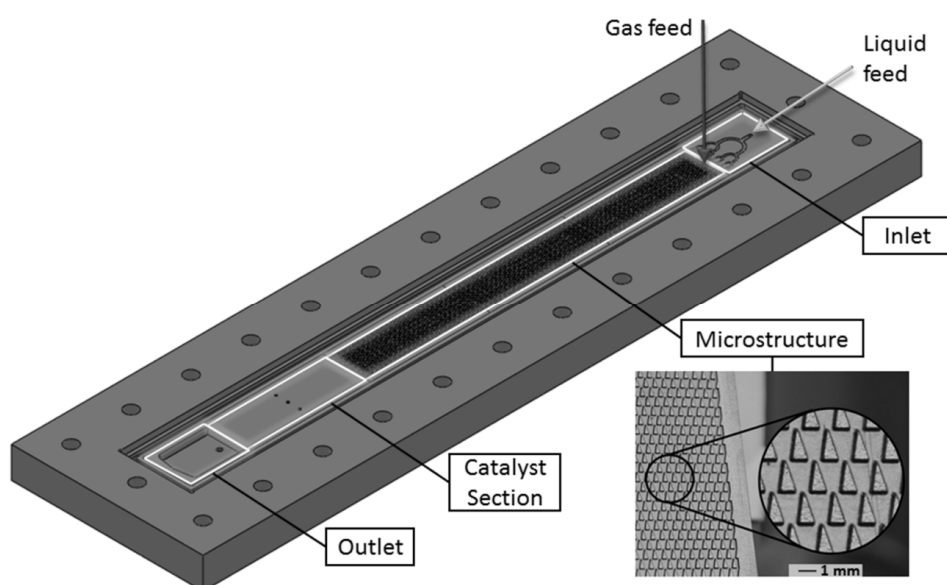


**Fig. 2.** Microreactor plate in this study.

## 2.2 Catalyst

### 2.2.1 Catalyst support

Carbon supported Pd catalysts have been extensively used in many studies for the direct synthesis with high performance [9, 12-15, 17]. Acidic pretreatment of the support and oxidized state of the catalyst usually give better performance [9]. Activated carbon has been found in many studies to give better performance than other supports.

In this study, Activated Carbon Cloth (ACC) was used as a catalyst support. Because ACC is a fabric-type support, it can be placed directly between the reaction plate and the cover plate.

Thus the replacement and regeneration of the catalyst can be done easily by opening the reactor and taking the ACC out. The packing problems are less difficult than with conventional granulated or powder catalysts.

Activated carbon cloth is flexible and easily applicable, it can be cut to proper size, bent, and rolled to fit into any reactor geometry. A large specific surface area is available (over 2000 m<sup>2</sup>/g). The diameter of fibers is small and uniform. Therefore, a good contact between the flowing fluid and the catalyst surface can be obtained and excellent mass transfer characteristics achieved [25].

The catalysts used in this study were developed and tested extensively in an autoclave batch reactor by Gudarzi et al. [9].

ACC is available from many manufacturers with different properties. In this study, ACC was purchased from Kynol GmbH, Germany, and the model number was ACC507-15. The specific surface area (BET) is as high as 1500 m<sup>2</sup>/g and the fiber size 9.2 μm. The microstructure of the fiber is uniform with straight pores rather than branched ones in granulated activated carbon.

### **2.2.2 Catalyst preparation**

Series of Pd/ACC catalysts were prepared by precipitation of Pd on ACC. The pretreatment of the support was done with 20 % nitric acid for overnight. Acidic solution of PdCl<sub>2</sub> was used to prepare the catalysts. The procedure has been described by Gudarzi et al. [9].

SEM images of catalysts with different Pd loading are shown in Fig. 3. The white spots represent metal particles which are well distributed throughout the ACC fibers. According to the images, Pd loading up to 1 wt.% mainly occurred inside the micropores of the ACC, because no particles can be detected on the outer surface of ACC. Increasing the amount of Pd led to development of large Pd particles on the outer surface [9].

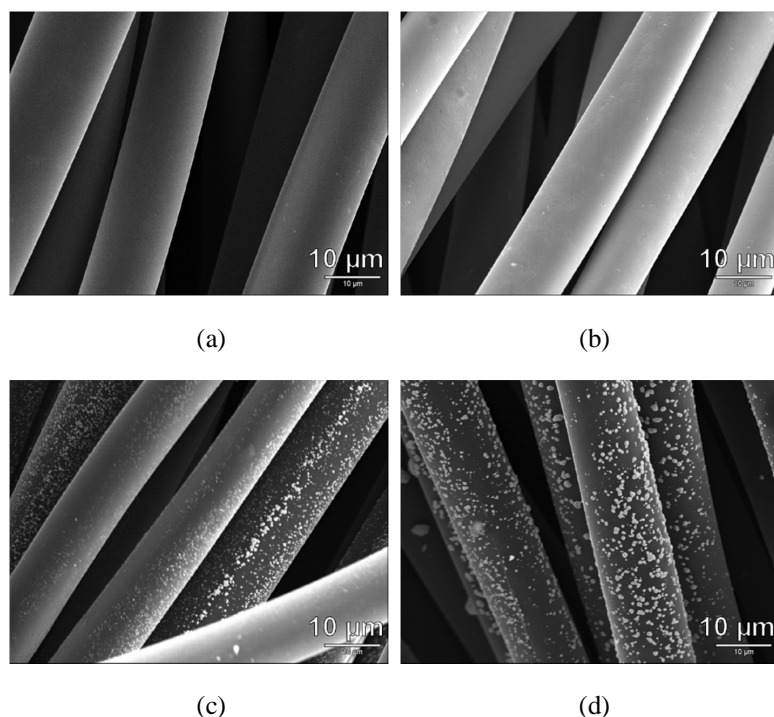


**Fig. 3.** SEM images for the catalysts used in this study; 0 wt.% (a), 1 wt.% (b) 3 wt.% (c), and 5 wt.% (d), reprinted with copyright from [9].

### 2.3 Experimental bench-scale process

A continuous bench scale process for the direct synthesis is shown in Fig. 4. The stainless steel equipment was initially passivated with 20% citric acid at 333.15 K for 12 h to minimize the decomposition of hydrogen peroxide. Methanol was used as a solvent allowing higher solubility of gases. Solvent was saturated with oxygen in a saturation vessel at 20 bar. Excess of oxygen gas was used in order to also strip away dissolved carbon dioxide and hydrogen left in the recycled solvent. The vessel was cooled to maintain solvent temperature at 273.15 K. From the saturation vessel, solvent with dissolved oxygen was fed into the microreactor together with mixture of CO<sub>2</sub> and H<sub>2</sub> (95%/5%). The fluids were flowing concurrently downwards in the reactor. At the bottom, gas and liquid phase were separated by gravity. Pressure was controlled by the gas outflow. Part of the outflowing liquid was taken as a product and the rest was recycled back to the saturation vessel. To maintain constant volume of liquid in the system, the equal amount of solvent was added to the saturation vessel as taken away as product stream after the reactor. The instrumentation is shown in Fig.4.

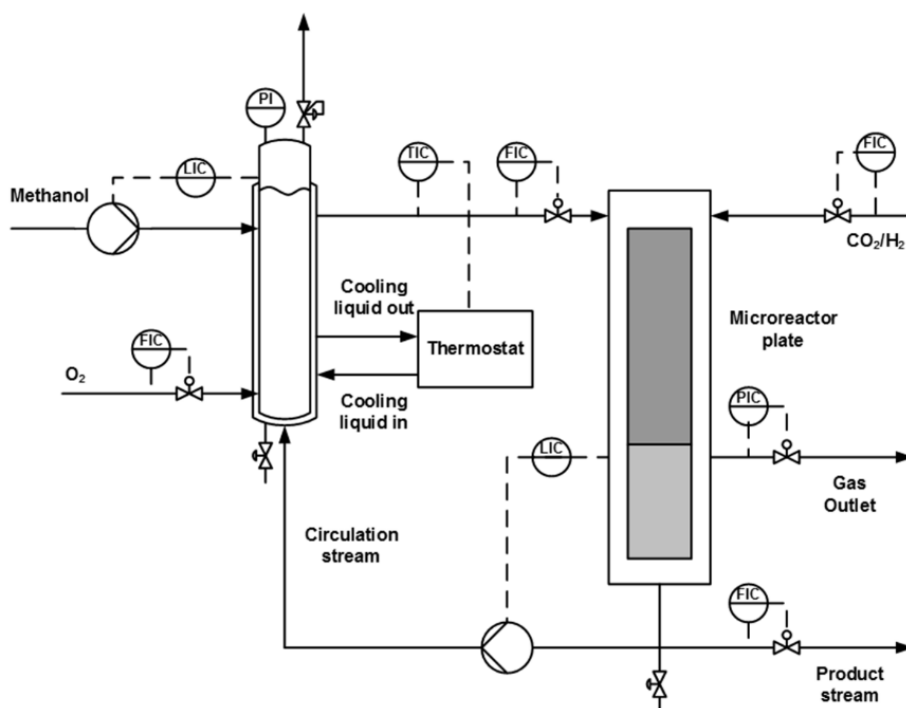


**Fig. 4.** Experimental setup.

### 3. Experimental procedure

Typical conditions in the reactor were 273.15 K and 20 bar. In the beginning, the saturation vessel was filled with methanol (0.35 l). Cooling of the liquid was started by feeding ethylene glycol through the jacket of the saturation vessel. Then oxygen flow through the saturation vessel was initiated. Gas sparger was utilized to achieve sufficient gas-liquid interface. After that, circulation of saturated solvent through the process was started. Next, the pressure of the reactor was raised to sufficient level by feeding inert gas. After reaching proper conditions in the whole process, the inert gas feed was changed to the mixture of CO<sub>2</sub> and H<sub>2</sub> and the reaction started.

The variables in the experiments were flow rate of liquid feed into the reactor, flow rate of gas feed into the reactor, pressure, concentration of Pd in the catalysts and amount of catalyst. In addition, two alternative inert gases, CO<sub>2</sub> and N<sub>2</sub>, were utilized to dilute hydrogen feed. Temperature was always the same, 273.15 K.

In each experiment, samples were taken from the product stream. Concentration of hydrogen peroxide and water was determined in each sample. The iodometric titration was used for hydrogen peroxide and Karl-Fischer titration for water. The selectivity was calculated according to Eq. 1.

$$selectivity (\%) = \frac{mol\ of\ produced\ H_2O_2}{mol\ of\ produced\ (H_2O_2 + H_2O)} \times 100\ \% \quad (1)$$

## 4. Experimental results

### 4.1 Long-term experiments

In these experiments, two different feed gas mixtures were used, as well as two pressure levels. The experimental conditions are shown in Table 1.

**Table 1**  
Conditions in long-term experiments.

No.	Liquid feed [ml/min]	Gas mixture	Gas feed [ml/min]	Product flow [ml/min]	Pressure [bar]	Catalyst	Amount of catalyst [g]
1	68	CO <sub>2</sub> /H <sub>2</sub>	102	0.85	20	3 wt.% Pd	0.21
2	68	N <sub>2</sub> /H <sub>2</sub>	102	0.85	20	3 wt.% Pd	0.21
3	68	CO <sub>2</sub> /H <sub>2</sub>	102	0.85	10	3 wt.% Pd	0.21

Analyzed concentration of H<sub>2</sub>O<sub>2</sub> in the products streams is shown in Fig. 5 as a function of time. It can be seen that the system reached steady state approximately in 20 h. The best results were obtained at higher pressure when carbon dioxide was used as inert gas. The likely explanation for the latter is that carbon dioxide increases the solubility of the gases [26] and stabilizes the produced hydrogen peroxide [27].

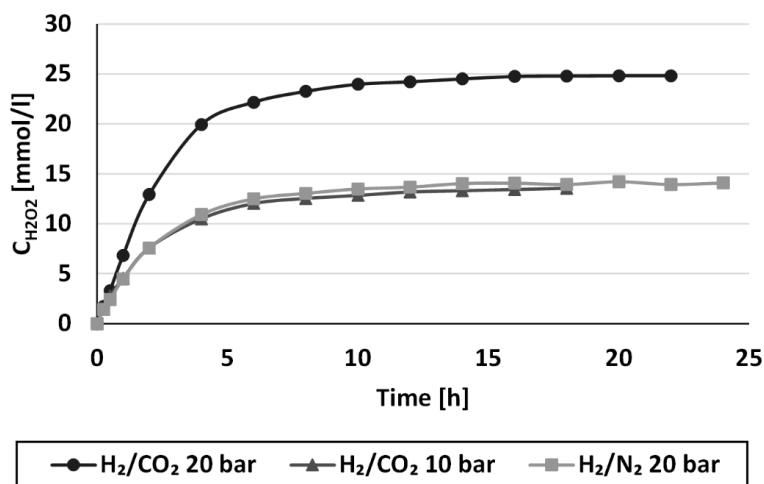


**Fig. 5.** Concentration of H<sub>2</sub>O<sub>2</sub> in long-term experiments.

The cumulative amount of H<sub>2</sub>O<sub>2</sub> produced (mmol) as a function of time is shown in Fig. 6. The upper curve represents the real cumulative H<sub>2</sub>O<sub>2</sub> production (mmol) and the lower one describes the cumulative H<sub>2</sub>O<sub>2</sub> (mmol) in the process circulation.

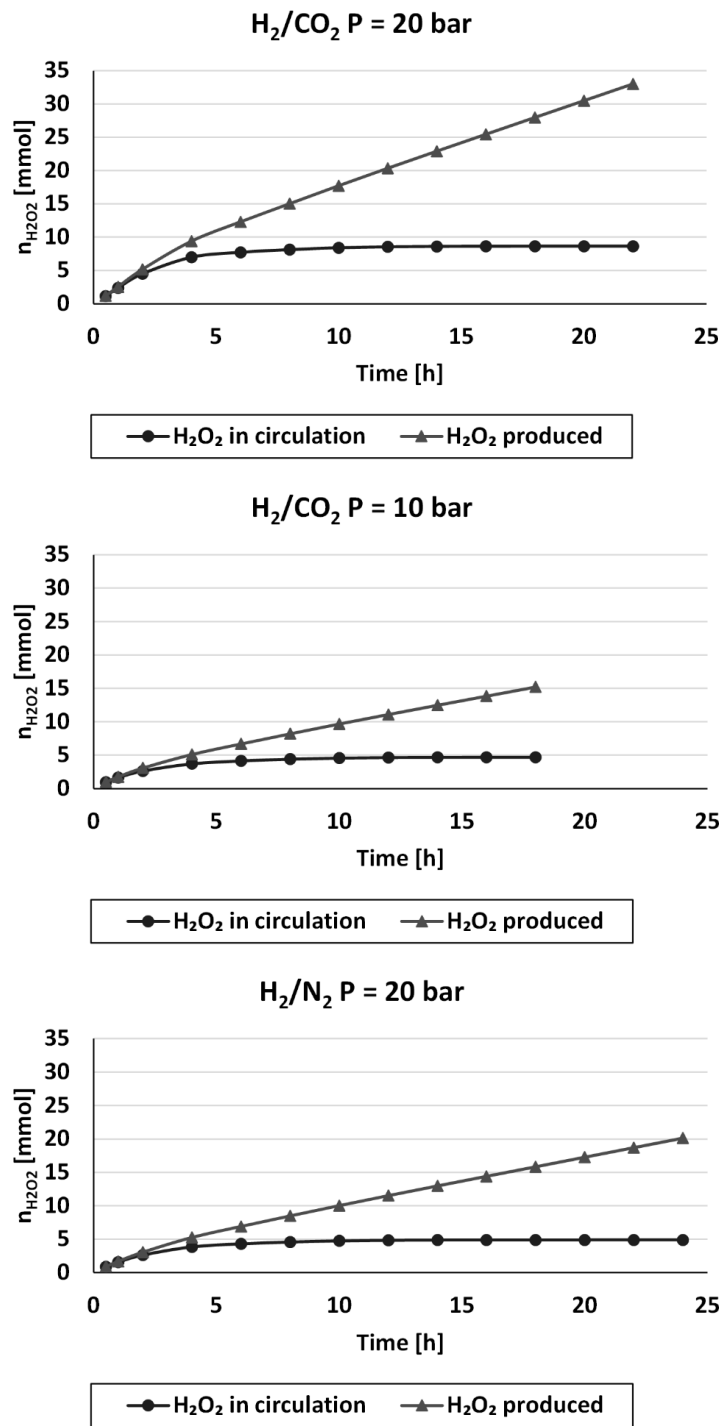


**Fig. 6.** Cumulative amount of H<sub>2</sub>O<sub>2</sub> produced.

The total production rate of  $\text{H}_2\text{O}_2$  in the reactor (mmol/h) is shown in Fig. 7. This is also shown per mass of Pd (mmol/h/g<sub>Pd</sub>).

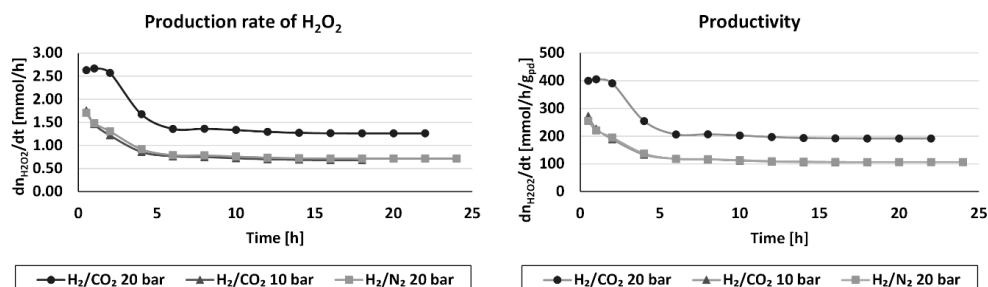


**Fig. 7.** Production rate of  $\text{H}_2\text{O}_2$  in the reactor.

Selectivity in the long-term experiments is shown in Fig. 8. It has the highest value at the beginning of the experiments, during the unsteady period. This is understandable because the decomposition of  $\text{H}_2\text{O}_2$  is directly proportional to the concentration of  $\text{H}_2\text{O}_2$ . The selectivity is the best at high pressure and with  $\text{CO}_2$  as inert gas instead of  $\text{N}_2$ . At higher pressure the rate of decomposition is lower because gas ( $\text{O}_2$ ) is produced during decomposition. As stated above,  $\text{CO}_2$  stabilizes  $\text{H}_2\text{O}_2$  and in that way improves selectivity.  $\text{CO}_2$  also improves the solubility of gases and, therefore, increases the production rate of hydrogen peroxide.

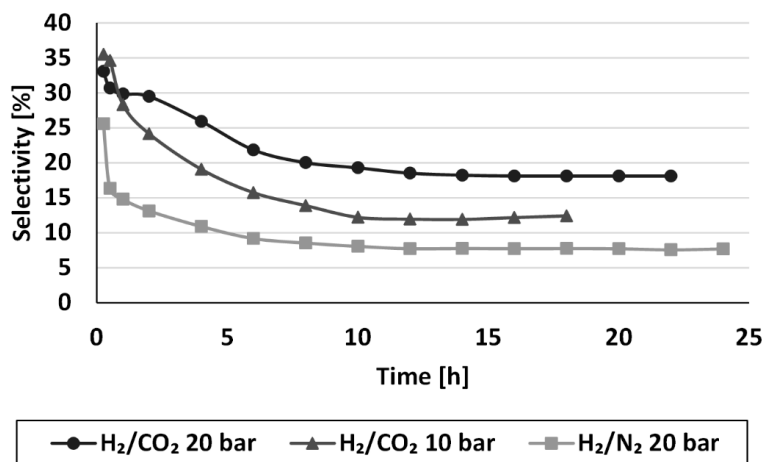


**Fig. 8.** Selectivity.

#### 4.2 Effect of the process conditions

Effect of different process conditions were studied with plenty of experiments with residence time of 6 hours. Temperature and pressure were the same in all the experiments, namely 273.15 K and 20 bar.

#### 4.2.1 Feed rate

Experiments were done with three different liquid feed rates. Gas/liquid ratio was kept constant in all these experiments. The conditions are shown in Table 2. Pressure was 20 bar, temperature 273.15 K and catalyst loading 0.21 g of 3 wt.% Pd. The product stream taken out after the reactor was 0.85 ml/min.

**Table 2**  
Experimental conditions for studies of liquid feed rate.

No.	Liquid feed rate [ml/min]	Gas feed rate [ml/min]
1	34	51
2	51	76.5
3	68	102

The results are shown in Fig. 9. Both concentration of  $H_2O_2$  and selectivity seem to increase as a function of liquid feed rate. A reason for this could be improved hydrodynamical conditions in the catalyst bed, causing better surface contact and liquid/solid mass transfer. Another explanation could be faster gas-liquid mass transfer in the microstructure section because of higher velocity of gas/liquid dispersion. However, the interfacial area was extremely high and therefore mass transfer is not limiting the total rate substantially in these experiments.

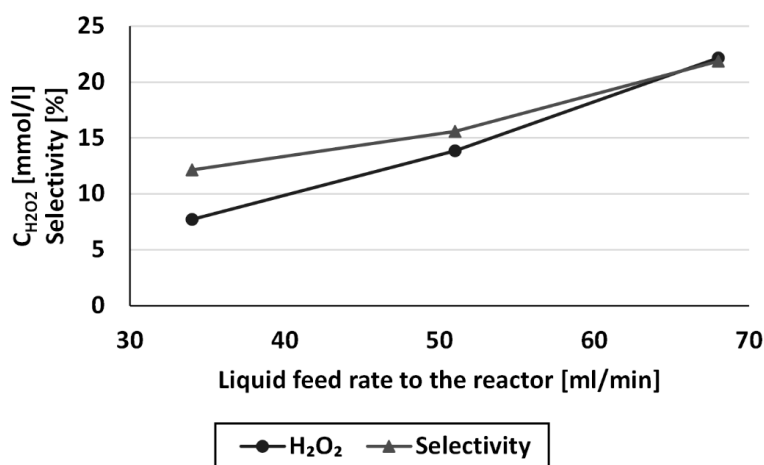


**Fig. 9.** Effect of liquid feed rate

#### 4.2.2 Gas/liquid feed ratio

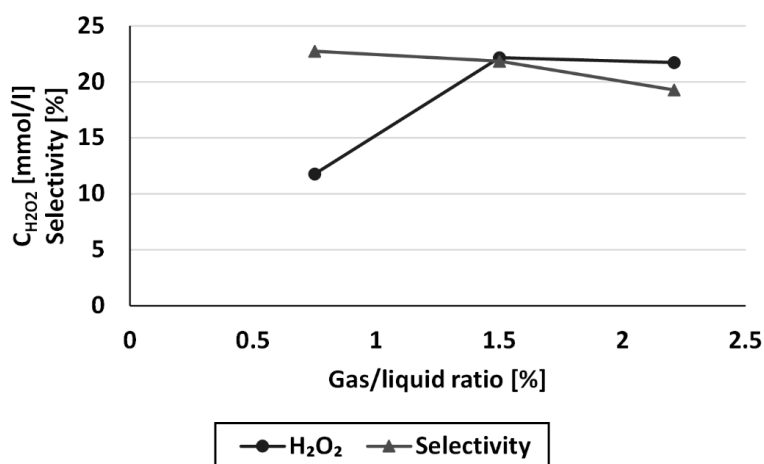
In Fig. 10, three different experiments are shown where gas flow rate was changing from 51 ml/min to 150 ml/min. The liquid flow rate was constant (68 ml/min). Therefore, gas/liquid feed ratio had values of 0.75, 1.00 and 2.21. The catalyst loading was 0.21 g of 3 wt.% Pd. The experimental conditions are shown in Table 3.

**Table 3**

Experimental conditions for studies of gas/liquid feed ratio.

No.	Liquid feed [ml/min]	Gas feed [ml/min]	Gas/liquid feed ratio [-]
1	68	51	0.75
2	68	102	1.00
3	68	150	2.21

The results of the experiments are shown in Fig. 10. The increase of H<sub>2</sub>O<sub>2</sub> concentration with increasing hydrogen feed is understandable. The decrease of selectivity can be explained by enhanced decomposition of H<sub>2</sub>O<sub>2</sub> via hydrogenation (see Fig. 1).

**Fig. 10.** Effect of gas/liquid feed ratio.

#### 4.2.3 Pd loading

The catalysts were prepared with 1 wt.%, 3 wt.%, and 5 wt.% Pd loading. The other conditions are shown in Table 4

**Table 4**

Experimental conditions for studies of Pd loading.

No.	Liquid feed [ml/min]	Gas feed [ml/min]	Catalyst [wt.% Pd]	Amount of catalyst [g]
1	68	102	1	0.21
2	68	102	3	0.21
3	68	102	5	0.21

The results are shown in Fig. 11. In the case of 1 wt.% Pd catalyst, almost all Pd particles were located inside micropores which are more difficult to access by the reactants. After increasing the amount of Pd to 3 wt.%, particles started to develop on the outer surface of carbon fibers which are easily accessible for the reactants. Further increase of Pd loading to 5 wt.% did not increase the number of active sites. It just led to bigger particles on the outer

surface of carbon fibers. Therefore, after 3 wt.% loading of Pd, the concentration of hydrogen peroxide did not increase anymore [9].

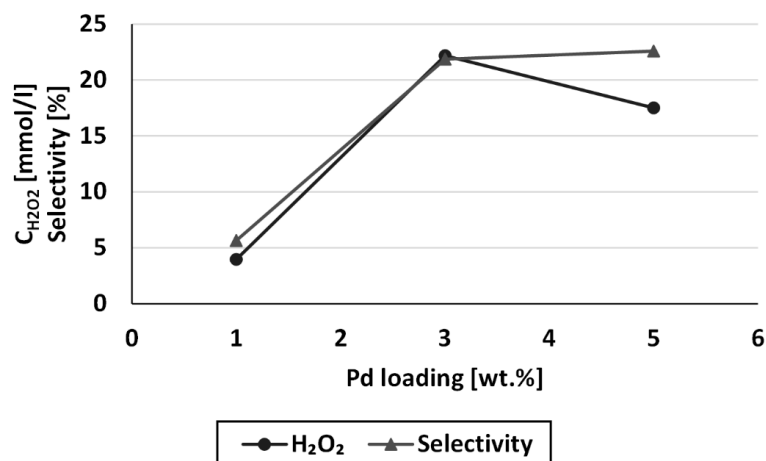


**Fig. 11.** Effect of Pd loading.

#### 4.2.4 Amount of catalyst

Experiments were done with two catalyst amounts, 0.21 and 0.42 g. The results are shown in Table 5.

The reason for the decreased selectivity might be the extra catalyst which caused the produced hydrogen peroxide to be hydrogenated or decomposed to water. This conclusion is supported by the observed decrease in the concentration of hydrogen peroxide.

**Table 5**

Effect of the amount of catalyst.

Amount of catalyst [g]	H <sub>2</sub> O <sub>2</sub> Concentration [mmol/l]	Selectivity [%]
0,21	22.16	21.85
0,42	14.18	16.00

Reaction conditions: Liquid feed rate = 68 ml/min, Gas feed rate = 102 ml/min, 3 wt.% Pd catalyst

## 5. Conclusions

A novel microreactor for direct synthesis of hydrogen peroxide was tested. The construction of the reactor, based on microstructured plates, offer certain advantages over conventional microreactors consisting of parallel channels with small diameter. Pd catalyst supported on carbon cloth was utilized.

The operation of the reactor was tested in a bench-scale process designed for experimental purposes. Effect of several process conditions on productivity and selectivity was studied and promising results achieved.

The microreactor and test process were designed to produce information for R&D purposes. The final goal is a full scale unit which have different design criteria and also partly different operation conditions.

The best strategy for scale-up is to install several parallel microreactor plates to enable sufficient throughput. Longer reactor plates with alternating mixing and catalytic sections would increase the yield. In this kind of reactor configuration several gas feeds through the cover plate, at different height levels, would be needed.

The arrangement of gas feed was designed for the test unit only. Hydrogen and oxygen gases, diluted with carbon dioxide, would be fed directly into the reactor in a production unit. The flow rates and compositions have to be optimized taking into account selectivity, yield and safety. Microreactor technology might offer possibilities to operate safely in the conditions which might be too dangerous with current technology but enhance the yield substantially. This has to be confirmed in a reliable way.

Separation of hydrogen peroxide and water from the circulating methanol stream is an essential part of a full scale process. This can be done with distillation. More promising, but also more challenging would be a membrane-based separation unit.

The research group will continue the development of the process concept according to these guidelines.

## References

- [1] B. Elvers, S. Hawkins, M. Ravenscroft, G. Schulz (Eds.), *Ulmann's Encyclopedia of Industrial Chemistry*, Vol. A13: Hydrogen peroxide, VCH, Weinheim, 1989.
- [2] Centi, G., Perathoner, S., Abate, S., Mizuno, N. (Eds.), *Modern Heterogeneous Oxidation Catalysis: Design, Reactions and Characterization*, Ch. 8: Direct synthesis of hydrogen peroxide: Recent advances, Wiley-VCH, Weinheim, 2009.
- [3] C. Samanta, Direct synthesis of hydrogen peroxide from hydrogen and oxygen: An overview of recent developments in the process, *Appl. Catal., A*, 350 (2008) 133-149.
- [4] C. E. Baukal Jr., *Oxygen-enhanced combustion*, CRC, New York, 1998.
- [5] Y. Voloshin, R. Halder, A. Lawal, Kinetics of hydrogen peroxide synthesis by direct combination of H<sub>2</sub> and O<sub>2</sub> in a microreactor, *Catal. Today*, 125 (2007) 40-47.
- [6] X. Wang, Y. Nie, J. L. Lee and S. Jaenicke, Evaluation of multiphase microreactors for the direct formation of hydrogen peroxide, *Appl. Catal., A*, 317 (2007) 258-265.
- [7] T. Inoue, Y. Kikutani, S. Hamakawa, K. Mawatari, F. Mizukami, T. Kitamori, Reactor design optimization for synthesis of hydrogen peroxide, *Chem. Eng. J.*, 160 (2010) 909-914.
- [8] T. Inoue, K. Ohtaki, S. Murakami, S. Matsumoto, Direct synthesis of hydrogen peroxide based on microreactor technology, *Fuel Process. Technol.*, 108 (2013) 8-11.
- [9] D. Gudarzi, W. Ratchanansorn, and I. Turunen, T. Salmi, M. Heinonen, Preparation and study of Pd catalysts supported on activated carbon cloth (ACC) for direct synthesis of H<sub>2</sub>O<sub>2</sub> from H<sub>2</sub> and O<sub>2</sub>, *Top. Catal.*, 56 (2013) 527-539.
- [10] J. K. Edwards, B. E. Solsona, P. Landon, A. F. Carley, A. Herzing, C. J. Kiely and G. J. Hutchings, Direct synthesis of hydrogen peroxide from H<sub>2</sub> and O<sub>2</sub> using TiO<sub>2</sub>-supported Au-Pd catalysts, *J. Cat.*, vol. 236 (2005) 69-79.
- [11] S. J. Freakley, M. Piccinini, J. K. Edwards, E. N. Ntainjua, J. A. Moulijn, G. J. Hutchings, Effect of reaction conditions on the direct synthesis of hydrogen peroxide with a AuPd/TiO<sub>2</sub> catalyst in a flow reactor, *ACS Catal.*, 3 (2013) 487-501.

- [12] P. Biasi, F. Menegazzo, F. Pinna, K. Eränen, T. O. Salmi, Continuous H<sub>2</sub>O<sub>2</sub> direct synthesis over PdAu catalysts, *Chem. Eng. J.*, 176-177 (2011) 172-177.
- [13] P. Biasi, N. Gemo, J. R. H. Carucci, K. Eränen and P. Canu, Kinetics and mechanism of H<sub>2</sub>O<sub>2</sub> direct synthesis over Pd/C catalyst in a batch reactor, *Ind. Eng. Chem. Res.*, 51 (2012) 8903-8912.
- [14] N. Gemo, P. Biasi, P. Canu and T. O. Salmi, Mass transfer and kinetics of H<sub>2</sub>O<sub>2</sub> direct synthesis in a batch slurry reactor, *Chem. Eng. J.*, 207-208, (2012) 539-551.
- [15] T. Moreno, J. García-Serna and M. J. Cocero, Direct synthesis of hydrogen peroxide in methanol and water using scCO<sub>2</sub> and N<sub>2</sub> as diluents, *Green Chem.*, 12 (2010) 282-289.
- [16] R. Burch, P. R. Ellis, An investigation of alternative catalytic approaches for the direct synthesis of hydrogen peroxide from hydrogen and oxygen, *Appl. Catal., B*, 42 (2003) 203-211.
- [17] D. Gudarzi, O. A. Simokova, J. R. H. Carucci, P. Biasi, K. Eränen, E. Kolehmainen, I. Turunen, D. Y. Murzin, T. Salmi, Direct synthesis of H<sub>2</sub>O<sub>2</sub> from H<sub>2</sub> and O<sub>2</sub> over carbon supported Au, Pd and Au-Pd/C bimetallic catalysts, *Chem. Eng. Trans.*, 21 (2010) 925-930.
- [18] P. Biasi, F. Menegazzo, F. Pinna, K. Eränen, P. Canu and T. O. Salmi, Hydrogen peroxide direct synthesis: selectivity enhancement in a trickle bed reactor, *Ind. Eng. Chem. Res.*, 49 (2010) 10627-10632.
- [19] P. Biasi, P. Canu, F. Menegazzo, F. Pinna and T. O. Salmi, Direct synthesis of hydrogen peroxide in a trickle bed reactor: comparison of Pd-based catalysts, *Ind. Eng. Chem. Res.*, 51 (2012) 8883-8890.
- [20] J. F. Ng, Y. Nie, G. K. Chuah, S. Jaenicke, A wall-coated catalytic capillary microreactor for the direct formation of hydrogen peroxide, *J. Catal.*, 268 (2010) 302-308.
- [21] S. Maehara, M. Taneda, K. Kusakabe, Catalytic synthesis of hydrogen peroxide in microreactors, *Chem. Eng. Res. Des.*, 86 (2008) 410-415.
- [22] W. Ratchanusorn, D. Semyonov, D. Gudarzi, E. Kolehmainen, I. Turunen, Hydrodynamics and mass transfer studies on a plate microreactor, *Chem. Eng. Process. Process Intensif.*, 50 (2011) 1186-1192.
- [23] D. Semyonov, W. Ratchanusorn, Ilkka Turunen, Hydrodynamic model of a microstructured plate reactor. *Comput. Chem. Eng.*, 52 (2013) 145-154.
- [24] R. Pohorecki, Effectiveness of interfacial area for mass transfer in two-phase flow in microreactors, *Chem. Eng. Sci.* 62 (2007) 66495-6498
- [25] R. T. Yang, *Adsorbents: Fundamentals and Applications*, JOHN WILEY & SONS, INC., New Jersey, 2003.
- [26] N. Gemo, P. Biasi, T. O. Salmi, P. Canu, H<sub>2</sub> solubility in methanol in the presence of CO<sub>2</sub> and O<sub>2</sub>, *J. Chem. Thermodyn.*, 54 (2012) 1-9.
- [27] J. K. Edwards, G. J. Hutchings, Palladium and Gold-Palladium Catalysts for the Direct Synthesis of Hydrogen Peroxide, *Angew. Chem. Int. Ed.*, 47 (2008) 9192-9198.

## ACTA UNIVERSITATIS LAPPEENRANTAENSIS

500. WANG, YONGBO. Novel methods for error modeling and parameter identification of redundant hybrid serial-parallel robot. 2012. Diss.
501. MAXIMOV, ALEXANDER. Theoretical analysis and numerical simulation of spectral radiative properties of combustion gases in oxy/air-fired combustion systems. 2012. Diss.
502. KUTVONEN, ANTERO. Strategic external deployment of intellectual assets. 2012. Diss.
503. VÄISÄNEN, VESA. Performance and scalability of isolated DC-DC converter topologies in low voltage, high current applications. 2012. Diss.
504. IKONEN, MIKA. Power cycling lifetime estimation of IGBT power modules based on chip temperature modeling. 2012. Diss.
505. LEIVO, TIMO. Pricing anomalies in the Finnish stock market. 2012. Diss.
506. NISKANEN, ANTTI. Landfill gas management as engineered landfills – Estimation and mitigation of environmental aspects. 2012. Diss.
507. QIU, FENG. Surface transformation hardening of carbon steel with high power fiber laser. 2012. Diss.
508. SMIRNOV, ALEXANDER. AMB system for high-speed motors using automatic commissioning. 2012. Diss.
509. ESKELINEN, HARRI, ed. Advanced approaches to analytical and systematic DFMA analysis. 2013.
510. RYYNÄNEN, HARRI. From network pictures to network insight in solution business – the role of internal communication. 2013. Diss.
511. JÄRVI, KATI. Ecosystem architecture design: endogenous and exogenous structural properties. 2013. Diss.
512. PIILI, HEIDI. Characterisation of laser beam and paper material interaction. 2013. Diss.
513. MONTO, SARI. Towards inter-organizational working capital management. 2013. Diss.
514. PIRINEN, MARKKU. The effects of welding heat input usability of high strength steels in welded structures. 2013. Diss.
515. SARKKINEN, MINNA. Strategic innovation management based on three dimensions diagnosing innovation development needs in a peripheral region. 2013. Diss.
516. MAGLYAS, ANDREY. Overcoming the complexity of software product management. 2013. Diss.
517. MOISIO, SAMI. A soft contact collision method for real-time simulation of triangularized geometries in multibody dynamics. 2013. Diss.
518. IMMONEN, PAULA. Energy efficiency of a diesel-electric mobile working machine. 2013. Diss.
519. ELORANTA, LEENA. Innovation in a non-formal adult education organisation – multi-case study in four education centres. 2013. Diss.
520. ZAKHARCHUK, IVAN. Manifestation of the pairing symmetry in the vortex core structure in iron-based superconductors. 2013. Diss.

521. KÄÄRIÄINEN, MARJA-LEENA. Atomic layer deposited titanium and zinc oxides; structure and doping effects on their photoactivity, photocatalytic activity and bioactivity. 2013. Diss.
522. KURONEN, JUHANI. Jatkuvan äänitehojakautuman algoritmi pitkien käytävien äänikenttien mallintamiseen. 2013. Diss.
523. HÄMÄLÄINEN, HENRY. Identification of some additional loss components in high-power low-voltage permanent magnet generators. 2013. Diss.
524. SÄRKKÄ, HEIKKI. Electro-oxidation treatment of pulp and paper mill circulating waters and wastewaters. 2013. Diss.
525. HEIKKINEN, JANI. Virtual technology and haptic interface solutions for design and control of mobile working machines. 2013. Diss.
526. SOININEN, JUHA. Entrepreneurial orientation in small and medium-sized enterprises during economic crisis. 2013. Diss.
527. JÄPPINEN, EERO. The effects of location, feedstock availability, and supply-chain logistics on the greenhouse gas emissions of forest-biomass energy utilization in Finland. 2013. Diss.
528. SÖDERHOLM, KRISTIINA. Licensing model development for small modular reactors (SMRs) – focusing on the Finnish regulatory framework. 2013. Diss.
529. LAISI, MILLA. Deregulation's impact on the railway freight transport sector's future in the Baltic Sea region. 2013. Diss.
530. VORONIN, SERGEY. Price spike forecasting in a competitive day-ahead energy market. 2013. Diss.
531. PONOMAREV, PAVEL. Tooth-coil permanent magnet synchronous machine design for special applications. 2013. Diss.
532. HIETANEN, TOMI. Magnesium hydroxide-based peroxide bleaching of high-brightness mechanical pulps. 2013. Diss.
533. TYKKÄLÄ, TOMMI M. Real-time image-based RGB-D camera motion tracking and environment mapping. 2013. Diss.
534. PEKKOLA, SANNA. Performance measurement and management in a collaborative network. 2013. Diss.
535. PANOREL, IRIS CHERRY. Pulsed corona discharge as an advanced oxidation process for the degradation of organic compounds in water. 2013. Diss.
536. TORKKELI, LASSE. The influence of network competence of internationalization of SMEs. 2013. Diss.
537. MOLANDER, SOLE. Productivity and services – safety telephone services for the elderly. 2013. Diss.
538. SITARZ, ROBERT. Identification of research trends in the field of separation processes. Application of epidemiological model, citation analysis, text mining, and technical analysis of the financial markets. 2013. Diss.
539. KATTEDEN, KAMIEV. Design and testing of an armature-reaction-compensated permanent magnet synchronous generator for island operation. 2013. Diss.
540. HÄMÄLÄINEN, HARRI. Integration of learning supportive applications to development of e-portfolio construction process. 2013. Diss.



